Universitat Autònoma de Barcelona

Contact resistance and electrostatics of 2DFETs

Ferran JOVELL MEGIAS

ADVERTIMENT. L'accés als continguts d'aquesta tesi doctoral i la seva utilització ha de respectar els drets de la persona autora. Pot ser utilitzada per a consulta o estudi personal, així com en activitats o materials d'investigació i docència en els termes establerts a l'art. 32 del Text Refós de la Llei de Propietat Intel·lectual (RDL 1/1996). Per altres utilitzacions es requereix l'autorització prèvia i expressa de la persona autora. En qualsevol cas, en la utilització dels seus continguts caldrà indicar de forma clara el nom i cognoms de la persona autora i el títol de la tesi doctoral. No s'autoritza la seva reproducció o altres formes d'explotació efectuades amb finalitats de lucre ni la seva comunicació pública des d'un lloc aliè al servei TDX. Tampoc s'autoritza la presentació del seu contingut en una finestra o marc alliè a TDX (framing). Aquesta reserva de drets afecta tant als continguts de la tesi com als seus resums i índexs.

ADVERTENCIA. El acceso a los contenidos de esta tesis doctoral y su utilización debe respetar los derechos de la persona autora. Puede ser utilizada para consulta o estudio personal, así como en actividades o materiales de investigación y docencia en los términos establecidos en el art. 32 del Texto Refundido de la Ley de Propiedad Intelectual (RDL 1/1996). Para otros usos se requiere la autorización previa y expresa de la persona autora. En cualquier caso, en la utilización de sus contenidos se deberá indicar de forma clara el nombre y apellidos de la persona autora y el título de la tesis doctoral. No se autoriza su reproducción u otras formas de explotación efectuadas con fines lucrativos ni su comunicación pública desde un sitio ajeno al servicio TDR. Tampoco se autoriza la presentación de su contenido en una ventana o marco ajeno a TDR (framing). Esta reserva de derechos afecta tanto al contenido de la tesis como a sus resúmenes e índices.

WARNING. The access to the contents of this doctoral thesis and its use must respect the rights of the author. It can be used for reference or private study, as well as research and learning activities or materials in the terms established by the 32nd article of the Spanish Consolidated Copyright Act (RDL 1/1996). Express and previous authorization of the author is required for any other uses. In any case, when using its content, full name of the author and title of the thesis must be clearly indicated. Reproduction or other forms of for profit use or public communication from outside TDX service is not allowed. Presentation of its content in a window or frame external to TDX (framing) is not authorized either. These rights affect both the content of the thesis and its abstracts and indexes.

UNIVERSITAT AUTÒNOMA DE BARCELONA

DOCTORAL THESIS

Contact resistance and electrostatics of 2DFETs

Author:
Ferran JOVELL MEGIAS

Supervisor:
Dr. Xavier CARTOIXÀ SOLER

A thesis submitted in fulfillment of the requirements
for the degree of
Ph.D. in Electrical and Telecommunication Engineering

in the

Research Group of Computational Nanoelectronics
Department d'Enginyeria Electrònica

July 2018

"Everything is made of atoms."

Richard P. Feynman

Abstract

Ferran JOVELL MEGIAS

Contact resistance and electrostatics
of 2DFETs

In the last decade, the rise of graphene and other 2-dimensional materials revolutionized materials science. The new physics brought by these new materials opened up the possibilities of new devices with outstanding characteristics. In the field of radiofrequency electronics, some of these devices are predicted to bridge the terahertz gap in the frequency spectrum. In this thesis, several simulation techniques have been employed to study different devices with this long term goal in mind.

In first place, a single-layer molybdenum disulfide (MoS_2) field effect transistor (FET) has been studied using the drift-diffusion model. To delve deeper into this, a MoS_2 $p-n$ junction has also been studied in this framework. Even though the drift-diffusion model is suited for bulk materials, a set of effective parameters was found. With it, it has been possible to reproduce the on-current of experimental data of the single-layer MoS_2 FET, but not the subthreshold swing. On the other hand, the MoS_2 $p-n$ junction yielded valuable results for the study of the depletion region.

One of the hurdles that must be overcome in order to harness the possibilities of graphene and other 2D materials so that the performance of high frequency devices is not compromised is to achieve a low enough contact resistance (R_c) between the metal contact and the channel. In this thesis, an intermediate graphite layer between the metal contact and the graphene layer is proposed in order to achieve the $100\ \Omega \cdot \mu$m mark that is often quoted to be the upper limit for R_c not to be the limiting factor. A graphite-graphene top contact structure is proposed and studied under ballistic transport by density functional theory (DFT) and Non-Equilibrium Green's Function Theory (NEGF) to calculate the contact resistance. In particular, several overlap amounts between graphene over the graphite bulk were studied. The results obtained are very promising for doped samples of graphene. To assess these results, a current path analysis was conducted using the eigenchannel formalism. This analysis showed that the transfer of electrons was done through the area of contact instead of an

edge. It was concluded that graphite was a suitable buffer to reduce R_c for metal-graphene contacts.

Finally, in order to understand better some of the experimental results in the contact resistance of metal-graphene contacts, the objective was to generate realistic atomic configurations using Molecular Dynamics. For that, a first step is to parametrize the metal-carbon interactions. The bond order potential (BOP) force field was chosen for this as it is a force field that can accurately describe the metal-carbon covalent bond. The metal-metal bond is described using the embeded atom potential (EAM) and the carbon-carbon interaction, by the Tersoff force field. The BOP force field has a ten parameter set that describe the characteristics of the bond: equilibirum distance, bond energy, etc. Using Parallel Tempering Monte Carlo (PTMC) optimisation algorithm trained from first principles calculations of small metal particles on top of a graphene sheet, a set of parameters for the BOP force field was obtained for the Pd-C and Ni-C pairs.

Resum

Ferran JOVELL MEGIAS

Contact resistance and electrostatics
of 2DFETs

Durant la darrera dècada, la popularització del grafè i altres materials de dues dimensions (2D) ha revolucionat la ciència de materials. Els nous fenòmens físics que esdevenen en aquests nous materials obren les possibilitats per a nous dispositius amb característiques extraordinàries. En el camp de l'electrònica d'alta freqüència, per alguns d'aquests dispositius s'ha predit que poden obrir el forat que hi ha actualment en el rang del terahertz. En aquesta tesis s'han fet servir diferents tècniques de simulació per estudiar diferents dispositius en l'entorn d'alta freqüència en ment.

En primer lloc, un transistor d'efecte de camp compost per una mono capa de disulfit de molibdè (MoS_2) ha estat estudiat fent servir el model de deriva difusió. Per aprofundir en això, s'ha estudiat també una unió $p-n$ amb aquest mateix material. Malgrat que el model de deriva difusió està pensat per materials convencionals, s'ha fet servir un conjunt de paràmetres efectius per tal de reproduir les dades experimentals. Amb aquest conjunt de paràmetres, ha estat possible reproduir el corrent de sortida d'aquest transistor tot i que no el període de transició. D'altra banda, els resultats de la unió $p-n$ han estat molt valuosos per a l'estudi de la zona de depleció.

Un dels obstacles a superar per poder poder utilitzar grafè i altres materials 2D en aplicacions d'alta freqüència, per tal de no comprometre el rendiment d'aquests dispositius, és el d'obtenir una resistència de contact (R_c) prou baixa. En aquesta tesi, s'ha proposat d'afegir una capa intermèdia de grafit entre el contacte metàl·lic i el canal de grafè per tal de reduir la resistència de contacte per sota dels 100 $\Omega \cdot \mu$m que sovint es cita com el límit del qual pot limitar el rendiment dels transistors d'efecte de camp. Un contacte de tipus "top" s'ha fet servir per a l'estructura de grafit-grafè que és molt convenient per simulacions de transport balístic mitjançant la teoria de la densitat del funcional juntament amb la teoria del no equilibri de green per a calcular aquesta resistència. En particular, s'han simulat diverses longituds de superposició del grafè sobre el contacte de grafit per tal d'estudiar-ne el seu efecte. S'ha observat que per a concentracions de portadors intrínseques, la resistència de contacte és molt alta, però per a làmines de grafè dopades, aquesta resistència decau per sota del límit citat. Per tal d'avaluar aquests resultats, s'ha estudiat el camí de corrent mitjançant el formalisme d'autocanals. Aquesta anàlisi demostra que la transferència d'electrons es duu a terme mitjançant l'àrea de solapament en comptes de la vora. El cas de vora també ha estat considerat com a referència per ser el cas límit. S'ha conclòs que una capa de grafit abans de la capa de grafè és viable per tal de reduir la resistència de contacte en els contactes metall-grafè.

Finalment, per tal d'entendre amb profunditat alguns dels resultats experimentals pel què fa a la resistència de contacte entre un metall i el grafè, l'objectiu és de generar estructures realistes mitjançant la dinànima molecular. Per a tal fi, el primer pas és el de parametritzar l'enllaç metall-carboni. El potencial d'odre d'enllaç fou escollit ja que és el potencial indicat per descriure aquesta mena d'enllaços covalents. Les interaccions metall-metall foren descrites pel potencial d'àtom incrustat, i la l'enllaç carboni-carboni pel potencial de Tersoff. El potencial de l'ordre d'enllaç està caracteritzat per un conjunt de deu paràmetres que descriuen les característiques de l'enllaç com són la distància d'equilibri o l'energia d'enllaç, entre altres. Mitjançant l'algorisme de Monte Carlo temperat paral·lel, s'ha pogut obtenir un conjunt de paràmetres per a la interacció Pd-C i Ni-C.

Acknowledgements

Tal i com diu un probervi Africà, "Si vols caminar ràpid, ves sol. Si vols caminar lluny, ves acompanyat". I certament he arribat lluny, però no sense l'ajuda indispensable de molta gent qui, al llarg d'aquest temps, ha caminat amb mi.

Primer a en Xavier Cartoixà per la seva dedicació a la recerca amb qui hem passat incontables hores tancats al despatx intentant entendre com funcionen les coses. A en David Jiménez per la seva incansable motivació per a l'excel·lència i per donar-me la oportunintat de participar en el projecte del Graphene Flagship. Després al Departament d'Enginyeria Electrònica per acollir-me durant aquests anys. També vull agraïr l'ajut de companyes i companys del department, Enrique, Laura i Martí i l'Anna, entre d'altres, per converses, ajudes i riures durant aquest temps. This project has received funding from the EU Horizon2020 research and innovation program under grant No. 696656, Graphene Flagship. I also want to acknowledge financial support by the Spanish MINECO under Project No. TEC2015-67462-C2-1-R (MINECO/FEDER).

To Professor Laurent J. Lewis for supervising my work during my stay at Université de Montréal and teach me another way to look at research and giving insight and advising on how to think from a perspective I have never would have been possible to otherwise. And to Daniel Fröster for his collaboration in the making of Chapter 4. His knowledge and research helped me understand and carry out this part of the project otherwise not possible.

Als meus amics qui han estat durant tot aquest temps al meu costat i amb qui he pogut gaudir de converses, estones, àpats i més durant els moments més durs i més bons. La vostra companyia és i serà absolutament necessària, ara i sempre.

A en Poire Vallvé i als cantaires del cor de la UAB que tants assaigs i cants han passat durant la durada de la meva tesi que han ajudat a espantar molts mals i a inspirar la creació i desig de fer del món el millor possible.

Finalment, a la meva estimada família qui, durant aquesta època, m'han donat suport i ajuda que sens cap dubte han estat imprescindibles. Em sento molt afortunat de tenir una família que m'estimi tant i sempre hi sigui per donar suport, i per sempre creure amb mi i donar-me ales per poder volar fins l'horitzó i més enllà.

A tots, moltes gràcies.

Ferran Jovell a Bellaterra a juny de 2018.

Contents

List of Figures

List of Tables

List of Abbreviations

DFT	**D**ensity **F**unctional **T**heory
NEGF	**N**on-**E**quilibrium **G**reen **F**unction **T**heory
CNT	**C**arbon **N**ano **T**ube
2DEG	**2** **D**imensional **E**lectron **G**as
MD	**M**olecular **D**ynamics
FEM	**F**inite **E**lement **M**ethod
BOP	**B**ond **O**rder **P**otential
EAM	**E**mbeded **A**tom **M**ethod
PTMC	**P**arallel **T**empering **M**onte **C**arlo
FET	**F**ield **E**ffect **T**ransistor
GFET	**G**raphene **F**ield **E**ffect **T**ransistor
MOSFET	**M**etal **O**xide **S**emiconductor **F**ield **E**ffect **T**ransistor

Physical Constants

Speed of Light	$c = 2.997\,924\,58 \times 10^{8}\,\mathrm{m\,s^{-1}}$ (exact)
Planck Constant	$h = 6.626\,069\,934(89) \times 10^{-34}\,\mathrm{J\,s}$
Reduced Planck Constant	$\hbar = 1.054\,571\,800(13) \times 10^{-34}\,\mathrm{J\,s}$
Elemental Charge	$e = 1.602\,176\,6(57) \times 10^{-19}\,\mathrm{C}$
Electron Mass	$m_e = 9.109\,382\,2(91) \times 10^{-31}\,\mathrm{kg}$
Boltzmann Constant	$k_B = 8.617\,332(4) \times 10^{-5}\,\mathrm{eV\,K\,s^{-1}}$
Vacuum Permittivity	$\varepsilon_0 = 8.854\,187\,8 \times 10^{-12}\,\mathrm{F\,m^{-1}}$
Vacuum Permeability	$\mu_0 = 4\pi \times 10^{-7}\,\mathrm{H\,m^{-1}}$ (exact)
Bohr Radii	$r_0 = 5.291\,772\,11 \times 10^{-11}\,\mathrm{m}$

Dedicada als meus estimats pares que
m'han donat sempre tot l'amor i el
suport que qualsevol fill pogués desitjar.

Foreword

This document is a doctoral thesis. This is the culmination of the work I have been doing during this past four years. Right here, the end of an era, of a period in which I dedicated my full body and mind into this research. Achieving this point has not been easy, and never was in the first place. However, this thesis will summarize all underlying theory that supports all these graphs, data points and numbers into some meaning applied to the real world, or at least an interpretation of it. Over the chapters of this thessis many subjects will be investigated and looked into. To the untrained eye, it might sound all like gibberish, but for those of you who understand all of these equations, it will make some sense. I want this document to be a reflection of all the knowledge I have accquired, studied, discussed with collegues and professors, around the world in conventions, study sessions, seminars and meetings into a standalone document that you can read and is coherent and understandable even if you are not capable of making sense of all the equations. On top of all this, my contributions to the world of electronic engineering in the radiofrequency applications will be added. Finishing my doctoral thesis does not mean I will stop asking questions, investigating or creating knowledge, hopefully. I look into the future with great aspirations and I am eager to jump into the next chapter of my life.

Chapter 1

Introduction

1.1 A look back

Before jumping into density functional theory or the wonders of molecular dynamics, some context has to be given. Human knowledge is very vast and it is necessary, if not mandatory, to put all things in its place otherwise it does not make sense. One could say that the study of electronics and semiconductors exploded when J. Bardeem, W. H. Brattain and W. Schockley invented the transistor back in 1947. Soon after, the first integrated circuit was built as well, and from there on the development of this new branch of knowledge, semiconductor physics, or semiconductor engineering really took off. In 1965, G. Moore published his paper [65] predicting the growth of the number of transistors in a chip would double every 18 months (See Fig. 1.1). But, since recently this is no longer the case. After the transistor gate reached the mark of 14nm, Si Metal Oxide Semiconductor Field Effect Transistor (MOSFET) scaling is no longer possible at previous rates due to discreteness of the matter, short-channel effects or the deteriorating effects of parasitics. To palliate these effects researchers have dealt with this phenomenon with new MOSFET architectures and using other materials. Nevertheless this only delays the moment in which the MOSFET scaling becomes impractical. In radio-frequency, electrical engineers and researchers are looking for new materials with ultra-high mobilities. The objective is to develop transistors with mobilities operating in the terahertz gap (0.3-3 THz), which has not been used yet. Activities in 2D materials such as graphene or molybdenum disulfide (MoS_2) have grown in recent years to stay. This kind of materials allows new architectures, features and properties in MOSFETs with respect to bulk traditional mateirials. The high mobility of a 2 Dimensional Electron Gas (2DEG) is yet to be exploited thanks to this confinement and will be an outbreak for the following years.

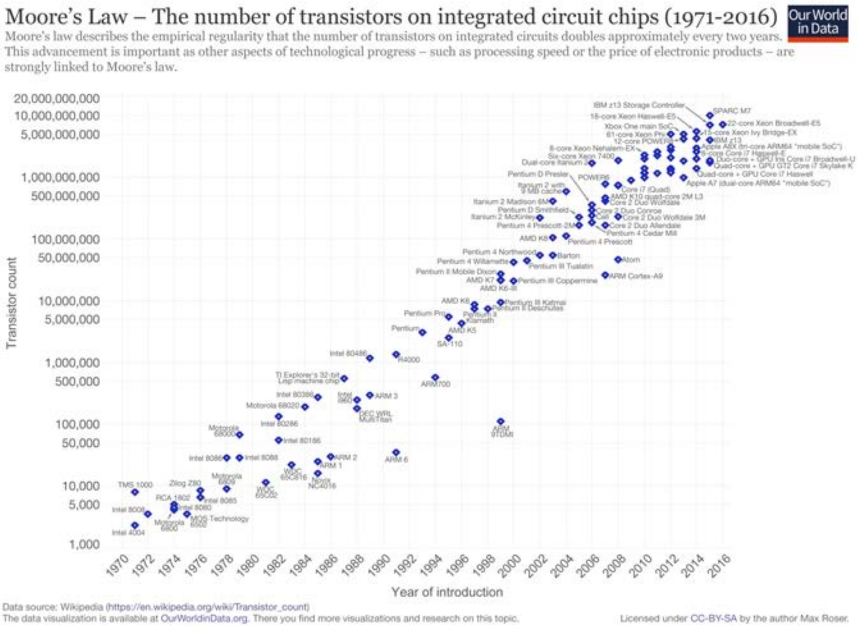

FIGURE 1.1: Moore's Law diagram. Every 18 months the number of transistors on a chip doubles [83].

1.2 Materials Science

The study of materials science has advanced to the point where it is possible to design a new material atom by atom or layer by layer. So, it is essential to have a systematic way of classifying materials and ordering in such a way that the systematic study of them is possible. Crystallography is the study of said materials and the classification of materials and crystals with respect to the atom's arrangement. In this next section, a brief introduction about the crystalline structure of materials is going to be set out, along with the energy bands interpretation, which is going to be useful later on. Further reading in Ref. [89].

1.2.1 Crystal Structure

All the properties of any material are closely related to the crystalline structure present at the atomic level. For a crystalline solid, there exist three primitive vectors such that the crystal structure remains invariant under a translation through any vector. This is called the Bravais or direct lattice,

$$\mathbf{R} = n_1\mathbf{a}_1 + n_2\mathbf{a}_2 + n_3\mathbf{a}_3, \tag{1.1}$$

where n_i are the primitive vectors of the lattice, with $i = 1, 2, 3$ are integer numbers. The lattice is now described by these characteristic vectors. The crystal is defined by adding a set of atoms at each point of the lattice (basis). Ideally, these crystals would span to infinity so

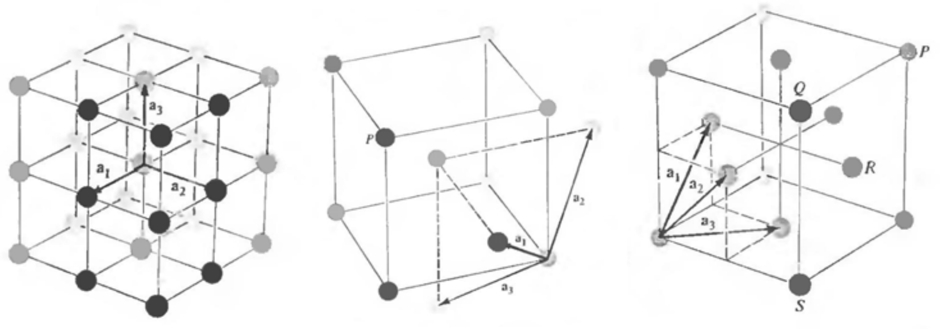

FIGURE 1.2: Three basic bravais lattices from left to right: Simple cubic, Body Centered Cubic (BCC) and Face Centered Cubic (FCC). Figure adapted from Ref. [3].

there is not surface or edge problems. For now, let's consider there is an infinite crystal. Since it is infinite, there is a region in this crystal that can be defined in a way that atoms inside this region can be used as building blocks, called a primitive cell. One kind of primitive cell of any given lattice is the Wigner-Seitz cell. This Wigner-Seitz cell can be constructed by drawing perpendicular bisector planes in the lattice from the chosen point to the nearest equivalent lattice sites. In Fig. 1.2 the three different basic cubic structures can be found: simple cubic, face centered cubic and body centered cubic. It is very convenient, in the solid state theory, to define the reciprocal of any given lattice.

The reciprocal lattice can be defined, for a given set of vectors in 1.1 as

$$\mathbf{b}_1 = 2\pi\frac{\mathbf{a}_2 \times \mathbf{a}_3}{\mathbf{a}_1 \cdot \mathbf{a}_2 \times \mathbf{a}_3},\ \mathbf{b}_2 = 2\pi\frac{\mathbf{a}_3 \times \mathbf{a}_1}{\mathbf{a}_1 \cdot \mathbf{a}_2 \times \mathbf{a}_3},\ \mathbf{b}_3 = 2\pi\frac{\mathbf{a}_1 \times \mathbf{a}_2}{\mathbf{a}_1 \cdot \mathbf{a}_2 \times \mathbf{a}_3} \tag{1.2}$$

so that $\mathbf{a}_i \cdot \mathbf{b}_j = 2\pi\delta_{ij}$ with $i = 1, 2, 3$ and where δ_{ij} is the Korneker delta. The general reciprocal lattice can be written as

$$\mathbf{k} = k_1\mathbf{b}_1 + k_2\mathbf{b}_2 + k_3\mathbf{b}_3 \tag{1.3}$$

where k_i are the reciprocal lattice vectors, with $i = 1, 2, 3$ are integer numbers. Equivalently to the Wigner-Seitz cell, in the reciprocal space the first Brillouin zone can be defined. It is a Wigner-Seitz cell in this reciprocal space. In Fig. 1.3 the Brillouin zone for two of the most common crystal structures is shown for reference [1]. This, defines the basis for the crystallography, the classification of all crystals according to its symmetry group. The reciprocal lattice is used, among other things, to draw the energy bands with respect to the Brillouin points.

---

[1] The First Brillouin zone for the cubic lattice is another cubic lattice with lattice parameter π/a.

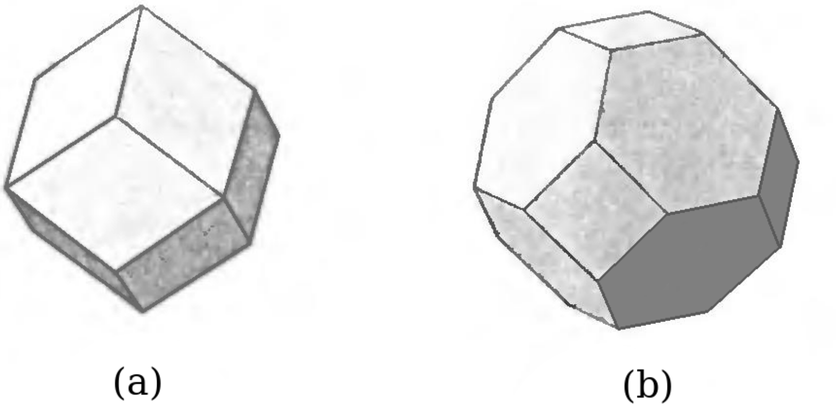

FIGURE 1.3: (a) First Brillouin zone for the body-centered lattice (b) First Brillouin zone for the face-centered lattice. Figure adapted from Ref. [3].

The energy band structure of a crystalline solid is the relation between the energy and the quasi momentum, **k** of the electrons within the solid. This energy dispersion is unique for every solid, so it can provide a lot of information about the material at hand. It is usually obtained from the solution to the Schrödinger equation:

$$\hat{\mathcal{H}}\ \psi_{\mathbf{k}}(\mathbf{r}) = E_{\mathbf{k}}\ \psi_{\mathbf{k}}(\mathbf{r}) \tag{1.4}$$

Where $\hat{\mathcal{H}}$ is the Hamiltonian of the crystal. In order to account for the periodicity on any given crystal, the Bloch theorem is used [5]. When the potential $V(\mathbf{r})$ in the Hamiltonian is periodic, the wave function is

$$\psi_{\mathbf{k}}(\mathbf{r}+\mathbf{R}) = e^{i\mathbf{k}\cdot\mathbf{R}}\psi_{k}(\mathbf{r}), \tag{1.5}$$

Bloch's theorem allows to find the total crystal wave function that accounts for that periodicity. Each state of the crystal can be labeled with **k**, which is a reciprocal vector that represents the phase shift from one site to another. So, it is possible to obtain the bands of a crystalline solid by solving the Schrödinger equation and finding the relation $E(\mathbf{k})$. In the case of semiconductors or insulators, Fig. 1.4 represents a generic band diagram which two bands are repsesented, the conduction band, E$_c$ and the valence band, E$_v$. In general, two regions can be distinguished. The Conduction band, upper band, labelled E_c. The Valence band, the lower band, labelled E_v. The energy bandgap is defined as

$$E_g = |\text{min}(E_c) - \text{max}(E_v)|. \tag{1.6}$$

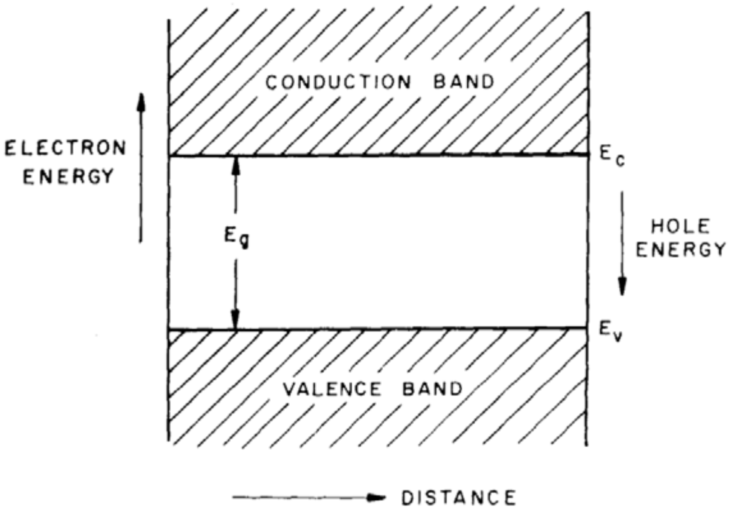

FIGURE 1.4: General form of Energy Bands for a semiconductor or an insulator. The upper band is the conduction band, E_c. The lower band, the valence band E_v. The distance between the two bands is the bandgap, E_g. Picture adapted from [89]

This value is one of the most important parameters in material physics because materials can be classified as insulators, semiconductors, semimetallic or metal depending on this value, E_g. Another relevant quantity in semiconductor physics is the Fermi level [2]. The Fermi level, E_f, is the energy level corresponding to the last occupied state in the band diagram at 0K. At a finite temperature, is the average change in energy when a particle is added to the system. In a semiconductor material it is possible to find two types of charge carriers electrons and holes. The position of the Fermi level determines the majority carriers in a semicondcutor. If the majority carriers are electrons, the semiconductor is often called a n-type semiconductor. If the majority carriers are holes, it is otherwise called a p-type semiconductor.

1.2.2 2D Materials

In this thesis a focus has been put in 2-Dimensional (2D) materials. This kind of materials is characterized by the fact that they are atomically narrow in one direction while being of arbitrary size along the other two. This causes a quantization of the energy levels for the electrons creating the so called 2 dimensional electron gas (2DEG), which has very interesting properties from the physical point of view. One of the most interesting and relevant properties that are useful in electronics is the high mobility of the electrons when they are confined.

Carbon allotropes have been observed before in different forms and dimensionalities. From the C_{60} "bucky ball" [49] to the carbon nano tubes (CNT) [63] that correspond to quasi

---

[2] Strictly speaking, the chemical potential.

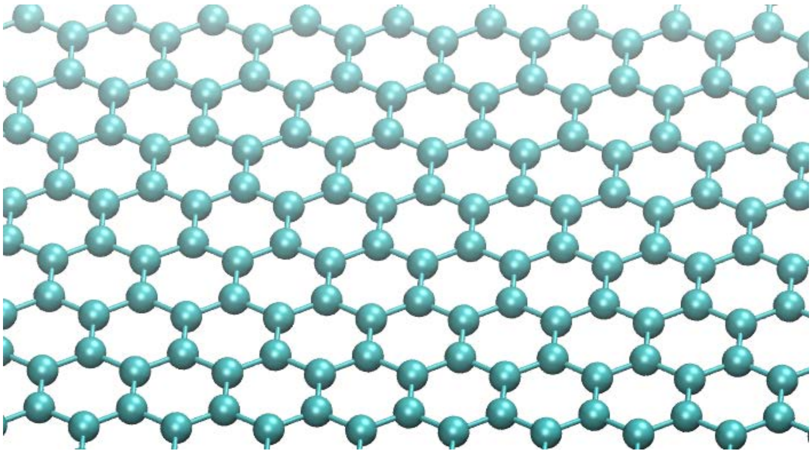

FIGURE 1.5: Graphene Honeycomb Lattice. Lattice parameter $a = 2.4829$ Å. Picture generated with VMD [41].

0D and quasi 1D systems. And being graphite the 3D counterpart, a free-standing allotrope for a 2D carbon had not been yet observed. It was not until Novoselov, Geim *et. al.* [69, 68, 70] reported the observation and measurements of graphene, a single-layer graphite. In a way, graphene is the unfolding of a CNT. This opened the door to the study of several other 2D materials using similar techniques [30]. With a collection of 2D van der Waals layered materials it is possible to create heterostructures with different functionalities such as LEDs [104], atomically thin $p-n$ junctions [51], photodetectors [48] and other devices [57].

Although graphene is not much of use for digital logic applications, due to the lack of a band gap, graphene field effect transistors (FETs) have been fabricated. It has been theorized that the ultra-high electron mobility in graphene can be used to bridge the terahertz gap in high frequency applications [67, 90]. The objective of the present thesis has been in the long range goal of High-Frequency electronics. Over the course of this work, 2D materials and low dimensionality structures have been used to this end and they have been studied with such applications in mind. These materials are described in the following sections: graphene, molybdenum disulfide, hafnium oxide and graphite, to name a few.

Graphene

Graphene is a 2-dimensional material formed by carbon atoms disposed in a honeycomb lattice. It is known for conducing both electricity and heat very efficiently and is structurally strong. From the state crystallographic point of view this material can be described as a hexagonal lattice structure with a basis of two atoms. The primitive vectors can be taken as

$$\mathbf{a}_1 = a\left(1, 0\right), \; \mathbf{a}_2 = a\left(\frac{1}{2}, \frac{\sqrt{3}}{2}\right)$$

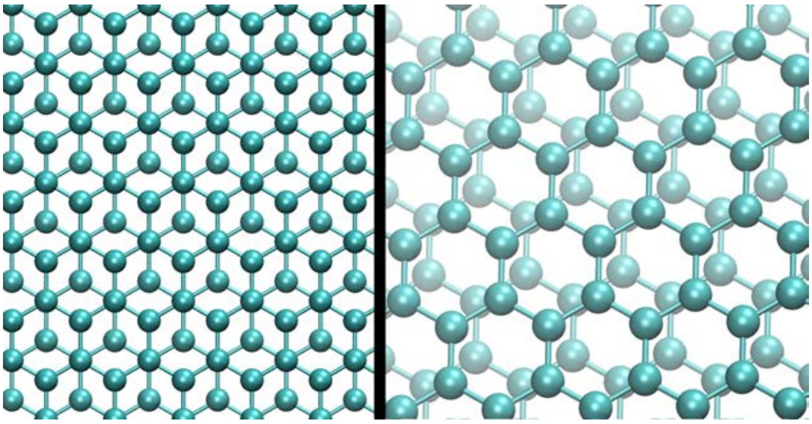

FIGURE 1.6: Graphite AB stacking. Each graphite layer is a graphene layer shifted with respect to the adjacent layers. Lattice parameters $a = 2.488\text{Å}$, $c = 6.54\text{Å}$. Top view (left), side view (right). Picture generated with VMD [41].

where a is the lattice constant. The atomic positions (in fractional coordinates of the primitive vectors) are given by

$$\mathbf{b'}_1 = \Big(-\frac{1}{6}, +\frac{1}{3}\Big),\ \mathbf{b'}_2 = \Big(+\frac{1}{6}, -\frac{1}{3}\Big).$$

Graphite

Graphite is a mineral composed solely by carbon. In particular, it can be thought of as "bulk" graphene. Its crystalline structure is graphene with an AB stacking, see Fig. 1.6. The different layers are bound by van der Waals forces. Its crystallographic characteristics are very similar to graphene, but with an extra layer.

$$\mathbf{a}_1 = a\Big(\frac{1}{2}, +\frac{\sqrt{3}}{2}, 0\Big),\ \mathbf{a}_2 = a\Big(\frac{1}{2}, -\frac{\sqrt{3}}{2}, 0\Big),\ \mathbf{a}_3 = c\Big(0, 0, 1\Big),$$

where a is the in-plane lattice constant and c the vertical lattice. The atomic positions with respect to the lattice vectors are

$$\mathbf{b'}_1 = \Big(0, 0, 0\Big),\ \mathbf{b'}_2 = \Big(-\frac{1}{3}, +\frac{1}{6}, 0\Big),\ \mathbf{b'}_1 = \Big(0, 0, \frac{1}{2}\Big),\ \mathbf{b'}_4 = \Big(+\frac{1}{3}, -\frac{1}{6}, \frac{1}{2}\Big).$$

Molybdenum disulfide (MoS_2)

Bulk Molybdenum disulfide (MoS_2) is a layered semiconductor with an indirect band gap [46]. In its monolayer form, the band structure changes to a direct gap semiconductor with a band gap of 1.8 eV [107]. The fact that this material is a semiconductor is useful in the sense that it is possible to investigate further in 2D materials with parabolic bands (see Sec. 1.2.4). The

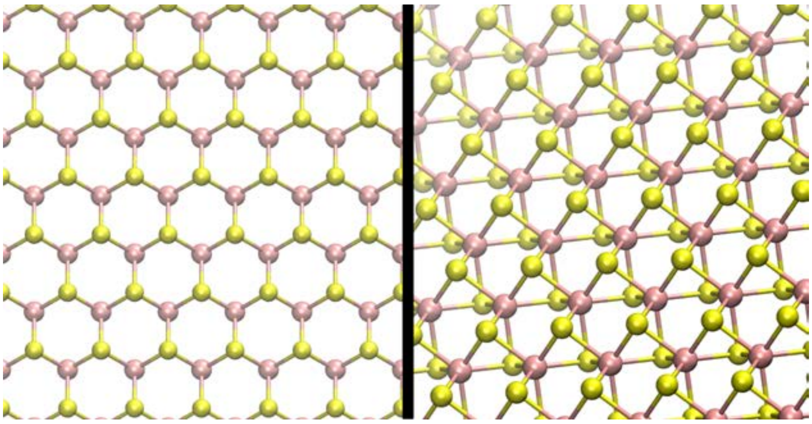

FIGURE 1.7: MoS_2 mono layer top view (left) and side view (right). Molybdenum atoms are represented by Pink balls and Sulfur atoms are represented by yellow balls. Image generated with VMD [41].

different layers are held by van der Waals forces, can, like graphene, be obtained via mechanical exfoliaton [54]. From a crystallographic point of view, a mono layer MoS_2 can be described as an hexagonal structure

$$\mathbf{a}_1 = a\left(\frac{1}{2}, +\frac{\sqrt{3}}{2}\right),\ \mathbf{a}_2 = a\left(\frac{1}{2}, -\frac{\sqrt{3}}{2}\right),$$

where a is the in-plane lattice constant. The atomic positions, in fractional coordinates with respect to the lattice vectors in the primitive cell, are given by

$$\mathbf{b'}_1 = \left(0, 0\right),\ \mathbf{b'}_2 = \left(\frac{2}{3}, \frac{1}{3}\right).$$

1.2.3 Other materials

Hafnium Oxide (HfO_2)

Hafnium Oxide is a high-κ insulator with a wide band gap of around $5.3 - 5.7$ eV [4]. Its dielectric constant is around $25\ \varepsilon_0$ [82], which makes it a very strong candidate for thin layer insulator in nanoelectronic devices. Its crystalline structure has different phases being the monoclinic and amorphous phases the most common. It is also used in resistive switching technologies due to its composition and crystalline structure [100].

1.2.4 Graphene vs. traditional semiconductors

Graphene is a very particular material for many reasons. First, it is a 2D material meaning that the dimensionality on one direction is very small. Second, is made entirely out of carbon, which is not an element usually found in the semiconductor industry, but as an impurity. Finally, the band diagram of graphene is very particular in the sense that it is neither a

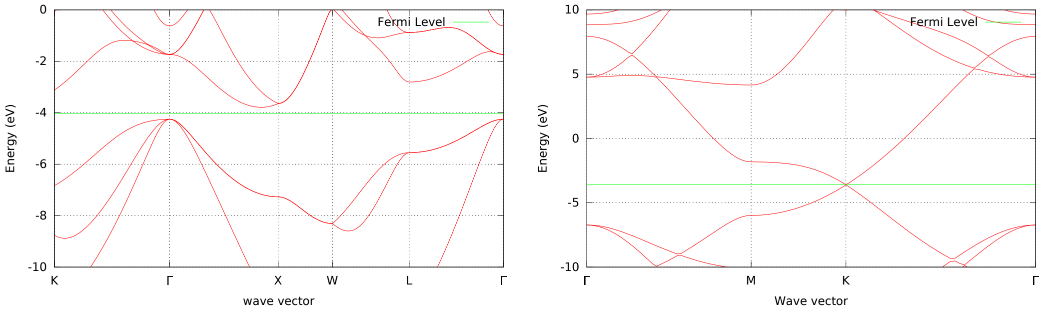

FIGURE 1.8: Energy bands for Silicon (left) and Graphene (right). The green line represents the Fermi level for intrinsic concentrations of carreirs.

semiconductor or an insulator, but a semimetal as the bands cross at the K point in the Brillouin zone. Near this point the bands of graphene can be approximated by Eq. 1.7.

$$E(k) = v_F \; \hbar \; |k| \tag{1.7}$$

where v_F is the Fermi velocity which takes values $\sim 10^6 \; m/s$. On the other hand, near the band edge the conduction band of traditional semiconductors can be approximated by Eq. 1.8, which is, instead, parabolic in k.

$$E(k) = \frac{h^2 k^2}{2m} \tag{1.8}$$

Figure 1.8 shows the band diagram for graphene and silicon is compared. As mentioned before, graphene bands cross at the K point of the Brillouin zone while Silicon bands do not cross and feature an experimental gap of 1.11 eV at 300K [45]. In digital electronics, the band gap is an essential magnitude to build, for example, a transistor. This allows the transistor to be switched on and off. However, graphene cannot be used for digital applications as per not having a band gap. Instead, it can be used for analog applications [73], its high mobility [6] or its high heat conductivity may be better suited for other uses.

1.3 Outline

This thesis is structured in the following way. In Chapter 1 a brief introduction to semiconductors and 2D materials with an emphasis on Graphene has been made. Following this, in Chapter 2 the theoretical background for the different approaches will be described as well as some details on the implementation uesd. Then, each of these techniques will be put to use and show some studies on different 2DM-based analog FETs and its results. In

Chapter 3 a 2D based FET is studied through the finite element method to obtain a macroscopic model with a set of parameters to model MoS_2 within this method. Afterwards, in Chapter 4 a parametrisation for carbon nickel and palladium in the BOP frame was found, discussed and tested for the simulation of metal deposition on a graphene substrate to study the contact resistence of a metal-graphene contact. In Chapter 5 the *ab initio* study of contact resistance between graphite and graphene and then using graphite as a buffer for the contact for the obtention of a contact structure that is suitable for high Rf transistors. The NEGF equations are used, along with DFT, to calculate ballistic transport through the studied geometry and finally compute the contact resistance from this system. Finally, in Chapter 6, a summary of the conclusions of this thesis.

Chapter 2

Methodologies

2.1 Computational Methods

The use of computer simulations to model and study different systems has been widely accepted for decades. The first time a simulation was carried out with a computer, in broad terms, was during the 1940s in the Manhattan project in Los Alamos [62]. Later, with the invention of the transistor and the firs CPU architectures, the use for computer simulations became inexpensive and its applications became more broadly used. This also led to the development of more efficient numerical techniques as well as many tools, programming languages and libraries for the efficient implementation of these techniques. Different techniques offer different properties which will be determined by the problem that wants to be solved. In a way, it is possible to order the different types of simulation techniques by this characteristic size and plot it against the characteristic simulation time. In Fig. 2.1 a picture of this sort is shown. In the horizontal axis, the characteristic size, in the vertical axis, the characteristic time. In the bottom left, where systems are smaller and computation times are larger, there are the Quantum Chemistry methods. These include methods such as Hartree-Fock which are used for chemists in small molecules, and chemical reactions. Next, there is the Density Functional Theory, in which this thesis has based parts of its work from. Then, the semi-empirical methods, such as tight-binding, that allow for larger systems but by approximating the total wave function using a localized basis. After this, the system size is large enough that quantum effects might be included in a broader picture. These are the classical methods that make use of the classical equations of motion, and a force field, in which all the interaction between the different particles, for calculating the forces and integrating said equations of motion. Finally, macroscopic methods, such as Finite Element methods, that leave the atomistic view of the system aside and, instead, approach it by defining regions that have a set of characteristics that represent a material. In this thesis, several simulation methods have been employed with different objectives for different experiments.

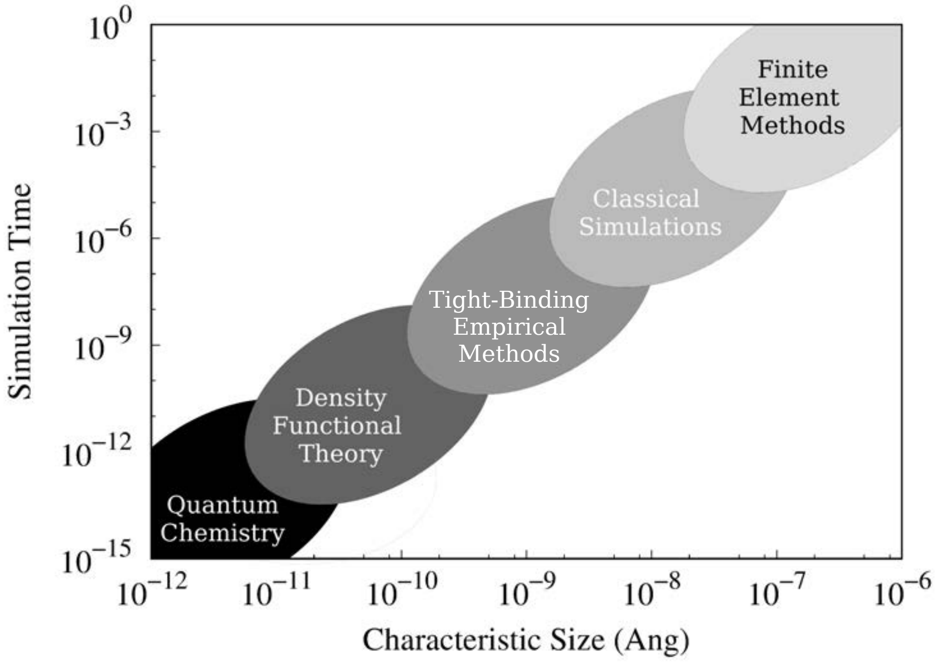

FIGURE 2.1: Characteristic system size vs. characteristic simulation time. Different simulation techniques will be used depending on the characteristic size of the system. As size decreases, quantum effect arise and have to be taken into account.

From the atomistic first principles calculations for transport structures at the microscopic level, to the transistor simulation using a macroscopic vision of the device.

In this chapter, four methodologies will be briefly described: Density Functional Theory and Non-Equilibrium Green Function Theory, Molecular Dynamics and the Finite Element Method. This techniques were used throughout this work in order to simulate and describe different processes and compute certain properties. The choice of the different techniques comes from the size of the system under study. From a macroscopic level, the finite element method for describing the I-V characteristics of a transistor to atomistic modeling for deposition simulations to quantum transport in order to calculate contact resistances. Finally, a short discussion on the codes used throughout this work is presented, dealing with characteristics of its implementation, technical detals and other relevant features of each code.

2.2 Density Functional Theory

The density functional theory was born in the 1960, with the formulation of the Hohenberg-Kohn theorems [40]. These theorems were based on the earlier Thomas-Fermi model [93] from 1927, which is considered the precursor of modern DFT. This theory allowed the prediction and study of new materials not yet available for experimental treatment, as well as a deep understanding of the ground state description of electronic states, in a more theoretical approach.

Like any other theory, DFT has its limits. With DFT it is only possible to find the ground state of the system. Excited states require other treatments of these equations leading to other kinds of problems not described here. These methods are very CPU hungry; therefore, the number of atoms in each simulation is limited by a few hundreds. Different implementations of DFT rely on different approaches such as the base, the pseudopotentials or the numerical schemes used. Each code will be useful for different applications due to the implementation characteristics.

This first section is structured as follows: in the first part a development of the basic equations of quantum mechanics is laid out and worked such that a proper description of the crystal or solid at hand is found. Later, the basic theorems allowing to find a solution to the problem are proposed and briefly discussed. Finally, a note on how the resulting equations are actually solved and a couple of examples of two of the most popular DFT energy functionals are shown as well.

2.2.1 The Schrödinger equation

In the year 1922 the German physicists Otto Stern and Walther Gerlach conducted an experiment [34, 32, 33]. In the Stern-Gerlach experiment silver atoms were sent through an inhomogenous magnetic field that deflected these atoms onto a screen. According to the laws of classical electrodynamics, the atoms should have been deflected according to the gradient of the magnetic field showing a continuous spectrum of deflected atoms. Instead, the screen revealed accumulations of points revealing that quantum effects were present in atomic-scale system. After this, it was clear that a new set of laws were required to describe the behaviour of atom-scale systems. Nowadays, the equations that describe quantum systems are well known.

In particular, the evolution of a system is given by the Schrödinger equation [85],

$$\hat{\mathcal{H}} \left|\Psi(t)\right\rangle = i\hbar \frac{\partial}{\partial t} |\Psi(t)\rangle, \tag{2.1}$$

with i the imaginary unit, $\hbar$ the reduced Planck constant, Ψ the wave function and $\hat{\mathcal{H}}$ the Hamiltonian operator. Equation 2.1, describes the time evolution of a quantum state represented by the ket $|\Psi(t)\rangle$, using Dirac's notation. The wave function is a key concept in quantum mechanics, as it fully describes a quantum system and stores all relevant information. In the subject of this thesis, however, the time dependency will only be considered as a stationary solution,

$$|\Psi(t)\rangle = e^{-i\frac{\epsilon}{\hbar}t}\,|\psi\rangle, \tag{2.2}$$

where all the temporal dependancy is contained in the exponential prefactor. The ϵ represents the energy associated with the wave function. The time evolution of this wave function according to Eq. 2.1 is

$$\hat{\mathcal{H}}\,|\Psi(t)\rangle = i\hbar\frac{\partial}{\partial t}\,|\Psi\rangle = i\hbar\frac{\partial}{\partial t}e^{-i\frac{\epsilon}{\hbar}t}\,|\psi\rangle = \epsilon\,e^{-i\frac{\epsilon}{\hbar}t}\,|\psi\rangle = \epsilon\,|\Psi(t)\rangle \tag{2.3}$$

With this time-dependency on the wave function, Eq. 2.1 turns into an eigenvalue problem of the Hamiltonian, being ϵ its eigenvalue

$$\hat{\mathcal{H}}|\psi\rangle = \epsilon\,|\psi\rangle. \tag{2.4}$$

From the classical mechanics analogy, the Hamiltonian of a system is defined as the sum of the kinetic energy plus the potential energy. As mentioned above, the objective is to find a quantum-mechanical description of solids. This way, the ion positions, electron positions, Coulomb forces, etc . . . have to be taken into account. For this, all these interactions are to be included in the potential of the Hamiltoninan operator. The periodicity and basis of the lattice in which these atoms are arranged will be also taken into account later.

2.2.2 Hamiltonian of a solid

The objective is to find the solution of the Scrödinger equation, the wave functions and energies, for the electrons in the solid. These electrons will be under the influence of the nuclei and electrons themselves. The Hamiltonian of the crystal is thus

$$\begin{aligned}\hat{\mathcal{H}} = &-\frac{\hbar^2}{2m_e}\sum_i \nabla_i^2 - \frac{1}{4\pi\epsilon_0}\sum_{i,I}\frac{Z_I e^2}{|\hat{\mathbf{r}}_i - \hat{\mathbf{R}}_I|} + \frac{1}{4\pi\epsilon_0}\sum_{i\neq j}\frac{e^2}{|\hat{\mathbf{r}}_i - \hat{\mathbf{r}}_j|}\\ &-\sum_I \frac{\hbar^2}{2M_I}\nabla_I^2 + \frac{1}{4\pi\epsilon_0}\sum_{I\neq J}\frac{Z_I Z_J\, e^2}{|\hat{\mathbf{R}}_I - \hat{\mathbf{R}}_J|}.\end{aligned} \tag{2.5}$$

where the lowercase indices apply to electrons and the uppercase indices to ions, following the same notation as in Ref. [59]. The first term is the electron kinetic energy, followed by Coulomb potential between electrons and ions, then the Coulomb potential between electrons themselves. Finally, the nuceli kinetic energy and the last term is the Coulomb potential between ions. Note that $\hat{\mathbf{r}}$ and $\hat{\mathbf{R}}$ are the position operators for electrons and nuclei respectively. Max Born and J. R. Oppenheimer noticed, in 1927, that [7], the inverse of the nuceli term, $1/M_I$, is rather small with respect to the electron term due to the mass of the typical nucleus is ~ 1000 times the mass of the electron. This implies that the kinetic term will be just a perturbation term that can be ignored with respect to the total Hamiltonian of the crystal. Taking into consideration this, the electronic Hamiltonian can be written as

$$\hat{\mathcal{H}}_e = \hat{T} + \hat{V}_{int} + \hat{V}_{ext} + \epsilon_{II}, \tag{2.6}$$

where the potential terms have been grouped. The term $\hat{V}_{int}$ includes the electron-electron interactions, the second term, $\hat{V}_{ext}$, accounts for the electron-nuclei potential and any other external fields and finally the ϵ_{II} term accounts for the nuclei interactioning with one another and any other terms that contribute to the total energy. Writing down the full Scrödinger equation expression 2.7 is obtained.

$$\left[\hat{T} + \hat{V}_{int} + \hat{V}_{ext} + \epsilon_{II}\right] |\Psi\rangle = \epsilon |\Psi\rangle \tag{2.7}$$

Solving this equation is not trivial as the state $|\Psi\rangle$ depends on the $3N$ electron variables where N is the total number of electrons. Theoretically, this is solvable; however, it is not computationally efficient. Instead, in 1965 Walter Kohn and Lu Jeu Sham [47] developed a method to solve these equations by replacing the electronic wave function for the electronic density.

2.2.3 The electron density and the Hohenberg-Kohn Theorems

Before proceding with the Hohenberg-Kohn theorems, let us define the electron density and the energy functional. The density operator is simply $\hat{\rho}(\mathbf{r}) = \sum_i \delta(\mathbf{r} - \mathbf{r}_i)$. The expectation value for any observable, and in particular the electron density, will be

$$\rho(\mathbf{r}) = \frac{\langle\Psi|\hat{\rho}(\mathbf{r})|\Psi\rangle}{\langle\Psi|\Psi\rangle}, \tag{2.8}$$

where Ψ is the electronic wave function. Note that $\int \rho(\mathbf{r})\mathrm{d}\mathbf{r} = N$, the total number of electrons. Finally, the energy functional is defined as

$$E = \frac{\langle\Psi|\hat{\mathcal{H}}|\Psi\rangle}{\langle\Psi|\Psi\rangle} = \langle\hat{T}\rangle + \langle\hat{V}_{int}\rangle + \int \hat{V}_{ext}\, \rho(\mathbf{r})\mathrm{d}\mathbf{r} + \epsilon_{II}. \tag{2.9}$$

The Hohenberg-Kohn theorems [40] ensure that the ground state electronic density carries the same information as the Hamiltonian of the system.

Theorem 1 *The ground-state energy from Schrödinger's equation is a unique functional of the electron density.*

This way, knowing the functional and the electronic density is all that's needed to solve Eq. 2.7 and calculate all relevant properties.

The second Hohenberg-Theorem ensures that the ground state of the functional corresponds to the ground state energy as the solution of the Schrödinger equation

Theorem 2 *The energy functional that minimises the total energy of the system corresponds to the solution of the ground state of the Schrödinger equation.*

This can be done by minimising the expression in 2.9 since the eigenvalues are stationary points of the Hamiltonian.

2.2.4 The Kohn-Sham Equations

The many-body Schrödinger equation is not practically solvable and, the Kohn-Sham approach proposed to replace this by an independent particle problem. The KS approach is based on two assumptions:

- The exact ground state density can be represented by the ground state density of an auxiliary system of non-interacting particles.
- The auxiliary Hamiltonian is chosen to have a standard kinetic energy term plus an effective potential $V^{\sigma}_{eff}(\mathbf{r})$ acting on an electron of spin σ at $\mathbf{r}$.

In Fig. 2.2.4 an schematic representation of this assumption plus the Hohenberg-Kohn theorems is shown for clarity.

$$\begin{tikzcd}
V_{ext}(\mathbf{r}) \arrow[d, Rightarrow] & \rho_0(\mathbf{r}) \arrow[l, Rightarrow, "HK"'] & \rho_0(\mathbf{r}) \arrow[l, Leftrightarrow, "KS"'] \arrow[r, Rightarrow, "HK_0"] & V_{KS}(\mathbf{r}) \arrow[d, Rightarrow] \\
\Psi_i(\{\mathbf{r}\}) \arrow[r, Rightarrow] & \Psi_0(\{\mathbf{r}\}) \arrow[u, Rightarrow] & \psi_{i=1,N_e}(\mathbf{r}) \arrow[u, Rightarrow] & \psi_i(\mathbf{r}) \arrow[l, Rightarrow]
\end{tikzcd}$$

FIGURE 2.2: Schematic representation of the Kohn-Sham *anzatz*. The HK refers to the Hohenberg-Kohn theorems that link V_{ext} with the electron density, while the HK_0 refers to the same theorems applied to the noninteractic problem. Adapted from [59].

This auxiliary Hamiltonian is

$$\hat{\mathcal{H}}^{\sigma}_{\text{KS}} = -\frac{1}{2}\nabla^2 + V^{\sigma}_{\text{KS}}(\mathbf{r}) \tag{2.10}$$

For a system with $N = N_{up} + N_{down}$ independent electrons under this Hamiltonian, the ground state has one electron in each of the N^σ orbitals $\psi_i^\sigma(\mathbf{r})$ with the lowest eigenvalues ϵ_i^σ of the Hamiltonian 2.10. The auxiliary density is given by

$$\rho(\mathbf{r}) = \sum_\sigma \rho(\mathbf{r}, \sigma) = \sum_\sigma \sum_{i=1}^{N^\sigma} |\psi_i^\sigma(\mathbf{r})|^2. \tag{2.11}$$

The independent particle kinetic energy T_s is

$$T_s = -\frac{1}{2} \sum_\sigma \sum_{i=1}^{N^\sigma} \langle \psi_i^\sigma | \nabla^2 | \psi_i^\sigma \rangle = \frac{1}{2} \sum_\sigma \sum_{i=1}^{N^\sigma} |\nabla \psi_i^\sigma|^2. \tag{2.12}$$

The classical Coulomb interaction of the electron density acting on itself is [38]

$$E_{\text{Hartree}}[\rho] = \frac{1}{2} \int \frac{\rho(\mathbf{r})\rho(\mathbf{r'})}{|\mathbf{r} - \mathbf{r'}|} \, \mathbf{dr} \, \mathbf{dr'} \tag{2.13}$$

Finally, the KS approach to the full interacting many-body problem is to rewrite the HK expression for the ground state energy functional in the form

$$E_{\text{KS}} = T_s[\rho] + \int V_{ext}(\mathbf{r})\rho(\mathbf{r}) \, \mathbf{dr} + E_{\text{Hartree}}[\rho] + E_{II} + E_{xc}[\rho]. \tag{2.14}$$

here V_{ext} is the external potential created by nuclei and other external fields independent of spin and E_{II} is the energy interaction between the nuclei. The non trivial many-body effects are all grouped under the exchange-correlation functional E_{xc}. This exchange-correlation functional can be written as

$$E_{xc}[\rho] = \langle \hat{T} \rangle - T_s[\rho] + \langle \hat{V}_{int} \rangle - E_{\text{Hartree}}[\rho]. \tag{2.15}$$

Here, $[\rho]$ denotes a functional of the electron density $\rho(\mathbf{r}, \sigma)$. This exchange-correlation energy functional term is left for further approximation as it has been demonstrated that it must be taken into account for accurate description of the interacting electrons among themselves [58, 102]. Further approximations can be made for this term. For instance, the Local Density Approximation [12, 78] or the Generalized Gradient Approximation [77] are two of the most used approximations to the Exchange-Correlation energy functional in DFT codes. These work with most materials, giving accurate energy descriptions of the materials and systems analyzed.

The Local Density Approximation

For most solids, electrons are reasonably approximated by an homogenous electron gas. This implies that the exchange-correlation energy is simply an integral over all space with this energy to be the same as an homogenous electron gas with that density.

$$\begin{aligned} E_{xc}^{LSDA}[\rho^{\uparrow},\rho^{\downarrow}] &= \int \rho(\mathbf{r})\ \epsilon_{xc}^{hom}(\rho^{\uparrow}(\mathbf{r}),\rho^{\downarrow}(\mathbf{r}))\ \mathbf{dr} \\ &= \int \rho(\mathbf{r})\ \left[\epsilon_{x}^{hom}(\rho^{\uparrow}(\mathbf{r}),\rho^{\downarrow}(\mathbf{r})) + \epsilon_{c}^{hom}(\rho^{\uparrow}(\mathbf{r}),\rho^{\downarrow}(\mathbf{r}))\right]\mathbf{dr}. \end{aligned} \tag{2.16}$$

For unpolarized systmes the LDA is found by setting $\rho^{\uparrow}(\mathbf{r}) = \rho^{\downarrow}(\mathbf{r}) = \rho(\mathbf{r})/2$.

The Generalized Gradient Approximation

The Generalized Gradient Approximation represents an improvement over the L(S)DA functional for many cases. Widely used GGAs can now provide the accuracy required for density functional theory to be widely adopted by the chemistry community. The first step beyond the local approximation is a functional of the magnitude of the gradient of the density $|\nabla\rho^{\sigma}|$ as well as the value of ρ at each point. It is convenient to write the functional as a generalized form of 2.16.

$$E_{xc}^{GGA}[\rho^{\uparrow},\rho^{\downarrow}] = \int \rho(\mathbf{r})\ \epsilon_{xc}(\rho^{\uparrow},\rho^{\downarrow},|\nabla\rho^{\uparrow}|,|\nabla\rho^{\downarrow}|,\dots)\ \mathbf{dr} \tag{2.17}$$

The term generalized-gradient denotes a variety of ways proposed for functions that modify the behaviour at large gradients in such a way as to preserve desired properties.

2.2.5 Hellmann-Feynman Theorem

This theorem [22, 39] relates the derivative of the total energy with respect to a parameter with the expected value of the derivative of the Hamiltonian with respect to that parameter.

Theorem 3 *Given an eigenstate ψ_λ for a Hamiltonian $\hat{\mathcal{H}}$ such that the eigenstates are orthogonal, then*

$$\frac{dE_\lambda}{d\lambda} = \left\langle \psi_\lambda \left| \frac{d\hat{\mathcal{H}}}{d\lambda} \right| \psi_\lambda \right\rangle. \tag{2.18}$$

where λ is a parameter of the Hamiltonian that the state also depends on. Its importance lies in that if we derive the energy with respect to the position **r** we can calulate the force

$$\mathbf{F} = -\frac{\partial E}{\partial \mathbf{R}} = -\left\langle \psi \left| \frac{\partial \hat{\mathcal{H}}}{\partial \mathbf{R}} \right| \psi \right\rangle - \left\langle \frac{\partial \psi}{\partial \mathbf{R}} \left| \hat{\mathcal{H}} \right| \psi \right\rangle - \left\langle \psi \left| \hat{\mathcal{H}} \right| \frac{\partial \psi}{\partial \mathbf{R}} \right\rangle = -\left\langle \frac{\partial \hat{\mathcal{H}}}{\partial \mathbf{R}} \right\rangle \tag{2.19}$$

in the last step the eigenstate of the Hamiltonian was used. Thus, the forces from the ground state can be calculated and therefore it is possible to perform structural relaxations.

2.2.6 Solving the Kohn-Sham equations

As descibed in previous sections, to solve the KS equations, a V_{ext}^{in} such that it will produce a ρ^{out} needs to be provided. However the in density and out density will be different except for the exact solution. In this case, we can use the out density to generate a new potential which, in turn, will produce a new density and so on. This will converge both the density and the potential to its solution after some number of steps. One of the simplest methods to seek convergence of the self consistent iteration is the linear mixing scheme.

$$\rho_{n+1}^{in} = \alpha \rho_n^{out} + (1-\alpha)\, \rho_n^{in} \tag{2.20}$$

where α is the mixing parameter. For rigid systems, strongly bound, large values of alpha makes this scheme converge fast. However, for "soft cases" such as metal surfaces such, convergence can become difficult. Depending on the type of problem, the energy functional used or even the electronic structure of the atoms can make this simple scheme to not converge properly. Beyond this simplistic linear mixing scheme, there is the Pulay mixing scheme [80, 71]. This numerical scheme takes into account the values of the density of the previous N steps. This way, Pulay mixing is given by $\rho_{n+1}^{in} = \alpha \rho_{-n}^{out} + (1-\alpha)\, \rho_{-n}^{in}$, where

$$\rho_{-n}^{out} = \sum_{i=1}^{N} \beta_i \rho_{out}^{(n-N+i)},\ \rho_{-n}^{in} = \sum_{i=1}^{N} \beta_i \rho_{in}^{(n-N+i)}. \tag{2.21}$$

The values of β_i are obtained by minimizing the distance between ρ_{-n}^{out} and ρ_{-n}^{in} and α is the mixing weight. Note that for $N = 1$ this reduces to the linear mixing of Eq. 2.20. Furthermore, the Broyden method [11] is another widely used convergence accelerator that also takes into account the history of the previous steps. This method is even more general than the Pulay mixing and, in fact, the Pulay mixing is a particular case of the Broyden method.

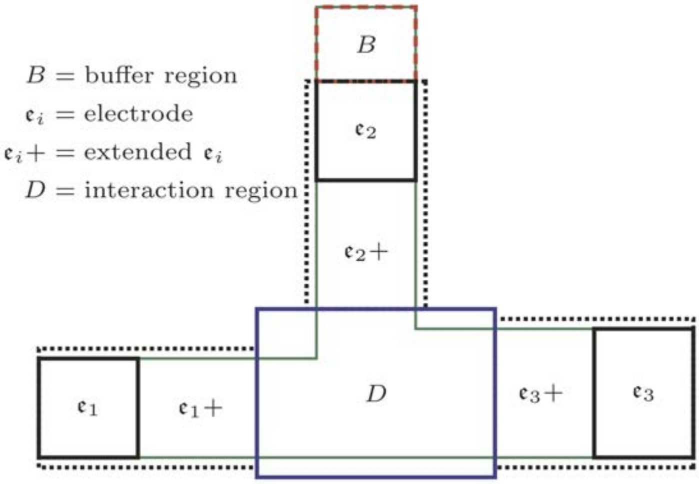

FIGURE 2.3: Transport setup. The system consists of three different electrodes, or leads as it is often referred in the literature, and a scattering zone in which electrons will be either scattered, reflected or transmitted. Electrode setup for $N_e = 3$ as example. Adapted from [74]

2.3 Electronic Transport

In the previous section 2.2, it was shown how to obtain and what are the wave functions and energies of the ground state of a given system in equilibrium. However, this is not always the case in real-like systems. In this section the study of electronic transport be will briefly reviewed with the Non-Equilibrium Green's Theory. The transport configuration that are usually studied for in the solid state systems is described in Fig. 2.3. Three electrodes in which electrons are injected or absorbed and a scattering zone where electrons will either and scatter. For simplicity, all electrons will be accounted for *i.e.* no electrons will be allowed to stay in the scattering zone or will be allowed to scape for tunneling effects or similar. This general system will be later used to analyze the equations that describe transport in the quantum world (see Sec. 2.3.2).

2.3.1 Conductance and the Landauer Formula

Conductance is a quantity related to the material properties and geometry. Classically it is defined as

$$G = \sigma \frac{A}{\ell} \tag{2.22}$$

where σ is the conductivity of the material, A the transversal area and ℓ the length of the device. So naturally, when studying electronic devices this quantity is of particular interest. This formula, however, only holds for macroscopic systems. As the size of the system is reduced quantum effects arise and they have to be accounted for. The Landauer Formula [50] relates the quantum conductance with the transmission coefficients.

$$G(\varepsilon) = \frac{e^2}{h} T(\varepsilon)M(\epsilon) \tag{2.23}$$

where e is the electron charge, h the Planck constant, $T(\varepsilon)$ the transmission coefficient as a function of the energy and $M(\epsilon)$ the number of spin polarized modes. By solving the transport problem from the electronics point of view is by calculating the transmission coefficients.

2.3.2 Scattering Theory

In this section the time-independent scattering theory is going to be briefly discussed. For starters, consider the scattering Hamiltonian:

$$\hat{\mathcal{H}} = \hat{\mathcal{H}}_0 + \hat{V} \tag{2.24}$$

where $\hat{\mathcal{H}}_0$ is the Hamiltonian operator of the unperturbed states. Here, the presence of the scattering potential $\hat{V}$ causes incoming states to scatter to another lead. If the scattering is elastic it means that the energy of the states do not change, which is what will be considered here. Otherwise, an inelastic scattering event takes place. Consider an eigenket of the Hamiltonian

$$\hat{\mathcal{H}}_0|\phi_0\rangle = \varepsilon|\phi_0\rangle.$$

The goal is to find a solution for the full Schrödinger equation,

$$\left(\hat{\mathcal{H}}_0 + \hat{V}\right)|\psi\rangle = \varepsilon|\psi\rangle \ \rightarrow \ \left(\hat{\mathcal{H}}_0 - \varepsilon\right)|\psi\rangle = \hat{V}|\psi\rangle. \tag{2.25}$$

For scattering states, the solution has to satisfy

$$|\psi\rangle \rightarrow |\phi_0\rangle \text{ when } \hat{V} \rightarrow 0$$

A naive approach to this would be to state that the solution is

$$|\psi\rangle = |\phi_0\rangle + \frac{1}{\hat{\mathcal{H}}_0 - \varepsilon}\hat{V}|\phi_0\rangle, \tag{2.26}$$

but this operator has a singularity on the eigenstates of $\hat{\mathcal{H}}_0$. To go around the singularity, an infinitessimal quantity is added in order to shift the operator to the complex plane. At the end of the calculation, this infinitessimal quantity will be taken to be zero. A formal solution of this equation satisfies

$$|\psi\rangle = |\phi_0\rangle + \frac{1}{\hat{\mathcal{H}}_0 - \varepsilon \pm i\eta}\hat{V}|\phi_0\rangle, \tag{2.27}$$

which is known as the Lippmann-Schwinger Equation [55]. Now, the Green Operator is defined as follows

$$\hat{G}^{\pm}(\varepsilon) \equiv \lim_{\eta\to 0^+}\left(\hat{\mathcal{H}} - \varepsilon \pm i\eta\right)^{-1}. \tag{2.28}$$

The ± sign denotes the advanced $(+)$ or retarded $(-)$ Green operator and by definition both are related by the expression

$$\hat{G}^{+}(\varepsilon) = \left[\hat{G}^{-}(\varepsilon)\right]^{\dagger} \tag{2.29}$$

since the Hamiltonian is an hermitic operator and the eigenvalues of a hermitian operator are real.

Example: ***The Poisson Equation***

The poisson equation is $\nabla^2\phi = \rho/\epsilon_0$. The corresponding Green Function for this equation is $G(\mathbf{r},\mathbf{r'}) = 1/4\pi\epsilon_0|\mathbf{r}-\mathbf{r'}|$, and its general solution is the well known composition of point charge electric potential is

$$\phi(\mathbf{r}) = \int \rho(\mathbf{r'})G(\mathbf{r},\mathbf{r'})\mathrm{d}\mathbf{r'} = \frac{1}{4\pi\epsilon_0}\int \frac{\rho(\mathbf{r'})}{|\mathbf{r}-\mathbf{r'}|}\mathrm{d}\mathbf{r'}.$$

Now, let's think about the transport system from an atomistic point of view [8]. In this representation, each atom site is a binding state tied to the atomic positions. Each incoming state from electrode e can be written in terms of this unperturbed binding states as

$$|\psi^e\rangle = \sum_{\mu} c_{e\mu}|\phi^e_{\mu}\rangle \tag{2.30}$$

From this it is let's re-write Eq. 2.27 expanding the scattered states in terms of this binding states,

$$c_{e\mu} = c^0_{e\mu} + \sum_{\nu} \left(\hat{G}(\varepsilon)\hat{V}\right)_{\mu\nu} c^0_{e\mu}. \tag{2.31}$$

The superindex ^{0} represents the coefficient for the unperturbed states for the potential $\hat{V}$. The coefficients $c^0_{e\mu}$ vanish in the scattering region, therefore

$$c_{e\mu} = \sum_{\nu} \left(\hat{G}(\varepsilon)\hat{V}\right)_{\mu\nu} c^0_{e\mu}. \tag{2.32}$$

The density matrix for incoming states, considering that states coming from deep in the electrodes are filled up to the electrochemical potential of the electrode μ_e, will be

$$\hat{\rho} = \sum_{e}^{N_e} \sum_{s}^{N_s} |\psi^s\rangle\langle\psi^s|\, n_F(\varepsilon_s - \mu_e), \tag{2.33}$$

where the index e runs over all electrodes, N_e is the total number of electrodes, and s over all states in the electrode, being N_s the total number of states in the corresponding electrode. Now, the density matrix can also be written in terms of this binding states, therefore the elements of the density matrix are

$$\hat{\rho}_{\mu\nu} = \sum_{e}^{N_e} \sum_{s}^{N_s} c_{s\mu} c^*_{s\nu} n_F(\varepsilon_s - \mu_e) \tag{2.34}$$

Since the electrodes do not interact with each other directly, only through the scattering regions, from this point on only the derivation will be done for one electrode. It is convenient, for reasons that will be aparent later, to introduce the spectral density matrix

$$\mathcal{A}^e_{\mu\nu} = \sum_{s}^{N_s} c_{s\mu} c^*_{s\nu}\, \delta(\varepsilon - \varepsilon_s). \tag{2.35}$$

Now, this spectral density operator can be re-written in terms of the binding states from Eq. 2.32

$$\mathcal{A}^e_{\mu\nu} = \left(\hat{G}(\varepsilon)\frac{1}{\pi}\mathrm{Im}\left[\hat{V}\hat{g}^e(\varepsilon)\hat{V}^\dagger\right] G^\dagger(\varepsilon)\right)_{\mu\nu} \tag{2.36}$$

where $\hat{g}^e(\varepsilon)$ is defined as

$$\hat{g}^e_{\mu\nu}(\varepsilon) = \sum_{s} \frac{c^0_{s\mu} c^{0\,*}_{s\nu}}{\varepsilon - \varepsilon_s \pm i\epsilon} \tag{2.37}$$

From this, the following quantities can be identified:

$$\Sigma_e(\varepsilon) \equiv \left[\hat{V}\hat{g}^e(\varepsilon)\hat{V}^\dagger\right], \tag{2.38}$$

$$\Gamma_e(\epsilon) \equiv \frac{i}{2}\left[\Sigma_e(\varepsilon) - \Sigma_e^\dagger(\varepsilon)\right], \tag{2.39}$$

where Σ_e can be identified as the self-energy on electrode e. Finally, the spectral density matrix can be written in terms of these quantities,

$$\mathcal{A}^e_{\mu\nu} = \frac{1}{\pi}\left[\hat{G}(\varepsilon)\Gamma_e(\varepsilon)\hat{G}^\dagger(\varepsilon)\right]_{\mu\nu}. \tag{2.40}$$

In equilibrium, the left and right parts of the density matrix can be combined:

$$\begin{aligned}\hat{G}\,\Gamma\,\hat{G}^\dagger &= \frac{i}{2}\hat{G}\left[\Sigma - \Sigma^\dagger\right]\hat{G}^\dagger \\ &= -\frac{i}{2}\hat{G}\left[\hat{G}^{-1} - (\hat{G}^\dagger)^{-1}\right]\hat{G}^\dagger \\ &= -\frac{1}{\pi}\mathrm{Im}\left[\hat{G}\right].\end{aligned} \tag{2.41}$$

Now, the density matrix can be written in terms of the Green's Operator in equilibrium as

$$\begin{aligned}\hat{\rho} &= -\frac{1}{\pi}\int_{-\infty}^{+\infty}\mathrm{Im}\left[\hat{G}(\varepsilon)\;n_F(\epsilon-\mu)\right] \\ &= -\frac{1}{\pi}\mathrm{Im}\left[\int_{-\infty}^{+\infty}\hat{G}(\varepsilon)\;n_F(\epsilon-\mu)\;\mathrm{d}\varepsilon\right].\end{aligned} \tag{2.42}$$

In equilibrium, this is not an improvement with respect to Eq. 2.33. But in the case of non zero bias calculations, this expression relates the newly introduced operators with the unperturbed electrodes through the evaluation of this integral. This integral is evaluated via contour integration using the Residue theorem. An analysis on the Green's Operator in the complex plane reveals that it is rapidly varying near the poles in the real axis but very smooth in the complex plane which allows for accurate quadrature methods.

Finally, the transmission coefficients can be calculated with the scattering matrix formalism using the Green Function via the Fisher-Lee relations [24]. The matrix elements of the S-Matrix can be written for two electrodes e and e' as [74]

$$s_{ee'}(\varepsilon) = -\delta_{ee'} + i[\Gamma_e(\varepsilon)]^{\frac{1}{2}}\;\hat{G}(\varepsilon)\;[\Gamma_{e'}(\varepsilon)]^{\frac{1}{2}} \tag{2.43}$$

where the subscripts refer to two different electrodes. Finally, the transmission coefficients from electrode e to e' is

$$T_{ee'}(\varepsilon) = \mathrm{Tr}\left[s^{\dagger}_{ee'}(\varepsilon)s_{ee'}(\varepsilon)\right] \tag{2.44}$$

or the aggregate transmission out from en electrode e

$$\begin{aligned} T_e(\varepsilon) &= \sum_{e\neq e'} T_{ee'}(\varepsilon) \\ &= i\ \mathrm{Tr}\left[(\hat{G}(\varepsilon) - \hat{G}^{\dagger}(\varepsilon))\Gamma_e(\varepsilon)\right] - \mathrm{Tr}\left[\hat{G}(\varepsilon)\Gamma_e(\varepsilon)\hat{G}^{\dagger}(\varepsilon)\Gamma_e(\varepsilon)\right]. \end{aligned} \tag{2.45}$$

Taking a look into the literature to find a physical interpretation of the Green Operator it is found that according to S. Datta [17], "The Green's function describes the coherent propagation of an injected electron. Any time the electron exits into a lead (electrode), or interacts with its surroundings, the coherent evolution is over". The Green operator is often also called a propagator as it describes the propagation of an electron from an initial state $|i\rangle$ into a final state $|f\rangle$, *i.e.*

$$\langle f|\hat{G}^{+}(t)|i\rangle = \langle i|\hat{G}^{-}(-t)|f\rangle^{*}, \tag{2.46}$$

So note that taking the complex conjugate of the same quantity leads to a totally different interpretation of the Green operator. This time, the sate $|f\rangle$ is propagating into state $|i\rangle$, instead. Hence, the different meanings of the advanced and retarded Green's operators. The retarded Green's operator describes the propagation in time of one initial state to a final state, while the advanced Green's operator describes an electron, for example, that suddenly becomes coherent and goes back into the electrode.

2.4 Molecular Dynamics

Molecular Dynamics is a computational technique for computing transport and equilibrium properties of a classical many-body system. This means integrating Newton's equation of motion. This allows for the study of different systems under different conditions: constant temperature, pressure, energy, mass, etc... It is referred as classical, in comparison with the previous section, because the equations that are begin solved are the classical Newton's Equations of motion. Even though the forces and equations of motion are treated classically, the energy description between particles is where the physical meaning of the system is hidden and should capture the most important quantum features.

In this section the basic features of MD are going to be laid out. While all the parts of the basic algorithm are important, the focus of this work has been on the force field. Then, the equations of motion and its solution will be solved using a simple algorithm. Following this, the core of the MD method, the force field, is explained. Then a quick review of how the sampling over some important quantities as an example are discussed. Finally, a discussion on the Bond Order Potential force field is laid out along with a justification of the use for this force field for the calculations carried out in this work.

2.4.1 Basics of Molecular Dynamics

The basic algorithm of any Molecular Dynamics code will follow a similar structure. Different implementations will offer different features and different advantages of the problem at hand. In simple terms all codes will follow this structure, as described in [28].

```
def programMD():
  init()
  t=0
  while(t < tmax):
    force(f, en)
    integrate(f, en)
    t += delt
  sample()
  return
```

This program will perform the following steps. The first thing that has to be done is to call the init subroutine. `init()` is the initialisation subroutine in which sets all initial positions, velocities and Energy and will initialize all other relevant quantities and then the global timer will be set to 0. The `force()` function will calculate all the forces between all possible pairs of particles according to some force field as described in section 2.4.2. Then, the `integrate()` subroutine will integrate the equations of motion for all particles and set the new positions at the next timestep, described in section 2.4.3. After this, the global time of the simulation will be increased by a certain amount defined previously and the loop will jump to the next iteration until the maximum time allowed for the simulation is reached. After this, the `sample()` subroutine will calculate important quantities relevant to the simulation being studied, as explained in section 2.4.4.

As mentioned above, all Molecular Dynamics programs will follow this basic structure while they can offer different numerical schemes for integration, different force calculations for different force fields or perform different sampling on the system. It is worth mentioning that there are, also, hybrid methods in which a combination of DFT and MD is used to move the particles classically while calculating the forces from a quantum mechanical point of view [61]. Other codes allow the mixing of both methods: Using quantum mechanics for certain parts of the system while treating the rest classically [60].

2.4.2 Force fields

At each time step the equations of motion are integrated and particles are moved according to some force. This force is calculated from the potential energy between two particles, $u(\mathbf{r})$. In molecular dynamics the parameter matrix that describes the interaction between two particles along with the analytical form to calculate the potential energy between two particles is called a force field. This allows the calculation of forces between particles using whatever models or expressions that are fit for the atom types present in the simulation. Classically, the force of a particle in a classical potential is given by

$$F = -\frac{\mathrm{d}u(\mathbf{r})}{\mathrm{d}\mathbf{r}}. \tag{2.47}$$

Each particle will be under the presence of a force field created by all other particles. All the physics and description of the different particles will be defined with this potential $u(\mathbf{r})$. Usually, the same force field is used by all particles and there is a set of parameters, along with a set of mixing rules that change for each interaction. To illustrate this, one of the most simple yet widely used for certain simulations is the Lennard-Jones 6-12 potential [52].

$$u(r) = 4\epsilon\left[\left(\frac{\sigma}{r}\right)^{12} - \left(\frac{\sigma}{r}\right)^{6}\right]. \tag{2.48}$$

In broad terms, and among other energy contributions, all potentials will have a repulsive and an attractive part. In this case, it is trivial to identify: the r^{-6} term represents the attractive part and the r^{-12} term, the repulsive part. For this particular case, the two parameters that describe the potential well are ϵ and σ which have a physical interpretation in terms of the potential. The first determines the depth of the potential well as pictured in Fig. 2.4, and the second represents the distance at which the potential goes from attractive to repulsive. Finally, a cutoff function or cutoff radius has to be included. It is not computationally possible nor efficient to compute all the forces between all the particle pairs at each time step as

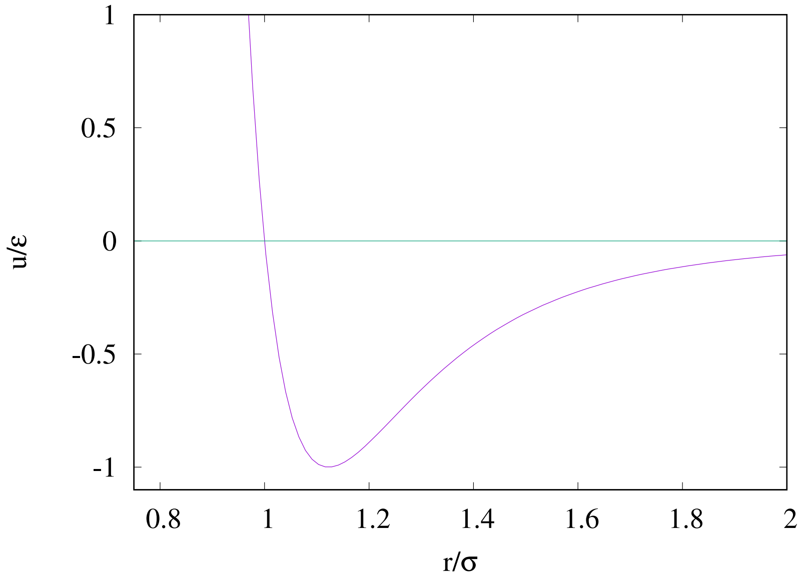

FIGURE 2.4: Lennard-Jones 6-12 potential in reduced units. Notice that the depth of the well is at $(-1, 2^{\frac{1}{6}})$ as defined by the potential's parameters.

this scales as $\mathcal{O}(n^2)$. This way, the potential can be written as

$$u_C(r) = \begin{cases} u(r), & r \leq r_C \\ 0, & r > r_C \end{cases} \tag{2.49}$$

with three effective parameters. This is a very simple potential that allows to showcase basic properties and features of force fields. For different type of particles in a MD simulation, different sets of parameters will be defined within the simulation. Sometimes, cross terms between different types of particles will be defined through a set of mixing rules such that the corss terms are calculated.

2.4.3 Equations of motion

After having calculated the forces, all that is left to do is the actual integration of Newton's Second Law [101]

$$\mathbf{F} = \frac{\mathrm{d}p}{\mathrm{d}t} = m\frac{\mathbf{dp}}{\mathbf{dt}} \tag{2.50}$$

Assuming constant mass, the classical momentum is simply $p = m \cdot v$. One of the simplest algorithms to integrate this differential equation is to take the Taylor's expantion around t

for a small enough Δt

$$r(t+\Delta t) = r(t) + v(t)\Delta t + \frac{F(t)}{2m}\Delta t^2 + \frac{\Delta t^3}{3!}\dddot{r} + \mathcal{O}(\Delta t^4) \tag{2.51}$$

and

$$r(t-\Delta t) = r(t) - v(t)\Delta t + \frac{F(t)}{2m}\Delta t^2 - \frac{\Delta t^3}{3!}\dddot{r} + \mathcal{O}(\Delta t^4) \tag{2.52}$$

summing Eqs. 2.51 and 2.52:

$$r(t+\Delta t) + r(t-\Delta t) = 2r(t) + \frac{F(t)}{m}\Delta t^2 + \mathcal{O}(\Delta t^4) \tag{2.53}$$

or

$$r(t+\Delta t) \approx 2r(t) - r(t-\Delta t) + \frac{F(t)}{m}\Delta t^2. \tag{2.54}$$

Finally, the obtained equation it is nothing more than Euler's formula for integrating differential equations. This equation gives the new position of a particle after a time Δt with errors of the order of Δt^4. This is the simplest approach for integrating the equations of motion. However, there are higher order numerical schemes that would be more computationally efficient and would converge faster, but will not be mentioned in this text.

2.4.4 Sampling

Finally, the last step on the generic MD algorithm is the sampling. Sampling allows the analysis of the system besides looking at equilibrium positions or final geometry. Plus, some of the properties of the system cannot be calculated directly and further calculations are needed. In this section two sampling quantities are being examined: The Radial Distribution Function (RDF) and the Mean Squared Displacements (MSD). Both of this quantities measure correlations, one within space and the other within time.

The Radial Distrubution Function.

The radial distribution function, is a distribution that gives information about the distribution, in space, of the position of the particles. So this distribution is $g(\mathbf{r})\mathrm{d}\mathbf{r}$ = Number of atoms in the shell at **r** with thickness d**r**. With this, we can write

$$\int_0^\infty g(\mathbf{r})\mathrm{d}\mathbf{r} = 4\pi \int_0^\infty \rho(\mathbf{r})\ \mathbf{r}^2\ \mathrm{d}\mathbf{r} \tag{2.55}$$

where ρ is the particle density in a volume V, N the total number of particles and r_C the cutoff radius. An example of this with a 2D Lennard-Jonnes Crystal is on figure 2.5.

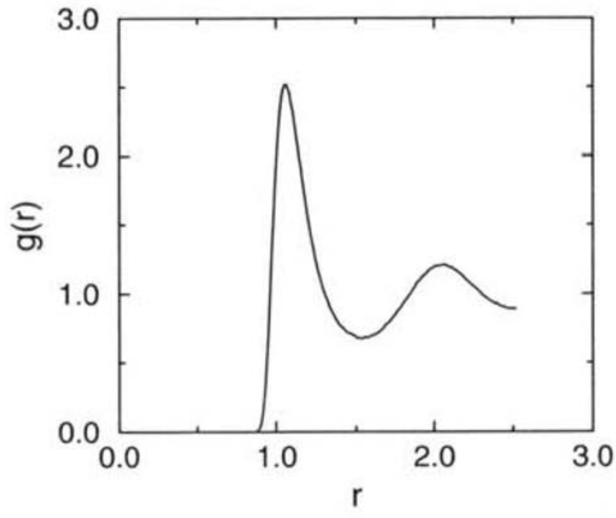

FIGURE 2.5: Lennard-Jones 2D Crystal Radial Distribution Function at $T = 1.54$ and $\rho = 0.8442$ (reduced units). Figure extracted from Ref. [28].

Mean Squared Displacements.

Spacial and Temporal Correlations

$$\left\langle r^2(t) \right\rangle = \left\langle (r - r_0)^2 \right\rangle = \frac{1}{T} \sum_{t=1}^{T} (r(t) - r_0)^2 \tag{2.56}$$

where r_0 is a reference position that can be either a initial position or the mean position $\bar{r}$. For instance, it is possible to calculate the difusion coefficient from this quantity. It can be shown that the relation between the MSD and the difusion coefficient is

$$\left\langle r^2(t) \right\rangle = 2D\, t \tag{2.57}$$

where D is the difusion coefficient and t is the time. For a 2D LJ system, this plot looks like 2.6.

2.5 Finite Elements Methods

The treatment of large devices, compared with the previous methods discussed earlier, an atomistic representations of them is not suitable for computer simulation. Instead, these devices are constituted from different parts that belong to different materials with different

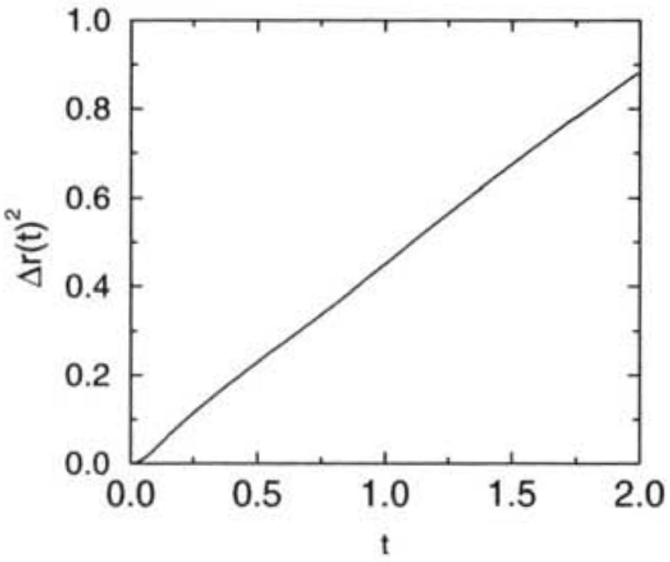

FIGURE 2.6: Mean Squared Displacements as a function of the simulation time. Figure extracted from Ref.[28].

properties, namely: semiconductors, conductors and insulators. The physics description for these materials will be discussed later on chapter 3. But in the end a set of partial differential equations has to be solved to find the quantities relevant for this problem. In conjunction to this, difficult geometries, or difficult boundary conditions, are not typically solvable by means of traditional methods. The Finite Elements Method is anumerical scheme for solving a set of partial differential equations in an arbitrary geometry with any boundary conditions. In this chapter the basics of this theory will be described in general.

2.5.1 General Partial Differential Equation problem

Let $\mathcal{A}$ and $\mathcal{B}$ be two differential operators of order n and $n-1$ that act on a function u. Then a set of differential equations can be written as

$$\mathcal{A}(\mathbf{u}) = \begin{pmatrix} A_1(\mathbf{u}) \\ A_2(\mathbf{u}) \\ \vdots \end{pmatrix} = 0 \tag{2.58}$$

in a domain Ω. The boundary conditions can be written as

$$\mathcal{B}(\mathbf{u}) = \begin{pmatrix} B_1(\mathbf{u}) \\ B_2(\mathbf{u}) \\ \vdots \end{pmatrix} = 0, \tag{2.59}$$

on the boundary of the domain, $\Gamma \equiv \partial\Omega$. This is the statement for a general problem which involves almost any kind of differential equation. The Finite Element process begins with approximating the solution $\mathbf{u}$ as

$$\mathbf{u} \approx \hat{\mathbf{u}} = \sum_{a=1}^{n} \mathbf{N}_a \tilde{u}_a = \mathbf{N}\tilde{\mathbf{u}} \tag{2.60}$$

where $\mathbf{N}_a$ are the shape functions defined locally that depend on independent variables and $\tilde{u}_a$ unknown coefficients.

2.5.2 Integral formulation

From Eq. 2.58 it follows, considering that the set of differential equations has to be zero at each point of the domain Ω, that

$$\int_\Omega \mathbf{v}^T \mathcal{A}(\mathbf{u}) \mathrm{d}\Omega \equiv \int_\Omega \left[v_1 A_1(\mathbf{u}) + v_2 A_2(\mathbf{u}) + \ldots \right] \mathrm{d}\Omega \equiv 0 \tag{2.61}$$

where

$$\mathbf{v} = \begin{pmatrix} v_1 \\ v_2 \\ \vdots \end{pmatrix} \tag{2.62}$$

is a set of arbitrary functions with same number of componens as $\mathbf{u}$. If Eq. 2.61 is satisfied for all $\mathbf{v}$, then 2.58 must be satisfied for all points. A proof of the previous statement can be found supposing $\mathcal{A}(\mathbf{u}) \neq 0$ then the set of arbitrary functions may be found and the integral 2.61 is non-zero. If theboundary conditions have to be simultaneously satisfied, it is required that

$$\int_\Gamma \tilde{\mathbf{v}}^T \mathcal{B}(\mathbf{u}) \mathrm{d}\Gamma \equiv \int_\Gamma \left[\tilde{v}_1 B_1(\mathbf{u}) + \tilde{v}_2 B_2(\mathbf{u}) + \ldots \right] \mathrm{d}\Gamma \equiv 0 \tag{2.63}$$

for any set of arbitrary functions $\tilde{v}$. Then the integral statement that

$$\int_\Omega \mathbf{v}^T \mathcal{A}(\mathbf{u}) \mathrm{d}\Omega + \int_\Gamma \tilde{\mathbf{v}}^T \mathcal{B}(\mathbf{u}) \, \mathrm{d}\Gamma = 0 \tag{2.64}$$

is satisfied for all $\mathbf{v}$ and $\tilde{\mathbf{v}}$ is equivalent to the differential equation in 2.58 and their boundary conditions 2.59. It was assumed that the integrals above are possible to be evaluated, so the set of arbirary functions must be chosen in such a way that the integrals are finite.

The continuity of the solution will depend on the operators $\mathcal{A}$ and $\mathcal{B}$. Assuming that the order of $\mathcal{A}$ is n, then $\mathbf{u} \in C_{n-1}$[1]. Equation 2.64 can be integrated by parts and this will decrease the required continuity of the unknown by one and increase it for the set of arbitrary functions.

2.6 Approximation to integral formulations: the Galerkin-weighted method

In general it is not possible to satisfy both the system 2.58 and its boundary conditions 2.59 with the approximation 2.60. However, the integral statements allow for further approximations if a set of finite functions is put in place of any function $\mathbf{v}$,

$$\mathbf{v} \approx \sum_{b=1}^{n} \mathbf{w}_b \delta\tilde{u}_b \text{ and } \tilde{\mathbf{v}} = \sum_{b=1}^{n} \bar{\mathbf{w}}_b \delta\tilde{u}_b \tag{2.65}$$

with $\delta\tilde{u}_b$ being arbitrary parameters. Inserting this approximations to 2.64 the following expression is found

$$\delta\tilde{u}_b \left[\int_\Omega \mathbf{w}_b^T \mathcal{A}(\mathbf{N}\tilde{\mathbf{u}})\, \mathrm{d}\Omega \; + \int_\Gamma \bar{\mathbf{w}}_b{}^T \mathcal{B}(\mathbf{N}\tilde{\mathbf{u}})\, \mathrm{d}\Gamma \right] = 0 \tag{2.66}$$

Since the parameters $\delta\tilde{u}_b$ are arbitrary, they can be dropped off and the integral statement still holds

$$\int_\Omega \mathbf{w}_b^T \mathcal{A}(\mathbf{N}\tilde{\mathbf{u}})\, \mathrm{d}\Omega + \int_\Gamma \bar{\mathbf{w}}_b{}^T \mathcal{B}(\mathbf{N}\tilde{\mathbf{u}})\, \mathrm{d}\Gamma = 0, \;\; b = 1, \ldots, n \tag{2.67}$$

Now, integrating by parts

$$\int_\Omega \mathcal{C}(\mathbf{w}_b)^T \mathcal{D}(\mathbf{N}\tilde{\mathbf{u}})\, \mathrm{d}\Omega + \int_\Gamma \mathcal{E}(\bar{\mathbf{w}}_b)^T \mathcal{F}(\mathbf{N}\tilde{\mathbf{u}})\, \mathrm{d}\Gamma = 0, \;\; b = 1, \ldots, n \tag{2.68}$$

Now the quantity $\mathcal{A}(\mathbf{N}\tilde{\mathbf{u}})$ represents the *residual or error* obtained by substitution of the approximation into the differential equation, and $\mathcal{B}(\mathbf{N}\tilde{\mathbf{u}})$ the residual on the boundary. The integral equation 2.67 is the weighted integral of such residuals. Almost any set of independent functions $\mathbf{w}_b$ could be used. Depending on the choice it gets a different name

1. Point Collection. $\mathbf{w}_b = \delta_b$ where δ_b is such that for $x \neq x_b; y \neq y_b$, $\mathbf{w}_b = 0$ but $\int_\Omega \mathbf{w}_b \mathrm{d}\Omega = \mathbf{1}$. This choice is equivalent to make the residuals zero at n points within

---

[1] C_k is the set of all continuous functions derivables at least k times.

the domain and integration is nominal. Finite Differences methods are particular cases of this weighting.

2. Subdomain collocation. $\mathbf{w}_b = \mathbf{1}$ in subdomain Ω_b and zero elsewhere. Makes the integral of the error zero over the specified subdomains. This is one of the main Finite Volume methods.

3. The Galerkin Method. $\mathbf{w}_b = \mathbf{N}_b$. The Galerkin Method is only a particular case of weighted residual method.

2.6.1 Weight function

In the case of the Galerkin method the weight function used is $\mathbf{w}_b = \mathbf{N}_b$. These are known for the name of tent functions. In one dimension this function is

$$N_b(x) = \begin{cases} \frac{x-x_{b-1}}{x_b-x_{b-1}} & \text{if } x \in [x_{b-1}, x_b] \\ \frac{x_{b+1}-x}{x_{b+1}-x_b} & \text{if } x \in [x_b, x_{b+1}] \\ 0 & \text{Otherwise} \end{cases} \tag{2.69}$$

with $b = 1, 2, \ldots, n$ where n is the total number of subdomains in the problem. Figure 2.7 shows a one dimensional representation of the tent weight function. This is just a summary of the Finite Element Method. For further details on this subject refer to [109].

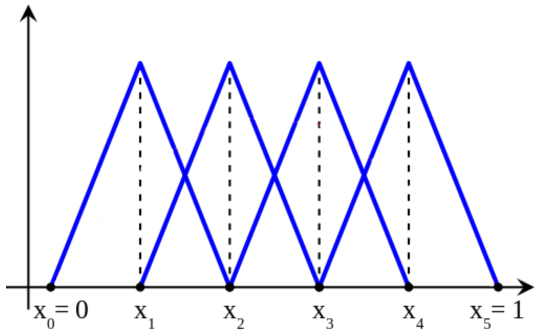

FIGURE 2.7: Tent function in a one dimensional representation

2.7 Software

Theoretical works benefit from the rising on computational power to carry out larger and more accurate calculations. In this brief section a description of the codes and programs used throughout this thesis will be explained. Different codes offer different characteristics and different options for different applications. The choice of such programs depends on the specific application for the situation at hand. Several codes have been used in this work like the SIESTA package, which includes TRANSIESTA, LAMMPS, the Silvaco TCAD suite and VMD, among others.

2.7.1 The SIESTA package

The SIESTA package [87] is a DFT code that uses a Linear Combination of Atomic Orbitals (LCAO) and a multiple-ζ plus polarization basis set. The core electrons have been dealt with non-relativistic norm-conserving pseudopotentials. This code allows for the calculation of the ground state of any system with arbitrary geometry using a localized base atomic set which reduces the amount of wave functions needed for the basis, compared to other planar wave codes, which in turn reduces the use of memory, and makes the computation faster.

The TRANSIESTA [11] code is part of this package and implements the Non-Equilibrium Green's Function theory that allows for the calculation of ballistic electron transport in conditions of non-equilibrium such as a finite voltage, transport through different atomistic structures and calculations with multi-terminal devices [8] which allows to perform structural relaxations, total energy calculations, small voltage simulations and finally ballistic electron transport. This package includes a variety of utilities for analising results. In particular, the TBtrans utility is a Tight Binding code that calculates transmission coefficients for different devices from the TranSiesta output files,

2.7.2 LAMMPS

LAMMPS stands for Large-scale Atomic/Molecular Massively Parallel Simulator and it was developed by S. Plimpton at Sandia Labs [79]. LAMMPS is a classical molecular dynamics simulator which implements parallel algorithms for performance optimisation. It implements a large amount of different force fields, different features, and allows for the sampling of many relevant quantities.

2.7.3 The SILVACO TCAD software

The SILVACO TCAD is a software for the desing, processing and performance simulation of electronic devices that implements the finite element method for solving the semiconductor equations in different materials with arbitrary geometry. It allows for the design of a device, in this case a transistor, the calculation of output characteristics, and has a large library of most used models and materials in the semiconductor industry.

2.7.4 VMD

VMD is a Molecular visualization program [41] for displaying, analyzing and animating molecular systems Using a 3D graphics built-in scripting. This program has been used throughout this thesis in order to visualize the atomistic structures shown in this document.

Chapter 3

Drift Difusion Simulation of 2D based devices

3.1 Introduction

The simulation of electronic devices can be achieved through different models and techniques. In this chapter, the Finite Element Method was chosen so that the geometry of realistic 2D-channel devices could be taken into account as well as model the different novel materials used in Field Effect Transistors such as HfO_2 and MoS_2. These kind of devices show a behaviour that follows the Drift Diffusion model for semiconductors as opposed to ballistic devices such as the ones studied in chapter 5.

This chapter is structured as follows: first, the semiconductor equations reviewed. Then, the material modelling for the use in the FEM software, the minimal set of parameters needed to describe the material. Finally, results from the studied devices as well as some improvements on the results presented in [43]. This chapter is a continuation of the work done in Ref. [43].

3.2 Semiconductor Equations

The basic equations that describe the behaviour of a semiconductor at the microscopic level are presented in this section using quantum mechanics, statistical mechanics and few classical arguments. Throughout this section, the steady state will be considered, hence all time derivatives will vanish. This model describes the movement of electrons in

3.2.1 Poisson's Equation, integral form

Poisson's equation allow the calculation of the electric potential as it relates to the charge distribution.

$$\nabla \cdot [\varepsilon \, \nabla \phi] = -q \, (C - n + p) \, , \tag{3.1}$$

Where ϕ is the electrostatic potential, q is the elemental charge, ε is the dielectric constant, n and p the intrinsic, electron and hole concentrations and C the total charge due to ionized donors and aceptors. The electric field is related to the electrostatic potential by

$$\nabla \times \mathbf{E} = 0 \; \Rightarrow \; \mathbf{E} = -\nabla \phi \tag{3.2}$$

where **E** is the electric field and, by definition, is a conservative field. It is assumed and required that the solution of Poisson's is continuous up to the second derivative, $\phi \in C_2$. This equation can also be written in temrs of integrals as well, also called the weak form. This is useful for the Finite Element Method Eq. 2.67. The dielectric tensor, ϵ, is assumed to be constant in this materials as they are homogeneous and isotropic so it can be taken as just a constant.

$$\nabla^2 \phi = -\frac{\rho(\mathbf{r})}{\varepsilon} \tag{3.3}$$

where $\rho(\mathbf{r}) = q \, (C - n + p)$ and n and p are functions of the position. Given some arbitrary weight function $w(\mathbf{r})$ and multiplying at both sides and integrating over all the volume

$$\int_V w(\mathbf{r}) \nabla^2 \phi \; \mathrm{d}V = -\int_V w(\mathbf{r}) \rho(\mathbf{r}) \mathrm{d}V. \tag{3.4}$$

Now, applying Green's Theorem [35] to the left hand side of the equation and the differential vector identity

$$w(\mathbf{r}) \nabla^2 \phi = \nabla \cdot (w(\mathbf{r}) \nabla \phi) - \nabla w(\mathbf{r}) \nabla \phi \tag{3.5}$$

the following expression is obtained

$$\int_{\partial V} (w(\mathbf{r}) \cdot \nabla \phi) \; \mathrm{d}S - \int_V (\nabla w(\mathbf{r})) \, (\nabla \phi) \; \mathrm{d}V = -\int_V w(\mathbf{r}) \rho(\mathbf{r}) \; \mathrm{d}V, \tag{3.6}$$

which is indeed an integral form of Eq. 3.1. Now, the solution ϕ is only required to be derivable up to the first derivative, $\phi \in C_1$, but so is the weight function, $w \in C_1$ as well.

Hence the name “weak” form as this is a weaker statement with respect to its differential form.

3.2.2 Continuity Equations

In the steady state solutions, the continuity equations on a semiconductor are

$$\nabla \cdot J_n = q\left(R_n - G_n\right), \tag{3.7a}$$

$$\nabla \cdot J_p = q\left(R_p - G_p\right). \tag{3.7b}$$

where $J_{n,p}$ are the density currents for electrons and holes, q the elemental charge, $G_{n,p}$ and $R_{n,p}$ the generation and recombination rates for electrons and holes respectively. Supplemented by the constitutive relations for the current, the following pair of equations is obtained

$$J_n = qn\mu_n\nabla\phi + qD_n\nabla n, \tag{3.8a}$$

$$J_p = qp\mu_p\nabla\phi - qD_p\nabla p, \tag{3.8b}$$

$\mu_{n,p}$ the electron and hole mobilities and $D_{n,p}$ the diffusion coeficient. Equations 3.7 and Eq. 3.8 along with the Poisson’s Equation, Eq. 3.1, form the so-called drift diffusion model for semiconductors.

3.2.3 Carrier Densities

In a semiconductor, one of the most important quantities is the carrier density n and p. From statistical mechanics and solid state physics, these equations can be derived.

$$n = N_C\, \mathcal{F}_{1/2}\left(\frac{E_f - E_c}{k_B T}\right) \tag{3.9a}$$

$$p = N_V\, \mathcal{F}_{1/2}\left(\frac{E_v - E_f}{k_B T}\right) \tag{3.9b}$$

where N_C and N_V are the corresponding effective density of states for the conduction and the valence bands. The $\mathcal{F}_{1/2}$ is the integral fermi function of $1/2$,

$$\mathcal{F}_{1/2}(x) = \int_0^\infty \frac{t^{1/2}}{1+\exp(t-x)}\mathrm{d}t. \tag{3.10}$$

The effective density of states for the conduction and valence bands are calculated from the expressions

$$N_c = 2\left(\frac{2\pi {m_e}^* k_B T}{h^2}\right)^{3/2} \tag{3.11a}$$

$$N_v = 2\left(\frac{2\pi {m_h}^* k_B T}{h^2}\right)^{3/2} \tag{3.11b}$$

where $m^*_{e,h}$ are the effective density of states masses for electrons and holes in the material, k_B the Boltzmann constant, T temperature and h the Planck constant.

3.2.4 Material Modelling

For the simulations run on these devices, three different kinds of materials were defined: semiconductors, conductors and insulators. Every one of these regions are treated different by the simulator. To simulate the different materials, a set of parameters were introduced that are characteristic of the materials. For semiconductors, the permittivity ϵ, the electron affinity χ, the bandgap E_g, the effective mass for electrons and holes m^* and the mobility for the two different carriers were defined. For conductors, the workfunction Φ and for insulators the permittivity, the electronic affinity band gap E_g were defined aswell. In the case of semiconductors, constant mobilities were chosen as the bias applied in the different simulations were small and all the simulations were carried out at room temperature (300K).

3.3 Device under Study

The FEM, in conjunction with the drift diffusion equations 3.1, 3.8 and 3.9 allow for the study of electronic devices of larger dimensions with respect to the small DFT devices or the description of MD[1]. This also is useful to calculate macroscopic quantities that only have meaning in a macroscopic level. On top of this, some devince features can also be calculated in a way that there is no need for an atomistic description of the system which would otherwise be very computationally expensive. First, a Field Effect Transistor (FET) based on a 2D MoS_2 channel is shown as part of the continuation on previous work. Then, a MoS_2 $p-n$ junction used to study the depletion length as a function of the doping.

---

[1] Parts of this section is a continuation on the Master's Thesis [43]. Many of the details missing here of that work can be found there.

3.3.1 2D MoS_2 channel FET

The FET geometry used for this work is based on from Ref. [81]. A scketch not to scale is shown in Fig. 3.1. The gate oxide is HfO_2, with ohmic gold contacts with a degenerate silicon separated by a SiO_2 insulator substrate that serves as a back gate and finally the MoS_2 channel. The output characteristics for this MoS_2 transistor are shown in Fig. 3.2. The set of parameters that characterize each material used are in table 3.1. Finally, with all these parameters, the output characteristics of the transistor are shown in Fig. 3.2. Comparing these results with the experimental results in Ref. [81] it can be observed that the saturation current obtained by the simulations is about 10 times the experimental data. This can be corrected by changing the electronic affinity of the MoS_2 channel. This way, while obtaining accurate agreement with the experimental results, some of these quantities can loose its physical meaning as these are not the experimental values anymore. On the other hand, the experimental value of the subthreshold swing is 74 mV dec^{-1}, while the obtained by the

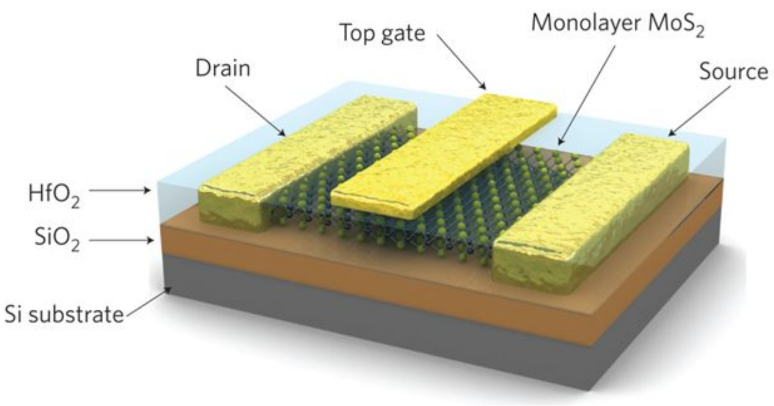

FIGURE 3.1: Single layer MoS_2 transistor geometry, not to scale. Reprinted with permission from Springer [81].

Parameter	MoS_2	Parameter	HfO_2	Parameter	Au
ε	$4\ \varepsilon_0$	ε	$25\ \varepsilon_0$	Φ	5.45 eV
χ	6.0 eV	χ	2.1 eV		
E_g	1.9 eV	E_g	5.7 eV		
m_e^*	$0.54\ m_e$				
m_h^*	$0.44\ m_e$				
μ_n	217 $cm^2 V^{-1} s^{-1}$				
μ_p	40 $cm^2 V^{-1} s^{-1}$				

TABLE 3.1: Modelling parameters for MoS_2, HfO_2 and Gold. Permitivitty ε, Electronic Affinity χ, Energy Band Gap E_g (300K), Effective mass for electrons and holes $m^*_{e,h}$ and mobility for electrones and holes $\mu_{e,h}$. For the contact, the workfunction Ψ.

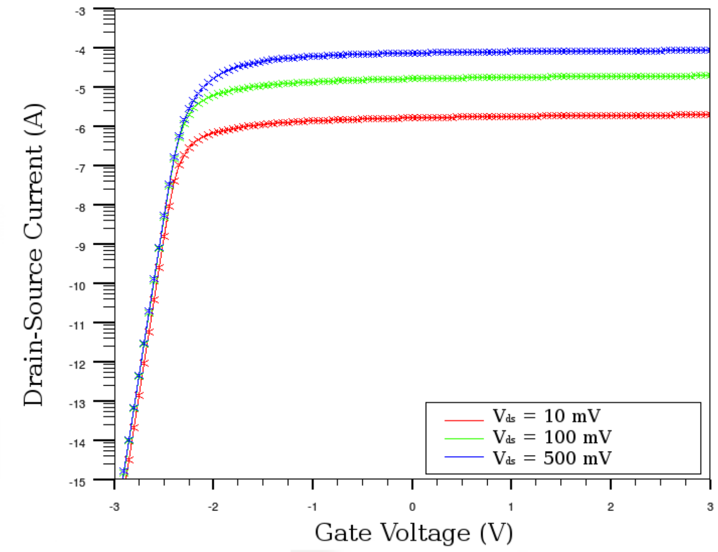

FIGURE 3.2: Simulated single-Layer MoS_2 FET output characteristics.

simulations is around 65 mV dec^{-1}. According to [89], the subthreshold swing is given by

$$S_s = \ln(10)\frac{k_B T}{q}\left(1 + \frac{C_q}{C_{ox}}\right). \tag{3.12}$$

With k_B is the Boltzmann constant, T the temperature, q the electron charge, C_q the capacity of the depletion layer capacitance and C_{ox} the capacity of the oxide. So in theory is it possible to tune the values of the capacitance of the oxide or the depletion layer, but would be by altering the geometry of the devince or adding artifical values of the materials in the simulation.

3.3.2 MoS_2 $p - n$ junction

The geometry used for this study is a simple metal-semiconductor-semiconductor-metal structure surrounded by vacuum as shown in Fig. 3.3. For this, different channel widths and different dopings for the MoS_2 were studied. The objective is to study the different depletion lenghts obtained using this model under a zero bias and under a small electric field. MoS_2 regions were modeled using the same parameters in table 3.1. The metal-semiconductor interface created a Schottky barrier, which was taken into account by the simulation. In one case, the interface was considered an Ohmic contact instead. Table 3.2 shows the results of the depletion lengths for different channel widths and different semiconductor doping levels. According to these results, in Fig. 3.4 the potential profile is shown for the 10μm $p - n$ junction.

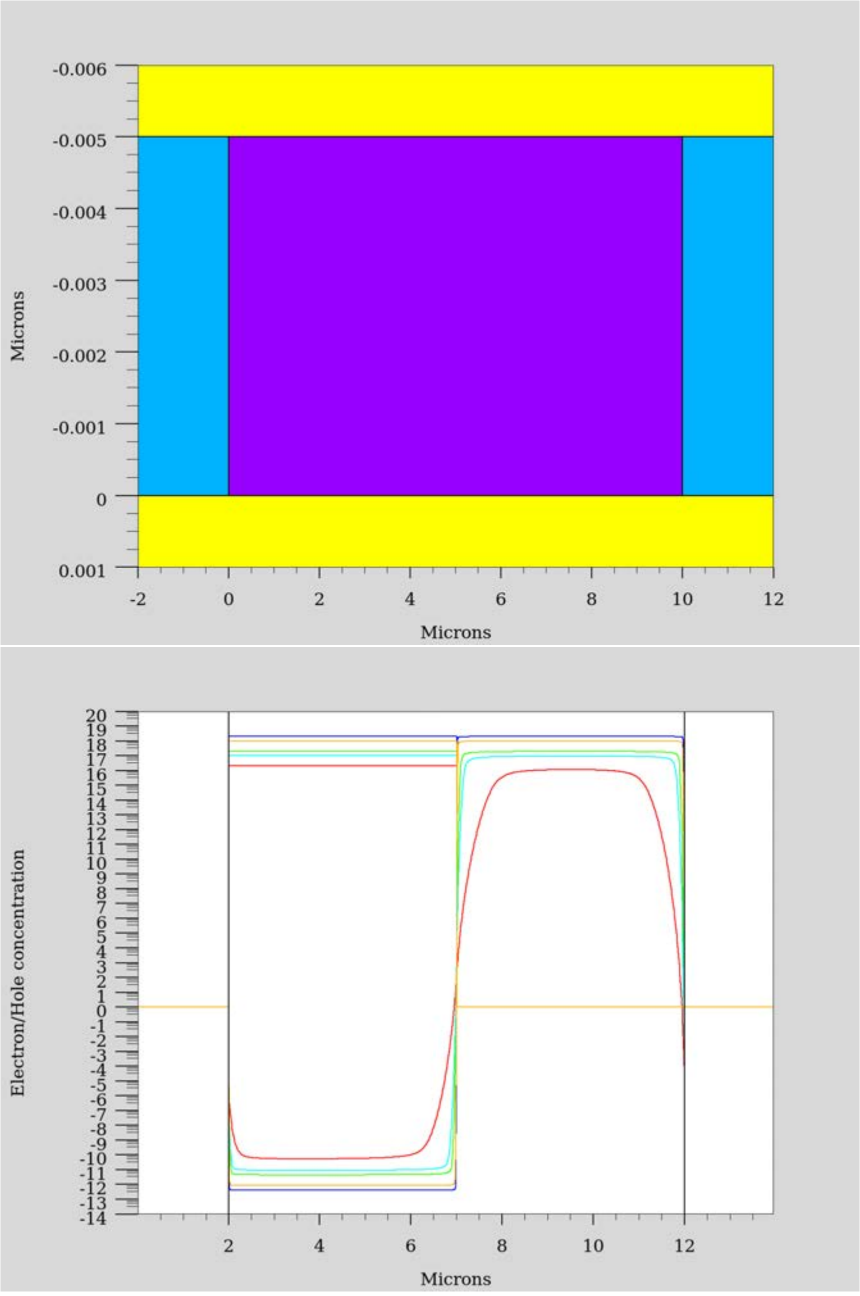

FIGURE 3.3: Top: Schematic MoS_2 $p - n$ junction of width 10 μm. Three different regions can be distinguished: Vacuum (Yellow), Metal contacts, gold (Blue) and MoS_2 (Purple). Bottom: MoS_2 junction electron and hole concentration. Five different concentrations were used: 1.0×10^{10} cm^{-2} (red), 5.0×10^{10} cm^{-2} (light blue), 1.0×10^{11} cm^{-2} (green), 5.0×10^{11} cm^{-2} (yellow), 1.0×10^{12} cm^{-2} (dark blue).

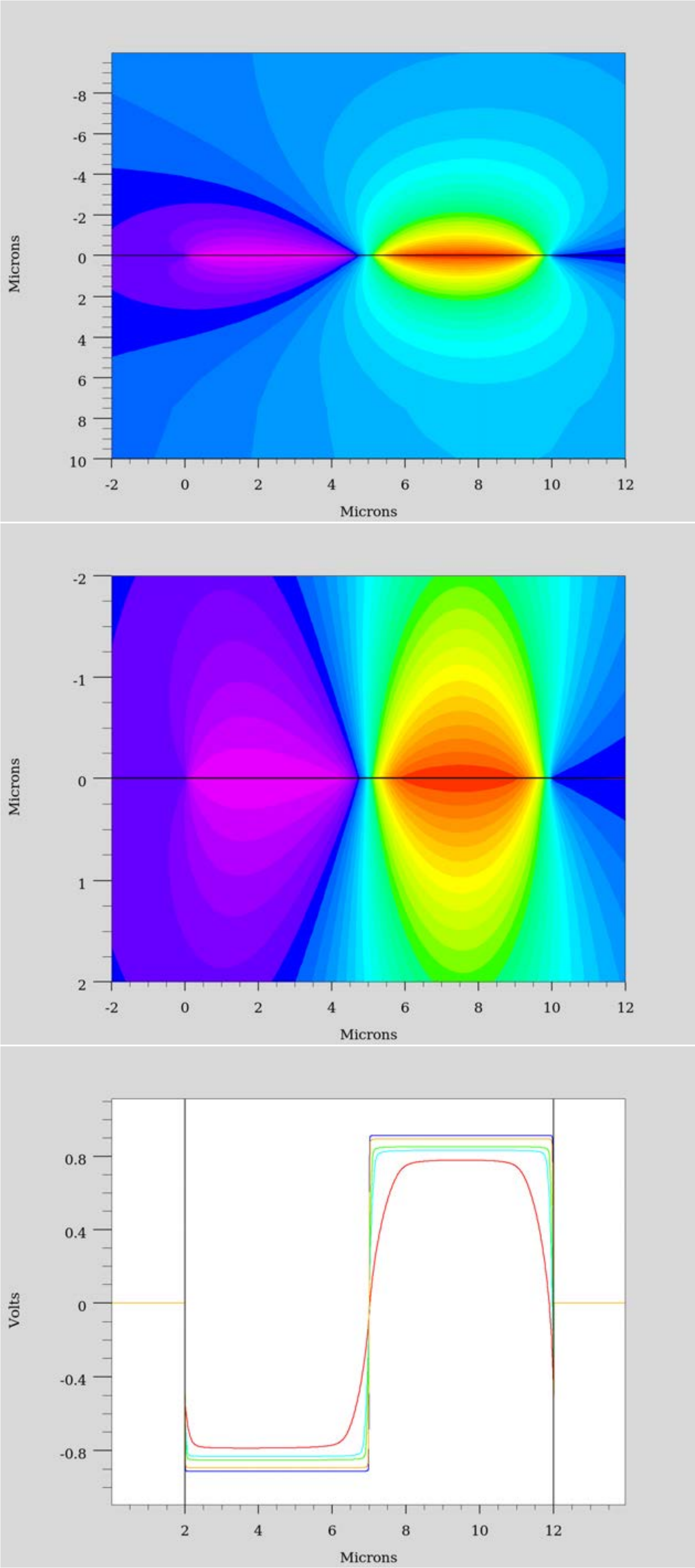

FIGURE 3.4: Potential contour of the MoS_2 $p-n$ junction of width 10μm at zero bias.

W \ x_p	1.0×10^{10}	5.0×10^{10}	1.0×10^{11}	5.0×10^{11}	1.0×10^{12}
0.1 μm					
1 μm			50 nm		
10 μm	400 nm	100 nm	50 nm	14 nm	9 nm
100 μm	600 nm				
10 μm*	600 nm				

TABLE 3.2: Depletion zone as a function of the Channel Width (W) at different doping levels (cm^{-2}) with Gold Shottky contacts. The blank spaces left represent flat depletion zone. *This corresponds to a simulation with Gold Ohmic contacts instead.

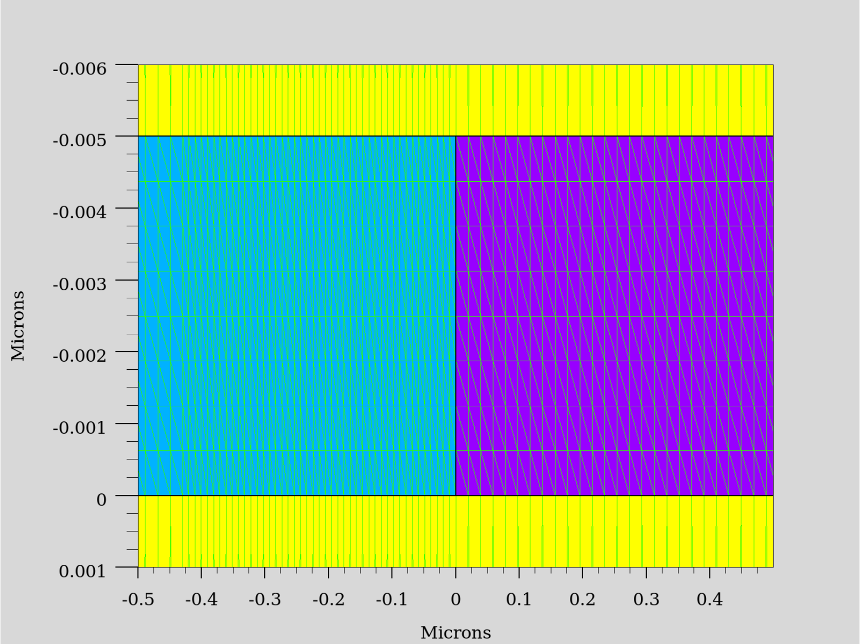

FIGURE 3.5: Detail of the metal-MoS$_2$ interface mesh. The green lines represent the division of each "element" of the graph that represents the mesh. Regions: Vacuum (Yellow), Metal contacts, gold (Blue) and MoS$_2$ (Purple)

The mesh is one of the key elements in order to obtain precise and reliable simulation results. The mesh is defined as a collection of points which the solution will be computed on until in converges. However, it is not a good idea to use a highly dense mesh for various reasons. First, there has to be a balance between accuracy and performance.

3.4 Conclusions

Two different devices were studied withing this model giving insight to the modelisation of electronic devinces using the drift diffusion equations with a finite element scheme. The single-layer MoS$_2$ FET was characterized using the FEM implemented in the SILVACO TCAD suite. This simulator assumed that all the regions in the device will behave like bulk material and all physical equations describing these regions are implemented like so. Plus, small size effects cannot be taken into account in order to simulate nanometric-sized systems properly.

However, the parameter set of these regions can be tweaked to reproduce at a qualitative level some of the output characteristics of the device. The output characteristics of this device is in accordance with the experimental data in a qualitative level. In order to adjust the output characteristics so that the simulated device reproduces more accurately the experimental data, few tweaks on the material properties must be changed. A $\mathrm{MoS_2}$ $p-n$ junction was also studied within this framework to calculate depletion lengths of this system. These results will help in the study of 2D materials with the drift diffusion model. Different widths with different dopings were considered obtaining the different depletion zones values.

Chapter 4

Bond Order Potential parametrisation for Pd-C and Ni-C interactions.

4.1 Introduction

The interaction between carbon based materials and some metals is very important since the rise of graphene as a new material. The electronic transport through structures based on these materials could help both understand its physics and figure out if such metals are suitabgle for high frequency devices along with graphene in different structures and geometries.

Albe *et al.* [1, 20, 66] parametrized elements metals of interest for many applications. These include Carbon, Platinum, Gallium, Nitrogen and Silicon. This was developed after the potential that Tersoff [92] proposed in 1986 and with the later modifications of Brenner [10], it is a formalism that is widely used nowadays and it is shown in this chapter.

The objective of this project is to work in this framework with relevant materials for radiofrequency applications and that have not been yet parametrized. In this project the parametrization for Nickel and Palladium was studied. The interest on these materials is such that it will allow to construct different structures and use molecular dynamics to perform both a CVD-like deposition or structural relaxation of transport structures as a first step for DFT calculations. Building realistic structres could give a more accurate description of contact resistance for top-contact like geometries, similar to the ones studied in chapter 5. In turn, this parametrisation will be useful for geometry relaxation of the structures containing these elements for further study afterwards with other methods, In particular Nickel and Palladium were studied in detail to obtain a parametrization of these materials for a handful of reasons. For nickel it is known that it has a (111) lattice parameter very similar to graphene and it is very interesting to use it in conjunction with. On the other hand, Palladium is a material proven to be very useful in high frequency applications [37, 105].

4.1.1 The Bond Order Potential

First proposed by Tersoff [92], this empirical interatomic potential was the first of the kind to take into account more terms in an energy expansion such that three body interactions were possible, leading to the prediction of closed packaged structures [91]. Later, Brenner [10] refined this potential for the study of chemical reactions in hydrocarbons. Afterwards, Albe *et. al.* [1, 20] used this same approach with the help of the Tight Binding potential for transition metals of Cleri and Rosato [15]. With this last tuning it allowed to study of mixed systems with carbon and *d*-transition metals.

From Ref. [1] the total energy is calculated using the following expression

$$E = \sum_{i>j} f_{ij}(r_{ij}) \left[V_R^{ij}(r_{ij}) - \frac{b_{ij} + b_{ji}}{2} V_A^{ij}(r_{ij}) \right], \tag{4.1}$$

where V_R and V_A are the repulsive and attractive potentials. The approximation used includes only nearest neighbours and in order to be computationally efficient a cutoff function is required. The cutoff function, $f(r)$, takes the following form

$$f(r) = \begin{cases} 1, & r \leq R - D, \\ \frac{1}{2} - \frac{1}{2}\sin\{\pi(r-R)/2D\}, & |R-r| \leq D, \\ 0, & r \geq R + D \end{cases} \tag{4.2}$$

Where r is the distance of two atoms labelled i, j and R and D are parameters to be determined later. The b_{ij} coefficients are the bond order coefficients which include angular dependency to reproduce correctly the formation of bonds. Following the Albe *et al* paper, this term takes the following form

$$b_{ij} = (1 + \chi_{ij})^{-1/2}$$

$$\chi_{ij} = \sum_{k(\neq i,j)} f_{ik}(r_{ik})\, g_{ik}(\theta_{ijk})\, \exp\left[2\mu_{ik}(r_{ij} - r_{ik})\right]$$

where the cutoff function is included again. Finally, the angluar dependancy is

$$g(\theta) = \gamma \left(1 + \frac{c^2}{d^2} - \frac{c^2}{[d^2 + (1+\cos\theta)^2]}\right). \tag{4.3}$$

For $c = 0$ this term is equal to a constant, γ, and the potential takes the form of the Embeded Atom Method potential [20]. This angular dependancy is decisive for covalent systems and for modeling metals aswell. Finally the analytical form of the attraction and repulsion potentials in Eq. 4.1 take the form of fully equivalent Morse-like structures

$$\begin{aligned} V_R(r) &= \frac{D_0}{S-1} \exp\left[-\beta\sqrt{2S}\ (r - r_0)\right], \\ V_A(r) &= \frac{S\,D_0}{S-1} \exp\left[-\beta\sqrt{2/S}\ (r - r_0)\right], \end{aligned} \tag{4.4}$$

with D_0 the dimer binding energy and r_0 the equilibrium distance. If the binding energy D_0 and the ground state frequency of the dimer molecule are known, then β is obtained from the expression

$$\beta = k\frac{2\,\pi\,c}{\sqrt{2D_0/\mu}}, \tag{4.5}$$

where k is the wave number and μ the reduced mass. The parameter S can be determined by the Pauling criterion that relates the bonding distance r_b and the bond energy

$$E_b = -D_0 \exp\left[-\beta\sqrt{2\,S}(r_b - r_0)\right]. \tag{4.6}$$

This last equation must be fullfilled when fitting lattice parameters and cohesive energies. This is extremely decisive for the transferability of the potential.

To summarize this section, the set of parameters that describe the physics of the simulated systems is

$$\{S, \beta, D_0, r_0, R, D, \gamma, c, d, \mu\}. \tag{4.7}$$

4.2 Parameter Optimisation

To obtain all ten parameters from the BOP potential an optimisation of the parameters have to be carried out from the DFT total energy calculations. For this, a geometric relaxation have to be done with DFT to obtain both final geometry and total energy. With this, the Parallel Tempering Monte Carlo algorithm is able to find a set of parameters that describes both the geometry and the energy with a certain degree of accuracy.

The basic idea of the PTMC algorithm is to run several Monte-Carlo simulations at different temperatures for different sets of parameters at each temperature. This allows the exchange of parameters between different temperatures, to thorougly explore the configuration space of the parameters at higher temperatures, while finding the local minima at the lower temperatures. Represented in Fig. 4.1 the basic principle of the algorithm is shown. This method is demonstrated to be useful when the dimensionality of the parameter space is large and has been used before in Refs. [25, 26] to solve a very similar problem.

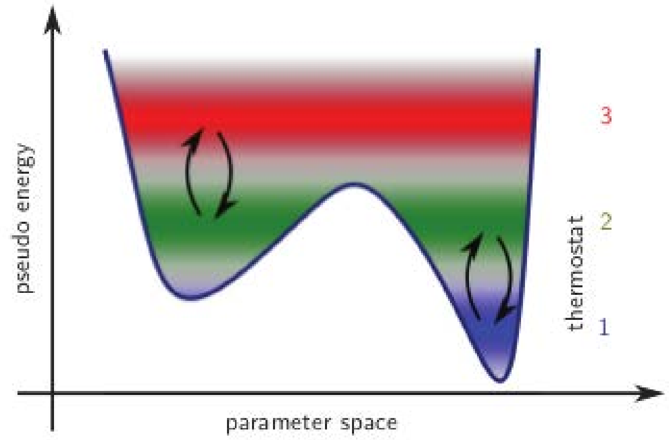

FIGURE 4.1: Principle of PTMC. Markov chains at high temperatures allow to explore broad regions of configuration space and help the chains at lower temperatures to escape local minima though successive swapping moves, resulting in a much faster equilibration. In the context of global optimization, the low temperature replicas can also discover previously unexplored regions much more efficiently. Source [26].

In order to use the PTMC algorithm, several test configurations with their respective energies must be known beforehand. Several configurations had to be relaxed using DFT to obtain the total energy of the system, according the respective functional used, and the relaxed geometry. The simplest but most significant system that was studied are a series of nanoparticles of increasing size in number of atoms and bonds with the substrate. In particular we were interested in studying the bonding of Nickel and Palladium on a graphene substrate described in the next section.

4.2.1 Geometry Description

In order to use the parametrisation method described in the previous section, some training input data had to be provided. This data came from DFT calculations, in particular metal nanoparticles on top a graphene layer were chosen. In Fig. 4.2 one of the nanoparticles is shown. Several sizes and several positions on top of the different sites on graphene were tested to find the optimal place for metal atoms in the substrate to rest at minimum energy. The complete set of geometries used for the PTMC algorithm training range from a single atom on top of the graphene lattice in a hollow, bridge or top position, up to a 55 atom nanoparticle. From 1, 2, 3, 4 and 7 metal atoms on top of graphene consist on planar structures layed on the most stable positions, see Fig. 4.3. Then, a geometry composed by 13 atoms in three different internal configurations represented in Fig. 4.4. The number of Carbon-Metal bonds differs. The configuration a and b have 3 while configuration c has 4. The 38 atom nanoparticle is shown in Fig. 4.5 with two internal different structures, represented by a mirror symmetry. Finally, a 55 atom ball represented in Fig. 4.6. In Appendix A the rest of the Nickel-Graphene geometries are shown in a similar fashon for completeness.

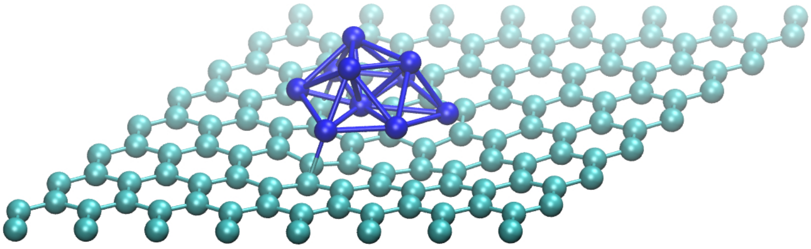

FIGURE 4.2: Example of a small nanoparticle of 10 Ni atoms over a graphene sheet.

4.2.2 Computational Details

All the geometries were relaxed until all constrained forces were lower than 0.01 eV/Å using the GGA functional in the parametriation of Perdew, Burke and Ernzerhof [77] for Nickel. For Palladium, the LDA functional [12] was used instead as it gives a better description of the Pd-C bond distance [95, 103]. The core electrons were treated using norm-conserving pseudopotentials of the Troullier-Martins type [94] with a double-ζ plus polarization base taking into account spin polarization for Nickel. All this calculations used a 2×2×1 Monkhorst-Pack Grid [64] using the SIESTA package [87].

4.2.3 Force field Parameters

After the optimisation of parameters through the PTMC algorithm, a set of parameters was found for both Ni-C and Pd-C, summarized in table 4.1. This set of rules describe only the Carbon-Metal interaction. To describe the Carbon-Carbon pair the description in Brenner [9] is used and the parametrisation within. For the Metal-Metal interaction the Embeded Atom Potential is used as described in Ref. [16]. For completion, added in Appendix B the required LAMMPS potential file as well as a code snipped for how to include them in any LAMMPS

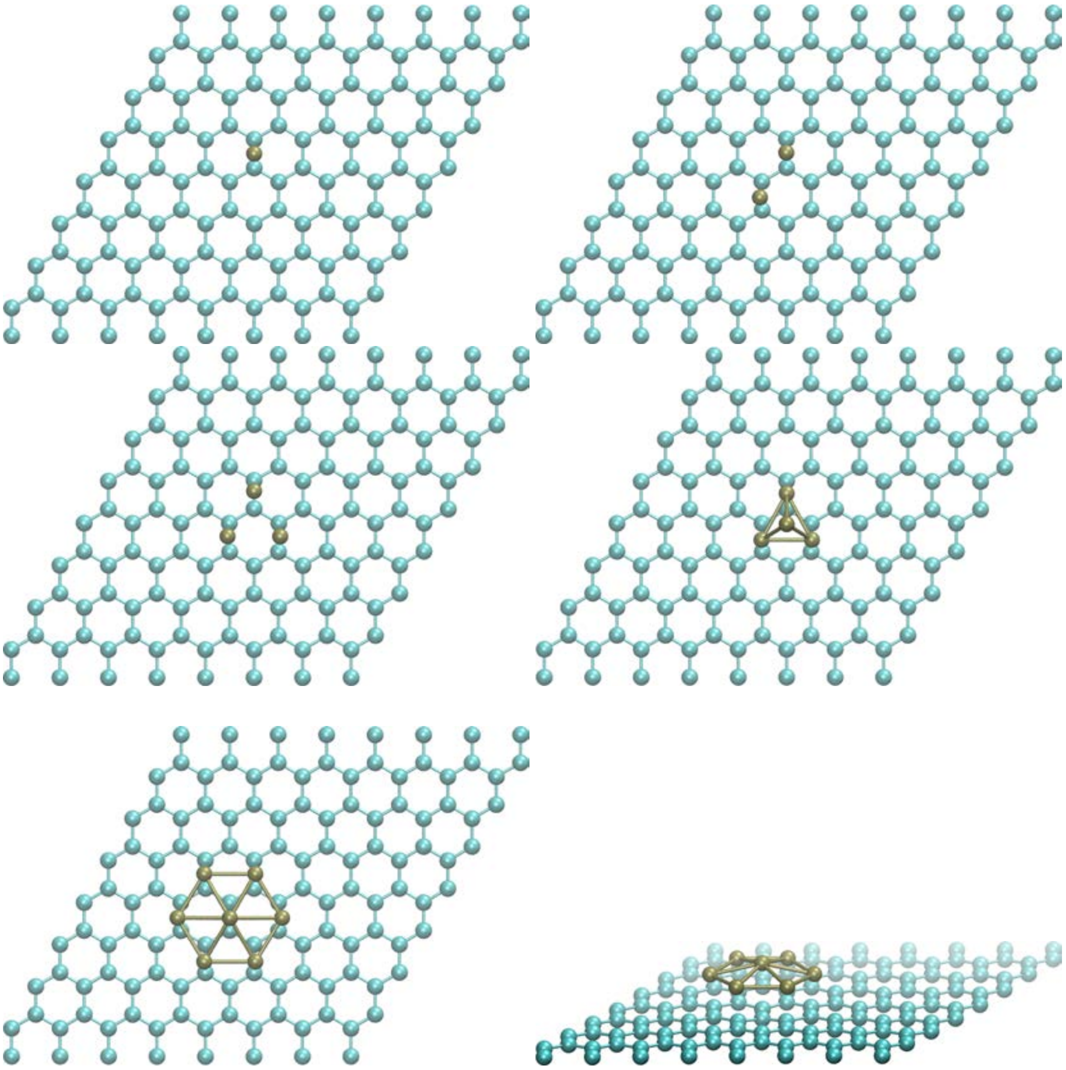

FIGURE 4.3: 1, 2, 3, 4 and 7 (top and lateral view) Pd atoms on top of a graphene sheet after geometry relaxation.

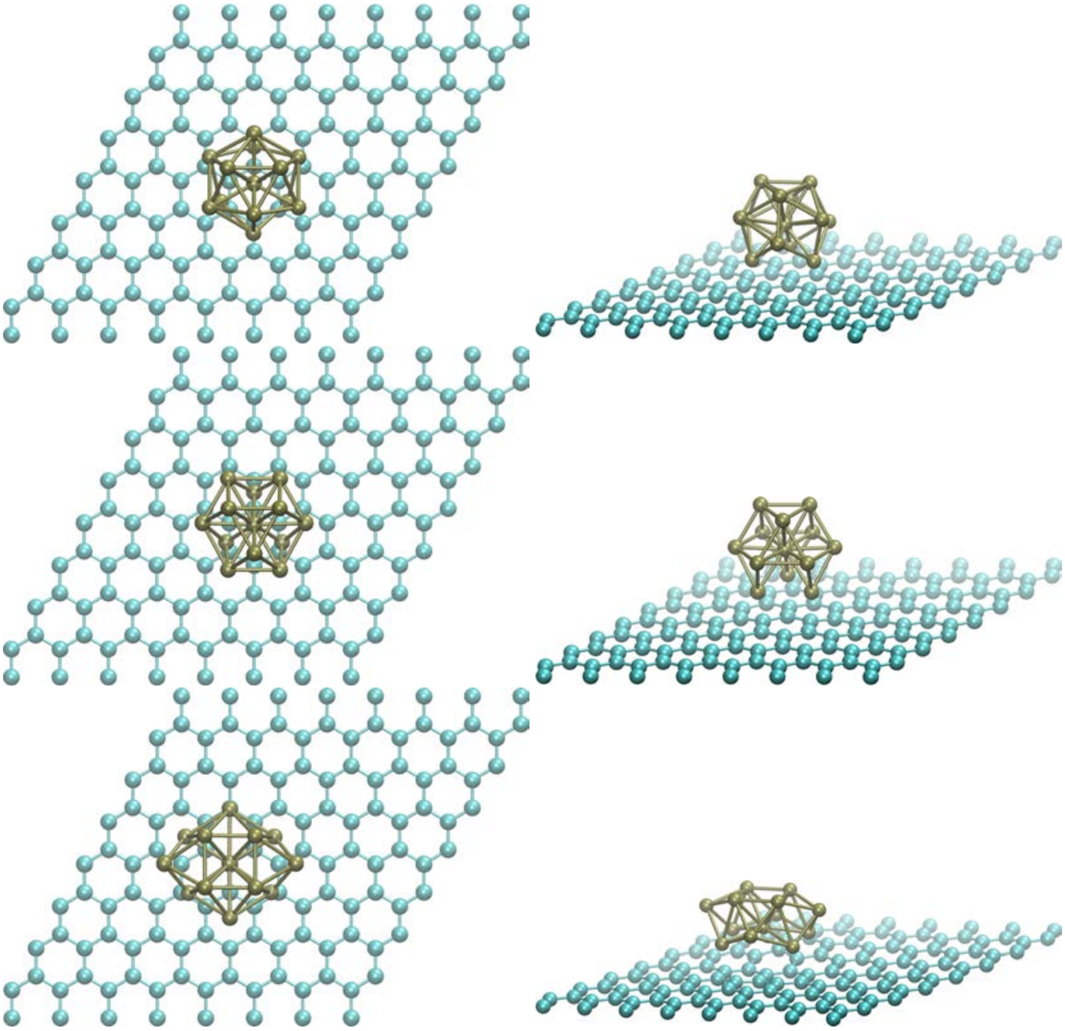

FIGURE 4.4: Top and lateral view for 13 Pd atoms on top of a graphene sheet with three different configurations.

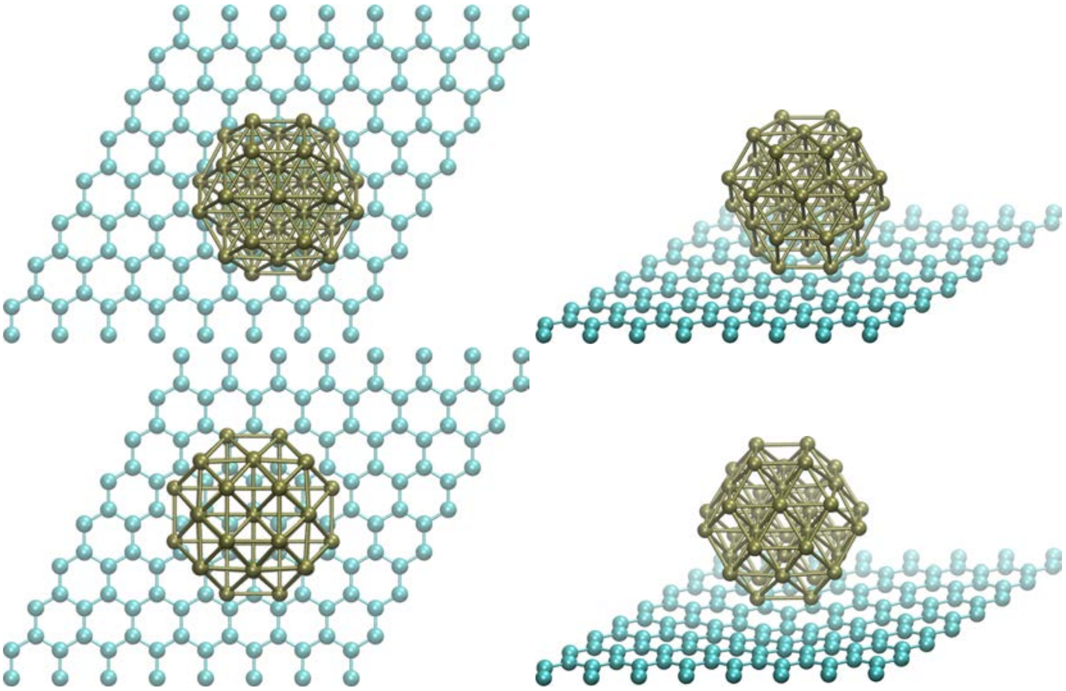

FIGURE 4.5: Top and lateral view for Pd 38 a and b configurations on top of a graphene sheet. The two configurations are a mirror image of each other.

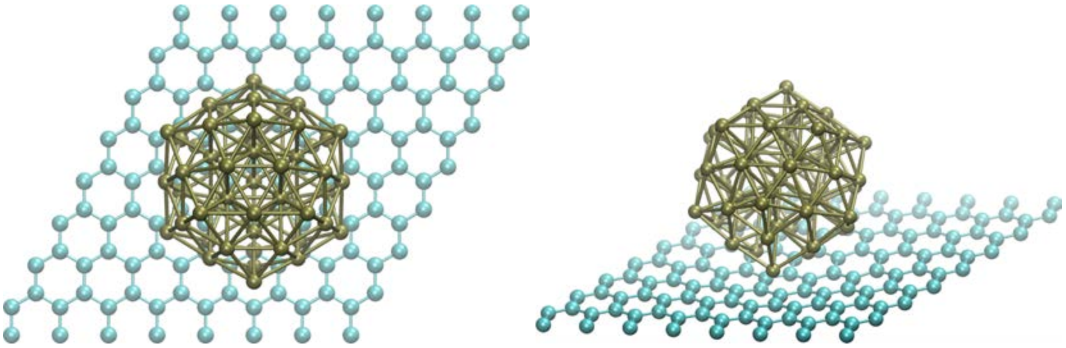

FIGURE 4.6: Top and lateral view for Pd nanoparticle consisting of 55 Pd atoms arranged in a quasisphere.

calculation. In these files the Pd-Pd, Ni-Ni and C-C interactions are also included as described above. For each geometry, the PTMC algorithm reached an energy reproduction according to the parameters used. In table 4.2 the values for the obtained DFT adsorption energies and the reproduced energies with the PTMC algorithm for each set of parameters is shown side by side. These results look very promising as the reproduced energies are very close to the target energies but more testing has to be done before using this force field's parameters for any production simulation. For example, the dimer energy, equilibrium distance, or the bond distance are all measures of how good of a parameter set this is with the possiblity of iterating the parameters again with a new initial guess.

	Pd-C	Ni-C
S	1.433×10^{2}	1.432×10^{2}
β	4.300	4.296
D_0	1.758	1.758
r_0	6.802×10^{-2}	6.807×10^{-2}
R	5.141	5.150
D	9.89×10^{-3}	5.0×10^{-2}
γ	1.806×10^{-2}	1.800×10^{-2}
c	6.903×10^{2}	6.888×10^{2}
d	4.755	4.753
μ	2.803	2.807

TABLE 4.1: Bond Order Potential parameters obtained from the PTMC optimisation through *ab initio* training for the Pd-C and Ni-C pairs. The C-C and Me-Me parameters are added in Appendix B.

N$_a$	E_{target}(Pd)	$E_{\text{reproduced}}$(Pd)	E_{target}(Ni)	$E_{\text{reproduced}}$(Ni)
1	-4.39458	-4.02778	-3.88876	-3.93083
2	-5.40951	-5.29990	-4.25306	-5.50767
3	-6.47832	-6.14807	-5.20541	-6.64512
4	-6.03174	-6.36230	-5.68362	-6.94597
7	-10.52663	-9.34759	-7.44564	-9.06748
10	-9.44840	-9.75142	-7.95338	-9.00257
13a	-6.71057	-9.31021	-5.45038	-7.10955
13b	-6.52372	-5.86262	-7.25059	-8.69627
13c	-8.73059	-9.15725	-7.99246	-9.33724
38a	-9.14434	-9.24890	-7.44934	-7.39335
38b	-6.49479	-6.99212	-5.14229	-6.47318
55	-9.56981	-10.86422	-7.20522	-8.06162

TABLE 4.2: Adsorption and reproduced energies (in eV) for different configurations of metallic nanoparticles on a graphene sheet for both Palladium (Pd) and Nickel (Ni). The letters by some of the structures indicate different internal configurations, see Appendix A.

4.3 Conclusions

Of course, this parameter set needs more testing before it can be released and needs to be validated agains experimental data and theoretical calulation from first principles. This said, a realistic structure of metal deposited on a graphene sheet can be carried out and its results studied. This simulations can be then used in combination with tight-binding codes to calculate ballistic transport properties in the context of high frequency applications.

To conclude, the bond order potential in the interpretation of Albe *et. al.* is the most suitable force field to describe the Metal-Carbon interaction and a set of parameters was found for the interactions Pd-C and Ni-C. The parametrisation of Pd-C and Ni-C interactions were studied for the suitability of metallic contacts with graphene using the PTMC algorithm for parameter optimisation. This algorithm is a very efficient tool for optimisation tasks that allows for a thorough search of the configuration space while able to find optimal values on a certain region of this space. With this parameter set, it will be possible to simulate CVD-like deposition of a metal on graphene, or use molecular dynamics for a first relaxation of large systems which would not be suitable using first principles techniques.

Chapter 5

Graphite Graphene Contacts

5.1 Introduction

Throughout the last fifteen years, graphene has demonstrated its capabilities as a new material with its extraordinary properties [31]. Although the lack of bandgap forbids the use of this material for digital applications, its properties are very well suited for analog radiofrequency devices [23]. However, before graphene can be widely adopted, several difficulties must be overcome. In particular, one of the limitations for the use of graphene in analog electronics is the high contact resistance when metal-graphene contacts are fabricated, while an upper bound of $100\ \Omega \cdot \mu\text{m}$ would be desirable [23, 96].

Theoretical work has been carried out for contact resistance between graphene and other metals. For instance, Chaves *et al* [14] created a model for contact resistance between metal and graphene in a top contact-like geometry. The metal-graphene edge contact geometry, in spite of its vanishing contact overlap, has also been proven to be at least as good as some of the top contact geometries [99]. Also, metal-carbon nanotube contacts have been long studied, both experimentally and theoretically, with extensive reviews in Refs. [88, 56].

Since graphene is a semimetal, interface dipoles will quickly be screened out, and thus no Schottky barriers are expected—or, more precisely, they are thin enough that carriers may easily tunnel through—. So, of the three injection mechanisms discussed in Ref. [2], only field emission should be applicable to lateral injection into graphene. Phase engineering [44, 98, 72] is a promising approach to achieve high-quality lateral contacts to semiconductors, but in principle not applicable to graphene. In top contacts, charge is injected through an interface with a lower degree of covalency than in edge contacts [86]. A possible strategy to lower contact resistance is the addition of an interface layer [36]. Other strategies have been reviewed in Ref. [19].

Despite their obvious similar structural properties, the use of graphite as an electrode for contacting graphene has received much less attention. The Lieber group has synthesized monolithic graphene-graphite structures, obtaining specific contact resistivities in the range of 700-900 $\Omega \cdot \mu$m, better than similarly fabricated Cr/Au junctions [75]. Also, Chari *et al* measured the resistivity of rotated graphite-graphene contacts, obtaining specific contact resistivities as low as 133 $\Omega \cdot \mu$m for holes and 200 $\Omega \cdot \mu$m for electrons [13].

The objective of this paper is to demonstrate the viability of graphite-graphene contacts and show their fundamental limits. To this purpose, we describe in section 5.2.1 the used geometry, followed by the computational methodology in section 5.2.2. We show in section 5.3 that this yields results well below the upper contact resistance limit for certain values of the overlap area and doping level. Then, an eigenchannel analysis give us more insight about the scattering processes in the interface between the graphite substrate and the graphene. This analysis brings us to the conclusions, in section 5.4, that the graphite-graphene interface presents more of an area effect than metal-graphene contacts [106], but still with very small transfer lengths of $\sim$20 Å.

5.2 Methodology

5.2.1 Geometry Description

Top contact geometries will be the focus because they are the most easily fabricated [2]. In Figure 5.1, a ball-and-stick representation of the structure of the graphite-graphene contact is displayed. As usual in ballistic transport calculations, there are three differentiated zones: a left electrode—where the electrons are injected—, a scattering zone through which electrons will pass or reflect, and a right electrode into which electrons that were not backscattered will arrive. The electrodes are semi-infinite and a single graphite-graphene contact will be studied.

In this chapter, the effect of overlap length of graphene over the graphite bulk has been studied. The numbers in the scattering zone indicate the different number of overlapping C-pairs providing the contact between graphene and the graphite substrate. We also studied the case where the last graphite layer turns into the graphene sheet, which we interpret as an edge graphite-graphene contact [99]. We have always considered perfectly aligned graphite-graphene junctions, as the study of the rotated contacts fabricated in Ref. [13] would result in computational cells too large to begin treated with first-principles methods.

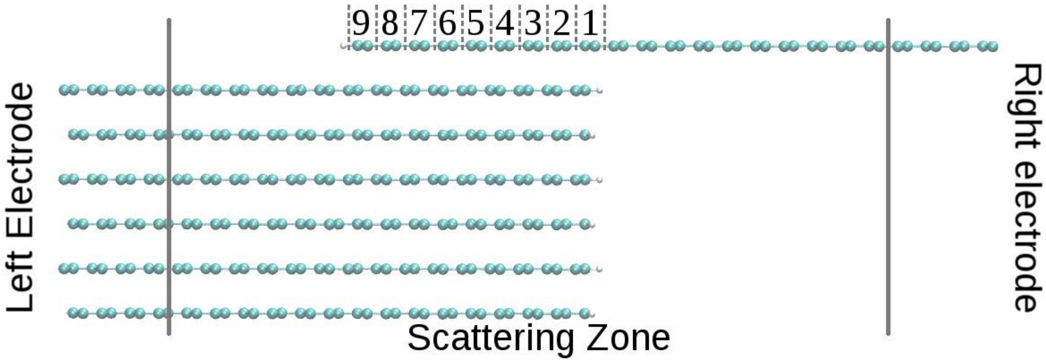

FIGURE 5.1: Ball-and-stick structure for the Graphite-Graphene top contact. Green/dark gray (white/light gray) balls indicate the carbon (hydrogen) atoms. Also indicated are the three different regions: Left Electrode, Scattering Zone and Right Electrode used for transport calculations. Electrons are injected in the left electrode through the scattering zone into the right electrode.

Structures were relaxed from first-principles using the SIESTA code [87], an efficient implementation of the Density Functional Theory using localized pseudo-atomic orbitals. Transport calculations were carried out using TRANSIESTA [8, 74], which implements the Non-Equilibrium Green's Function formalism under the DFT as well.

5.2.2 Computational Details

Calculations were performed with a double-ζ polarized basis set, using norm-conserving pseudopotentials of the Troullier-Martins type [94]. The lateral periodicity of the structure was accounted for using a 16 $k_{\|}$-point Monkhorst-Pack [64] grid for structural relaxations, and a dense 3056 $k_{\|}$-point grid in order to properly capture the fine details close to the Dirac point. Numerical integrals were carried out on a discretization mesh equivalent to a cut-off of 250 Ry, which provides total energies for graphene and graphite converged to the few meV range. The Generalized Gradient Approximation (GGA) in the parametrization of Perdew-Burke-Ernzerhof (PBE) [77] was used to describe exchange-correlation effects. GGA accurately describes the lattice parameter of graphene, but underestimates the interlayer distance [84]. This, of course, can be corrected with the use of van der Waals (vdW) type functionals. It has been demonstrated that the parametrization of Dion-Rydberg-Schröder-Langreth-Lundqvist (DRSLL) of the vdW interaction provides a good description of the interlayer distance while slightly overestimating the in-plane lattice constant [84, 18]. Thus,all structural and cell relaxations for graphene and graphite were carried out with the vdW-DRSLL functional until residual stress tensor components were below 1 kbar (forces were very close to zero because of the structural symmetry), obtaining an interplane distance of

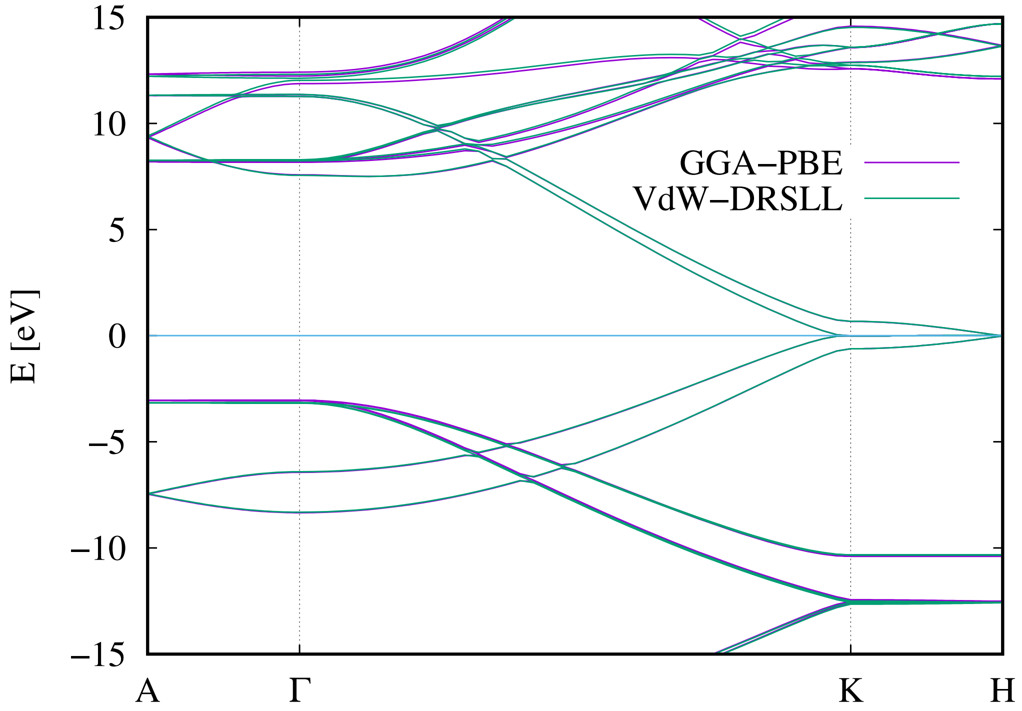

FIGURE 5.2: Energy bands for graphite. Purple (green) lines are obtained with GGA-PBE (vdW-DRSLL) parametrization, and the structure is taken to be the same for both functionals. The clear blue line indicates the Fermi Level position.

3.377 Å for graphite, in good agreement with experimental values. On the other hand, the interlayer binding energy we obtain with the vdW-DRSLL functional is 199 meV/atom, quite higher than experimental values [108] or even values obtained with plane waves with the same functional [84]. Due to SIESTA's use of localized orbitals, binding energies [29] have a tendency of being higher values than otherwise obtained. Unfortunately, since difficulties were found to achieve electronic convergence with the vdW-DRSLL functional for the transport structures (cf. Figure 5.1), the PBE functional was used to relax the in-plane positions until in-plane forces were below 0.04 eV/Å, while keeping the interplane distance to the vdW-DRSLL value.The PBE functional was used for transport calculations as well. From the transport point of view, this is justified because, for a fixed geometry, the two functionals yield very similar energy dispersions. In Fig. 5.2 the energy bands comparing the two functionals for bulk graphite with the relaxed geometry are shown. Around the Fermi level, the energy difference between the two curves is negligible, and therefore it is concluded that both functionals provide a good description of the energy dispersion of the system. In particular, it must be stressed that the dispersion along z, which is closely related to the interlayer coupling (*i.e.* transport) of the electronic states, is not affected by the passage from the vdW-DRSLL functional to PBE.

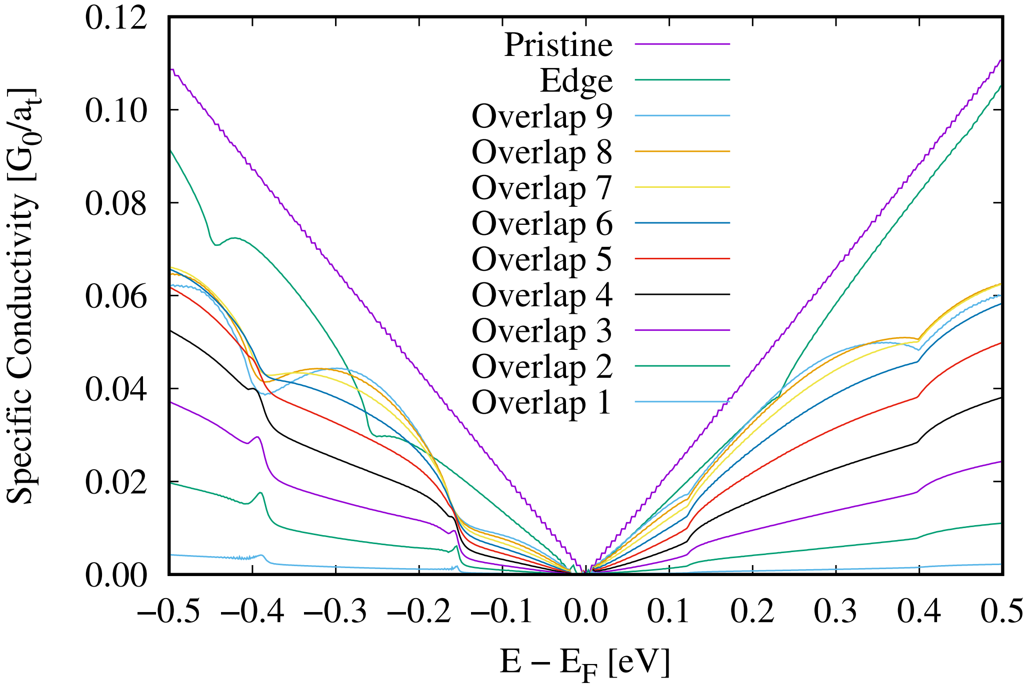

FIGURE 5.3: Specific Conductance of the Graphite-Graphene contacts per unit of lattice length.

5.3 Results

From the TRANSIESTA calculations we obtain the energy-resolved specific conductance (*i.e.* the conductance per unit of tranverse length) for the different structures.

In Figure 5.3 the specific conductance, in units of $G_0 = e^2/h$ over the transverse length of the calculation cell ($a_t = 2.484$ Å), is shown for the graphite-graphene top contact for different values of the overlap (cf. Figure 5.1) and the edge contact. The pristine graphene case— which provides the quantum limit for the conductance of the whole structure— is shown as well for reference. We note that the difference between the edge contact and the pristine graphene limit is small, suggesting that an edge, or large overlap, contact between graphite and graphene would provide a low contact resistance. Regarding the varying amount of overlap, we observe that, contrary to the metal-graphene case [106], there is a noticeable monotonic dependence of the conductance on the overlap width. This is a reflection of the weaker substrate-graphene $p_z - p_z$ coupling compared to the stronger $d - p_z$ coupling in metal substrates. Despite the weaker coupling, a relatively narrow overlap of ~ 20 Å suffices to achieve a conductance similar to metallic substrates for doped graphene (see Ref. [106]). We now turn our attention to the (specific) contact resistance. It can be extracted from the calculated conductance of the whole graphite-graphene structure, $G_{gg}(E_F)$, where E_F is the Fermi level, and the calculated conductance of the pristine graphene layer, $G_g(E_F)$. The

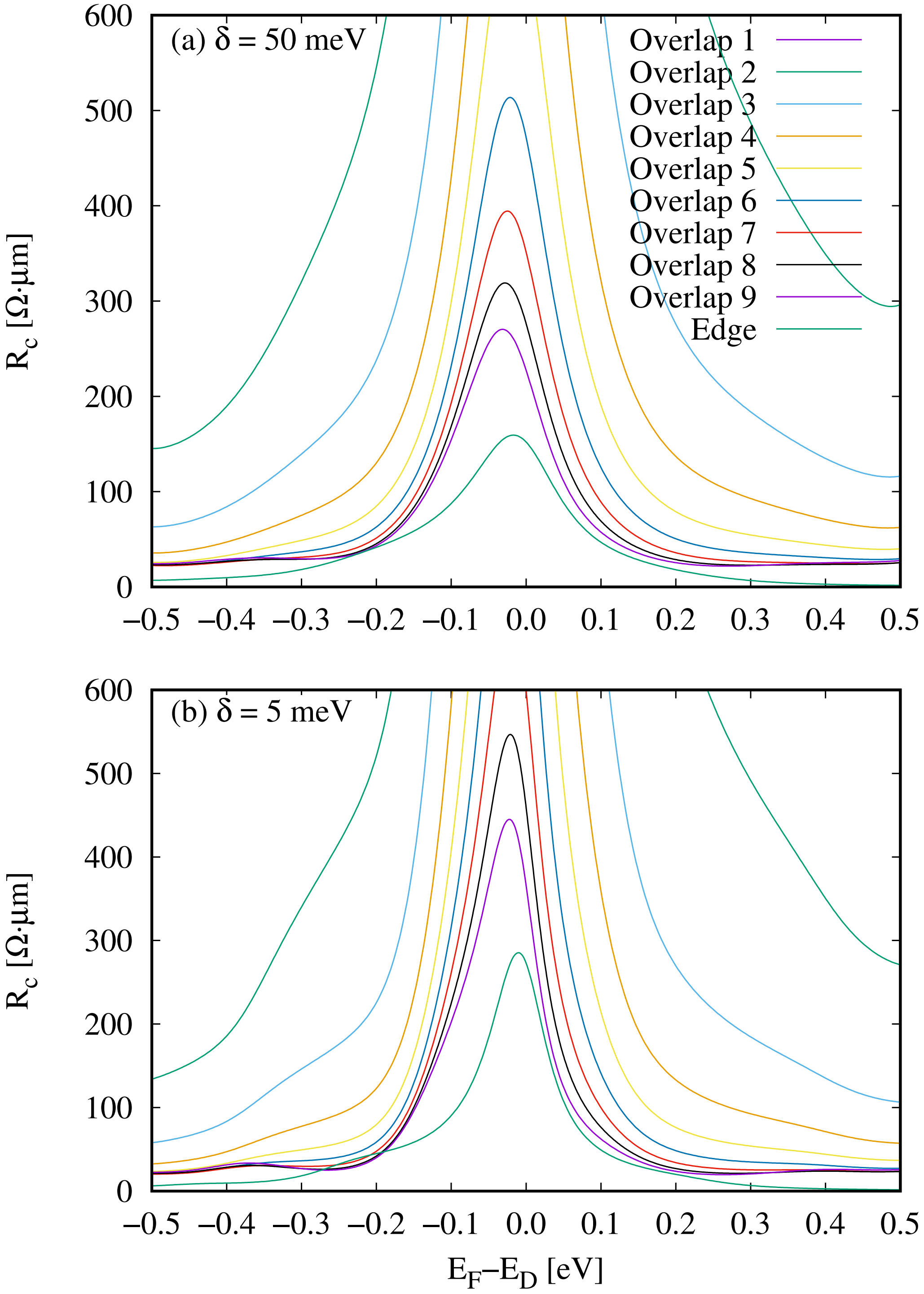

FIGURE 5.4: Specific Contact Resistance. (a) Thermal broadening at 300 K plus electron-hole puddle of 50 meV. (b) Thermal broadening at 300 K plus electron-hole puddle at 5 meV.

contact resistance R_c is then given by the following operation on the conductances:

$$R_c(E_F) = G_{gg}^{-1}(E_F) - G_g^{-1}(E_F). \tag{5.1}$$

Now, in order to calculate the zero bias contact resistance considering a thermal and gaussian electron-hole (e-h) puddle [42] broadening, we used:

$$
\begin{aligned}
R_c(E_F) = \\
&+ k_B T \left(\iint \frac{\exp\left[(E-E')/k_B T\right]}{1+\exp\left[(E-E')/k_B T\right]^2} \, G_{gg}(E) \, w(E'-E_F;\eta) \, \mathrm{d}E \, \mathrm{d}E' \right)^{-1} \\
&- k_B T \left(\iint \frac{\exp\left[(E-E')/k_B T\right]}{1+\exp\left[(E-E')/k_B T\right]^2} \, G_{g} \, (E) \, w(E'-E_F;\eta) \, \mathrm{d}E \, \mathrm{d}E' \right)^{-1} ,
\end{aligned}
$$

where $w(E'-E_F;\eta)$ is the gaussian broadening function and η the broadening paremeter, taken to be 50 meV for SiO$_2$ substrates [42], T is the chosen temperature and k_B is the Boltzmann constant.

The obtained specific contact resistance results are shown in Figure 5.4. The contact resistance at the Dirac point (undoped graphene) strongly depends on the amount of overlap, with the widest overlaps getting close to the $100\ \Omega \cdot \mu$m value, especially in the case of high e-h puddle broadening. The values of the contact resistance at higher/lower values of the Fermi energy (*i.e.* doped samples) rapidly decrease below the landmark value of $100\ \Omega \cdot \mu$m. These values are represented, for carrier concentrations calculated according to the procedure in Ref. [21], as a function of the graphene-graphite overlap, L_c, in Figure 5.5, where we see that the R_c values effectively saturate for $L_c > \sim 20$ Å in highly doped samples, while L_c might extend for a few 10s of Å more when contacting lowly doped graphene. To calculate the conductance and contact resistance for doped samples it was assumed that the electrostatics of the interface remain constant for different values of the doping. To asses this assumption, the Density of States were calculated for pristine graphene and for a graphene sheet charged uniformly such that $E_F - E_D = 0.2$ eV. Represented in Fig. 5.6, the DOS for a charged sheet of graphene does not change substantially, it shifts to the left for about 0.2 eV. The total charge added in a 2 atom primitive cell is ~ -2.52mC.

5.3.1 Current path analysis

In order to asses our conclusions and gain insight into the graphite-graphene coupling, an eigenchannel analysis has been carried out using the Inelastica package [27, 76]. In Figure 5.7, current is represented by arrows for each atom in the geometry, represented by translucid balls, and with the arrow thickness proportional to the magnitude of the current. Each plot corresponds to a wave vector $k_\perp$, perpendicular to the plane of the representation, different energy of the incoming particle and/or different overlap, resulting in a transmission coefficient, T.

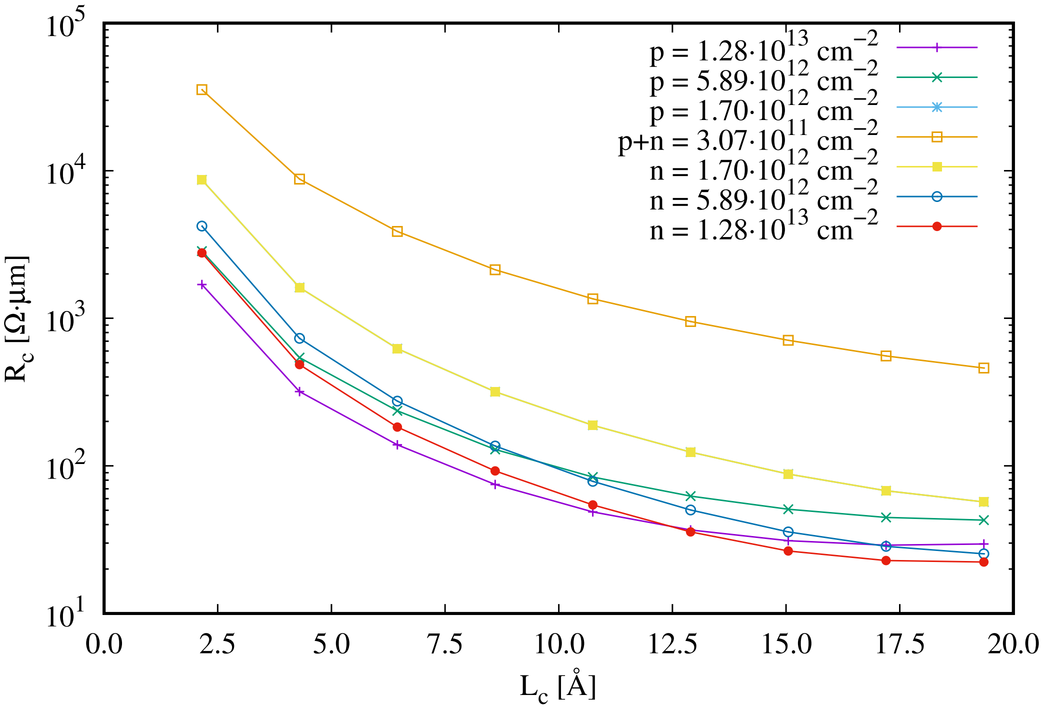

FIGURE 5.5: Specific Contact Resistance as a function of contact length for different graphene excess carrier concentrations at 300 K.

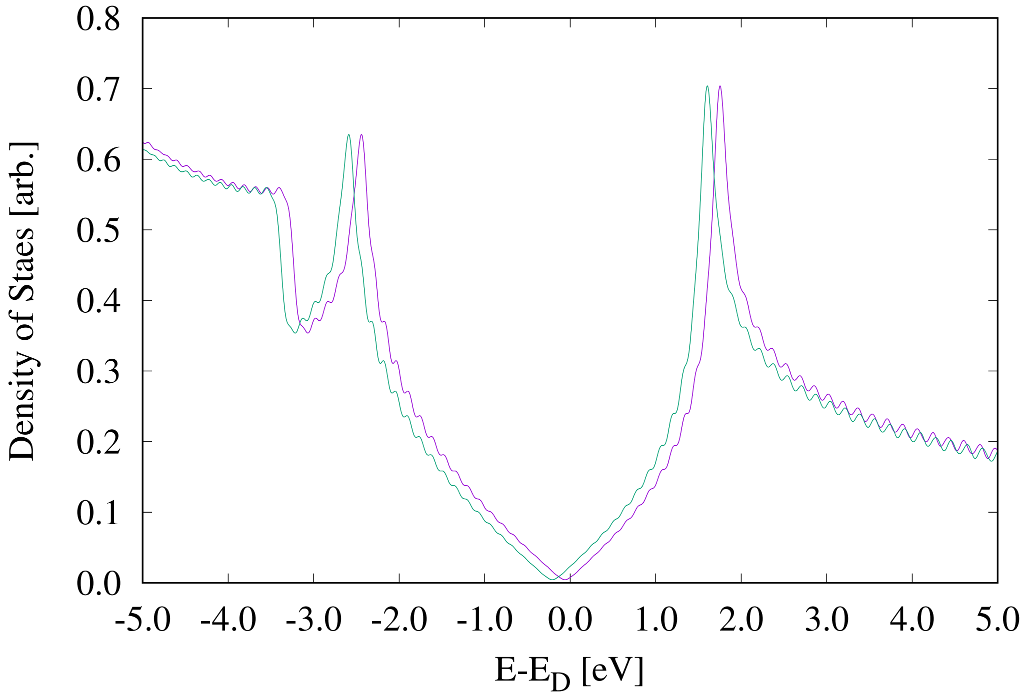

FIGURE 5.6: Graphene density of states (DOS) for pristine graphene compared with charged graphene such that the total charge accounts for $E_F - E_D = 0.2$ eV.

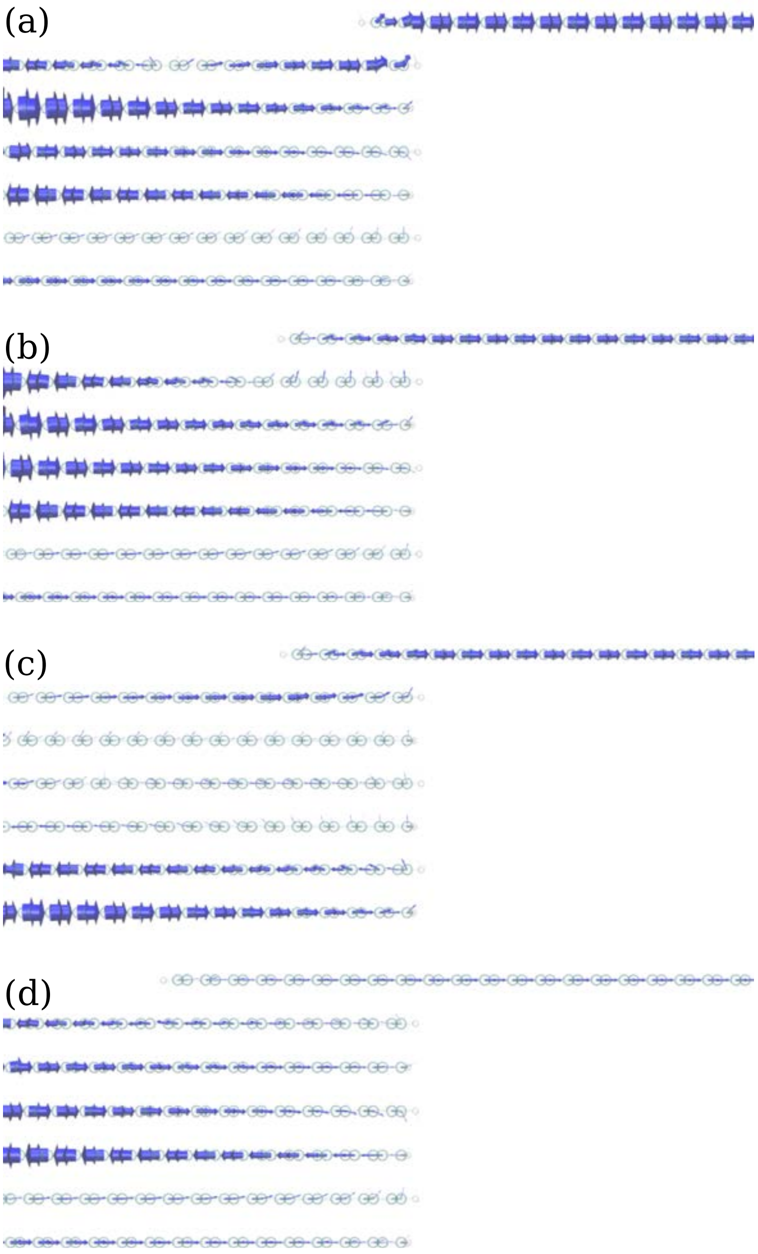

FIGURE 5.7: Current paths for different contact lenghts for both carriers at fixed $k_\perp$ = 0.660 $\pi/a_\perp$. (a) Overlap 2 for e: E = 0.105 eV, T = 0.99016, (b) Overlap 5 for e: E = 0.105 eV, T = 0.4890, (c) Overlap 5 for h: E = -0.105 eV, T = 0.51762, (d) Overlap 9 for e: E = 0.105 eV, T = 0.15161

Figures 5.7.(a)-(d) show the current lines for electrons in the cases with overlap 2, 5 and 9, with $k_\perp$ and E chosen in such a way that high T's are obtained. We can see that, as the overlap increases, injection becomes more distributed across the overlapping area, in opposition to the case of metal-graphene contacts [106], where only 1-2 metal-carbon bonds contributed to injection. Notwithstanding that, when only a very small area is available for injection (e.g. overlap 2), high transmission is still achievable, with nearly complete injection to graphene taking place through the last two pairs.

5.4 Discussion and summary

Of course, any graphite-graphene contact will eventually need to be contacted to metal leads. One set of measurements of the contact resistance of metal-multilayer graphene (1,3,4,$\sim$50,$\sim$100 layers) did not find any strong dependence on the number of layers, which was attributed to only the top layer or two of a graphene stack playing a role in the contact formation [97]. It is expected that a different fabrication procedure promoting the formation of edge metal-C bonds, such as demonstrated in Ref. [53], would significantly decrease the metal-graphite contact resistance.

In conclusion, it was shown that graphite-graphene contacts provide a promising route towards the reduction of the contact resistance in graphene FET channels. Although transfer lengths are significantly higher than in metal-graphene contacts, their magnitudes are still quite small, at a few tens of Å. In addition, edge graphite-graphene contacts are expected to have quite low contact resistance.

Chapter 6

Conclusions

This final chapter is devoted to the global conclusions of this thesis. Different devices, systems and geometries with the underlying theme of electronic devices based on 2D materials. Several techniques were used for different porpuses reaching widely different conclusions for each.

In chapter 3 both a MoS_2 based MOSFET and a MoS_2 $p-n$ junction was studied using the drift diffusion model using the fininte element method to solve these equations. However, the implementation of the Finite Element Method used in this thesis assumed bulk materials for all regions of simulation and dit not take into account quantum effects that are relevant when the dimensionality is low. To mitigate this, it is possible to define an effective set of parameters in order to find results that match the experimental results for the different devices at the expense of loosing physical meaning of some of the quantities. Moreover, it might still be good enough to study the radio-frequency characteristics but more testing is needed in this regard. For the $p-n$ junction simulation, some results were obtained that were used as a reference for other calculations. Its results were consistent with a 3D material with a very small mesh in the 2D channel.

In chapter 4 molecular dynamics in tandem with first principles methods were used to find a parametrisation on a particular forcefield, the bond order potential, to optimise its parameters for a very particular set of systems. The Bond Order Potential in the interpretation of Albe *et. al.* is the most suitable force field to describe the Metal-Carbon interaction and a set of parameters was found for Palladium and Nickel using the parallel tempering monte carlo algorithm for parameter optimisations. This algorithm is a very efficient tool for optimisation tasks that allows for a thorrow search of the configuration space while able to find optimal values on a certain region of this space. With this set of parameter, opens the possiblity of simulating a CVD-like deposition of a metal on graphene or to use the forcefield for a first geometry relaxation for larger systems involving these atoms for, say, *ab initio* calculations that would otherwise require a lot of time in these type of calculations. Moreover, the potential files are provided in appendix B.

Finally, in chapter 5, a graphite-graphene contact structure was developed and simulated with first principle methods as well as ballistic transport calculations using the non-equilibrium green function theory. These results look very promising for experimental use. It was shown that graphite-graphene contacts provide a promising route towards the reduction of the contact resistance in graphene FET channels. Although transfer lengths are significantly higher than in metal-graphene contacts, their magnitudes are still quite small, at a few tens of Å. In addition, edge graphite-graphene contacts are expected to have quite low contact resistance. Looking forward, this graphite-graphene structures will have to be attached to metallic contacts.

Appendix A

Geometries for the PTMC algorithm

All the different geometries for the Nickel Carbon training for the PTMC algorithm training.

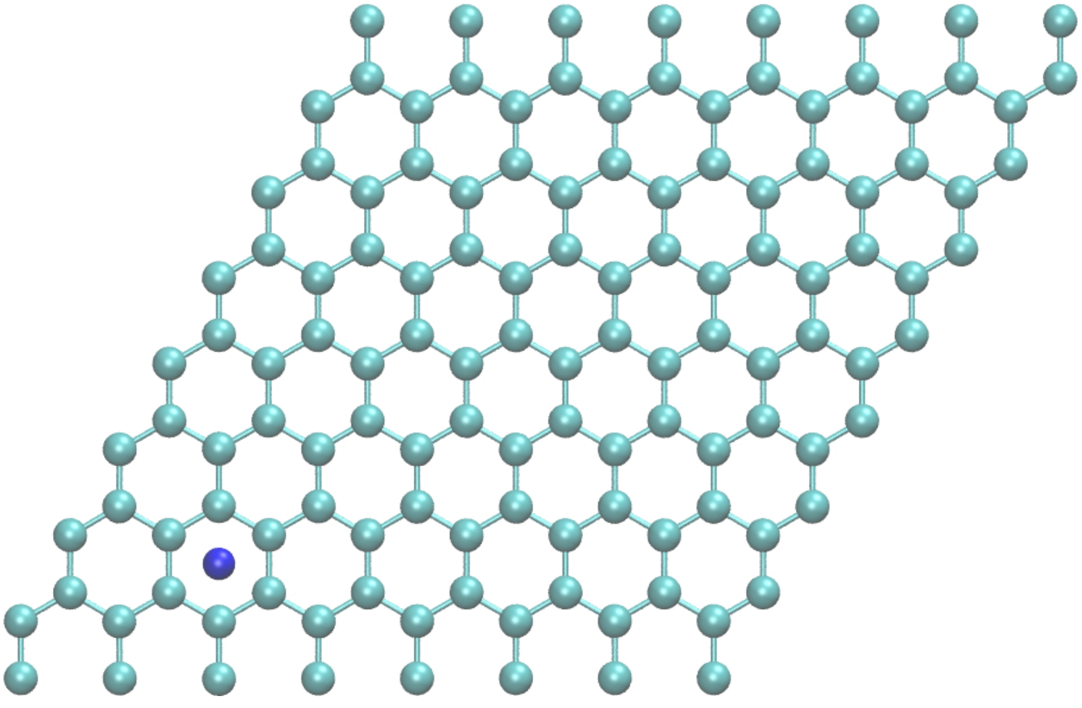

FIGURE A.1: Ni 1 top view on a hollow position on top of a graphene sheet.

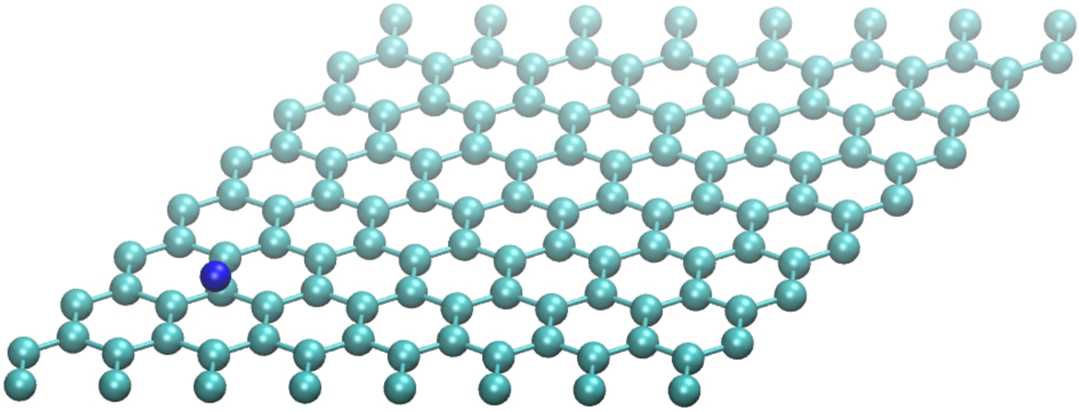

FIGURE A.2: Ni 1 lateral view on a hollow position on top of a graphene sheet.

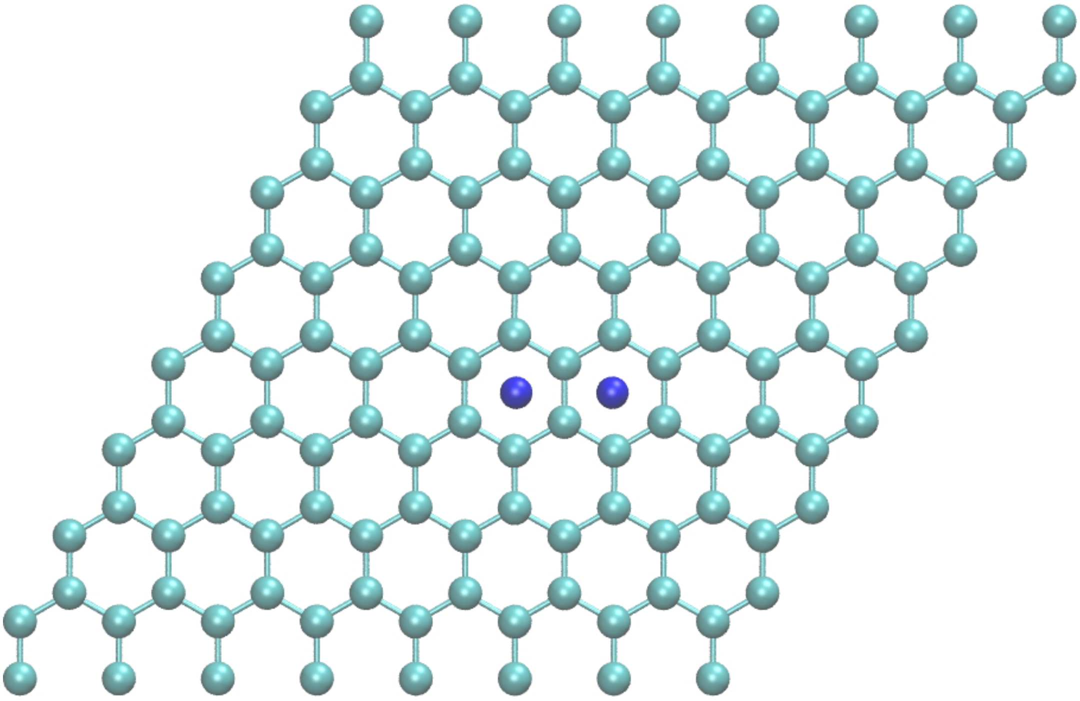

FIGURE A.3: Ni 2 top view on a hollow position on top of a graphene sheet.

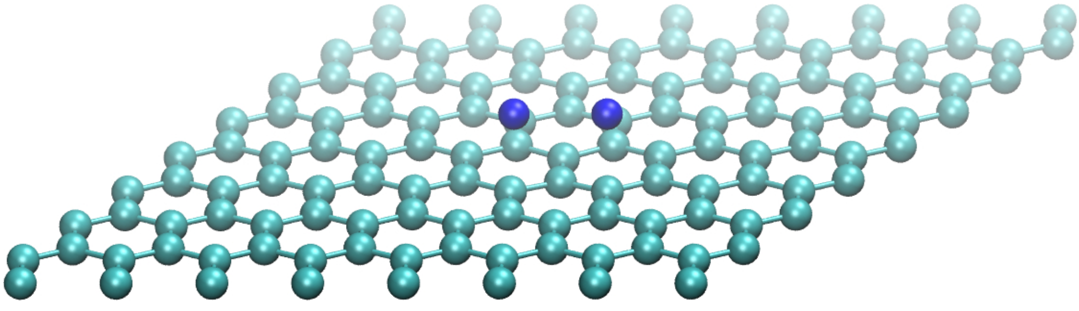

FIGURE A.4: Ni 2 lateral view on a hollow position on top of a graphene sheet.

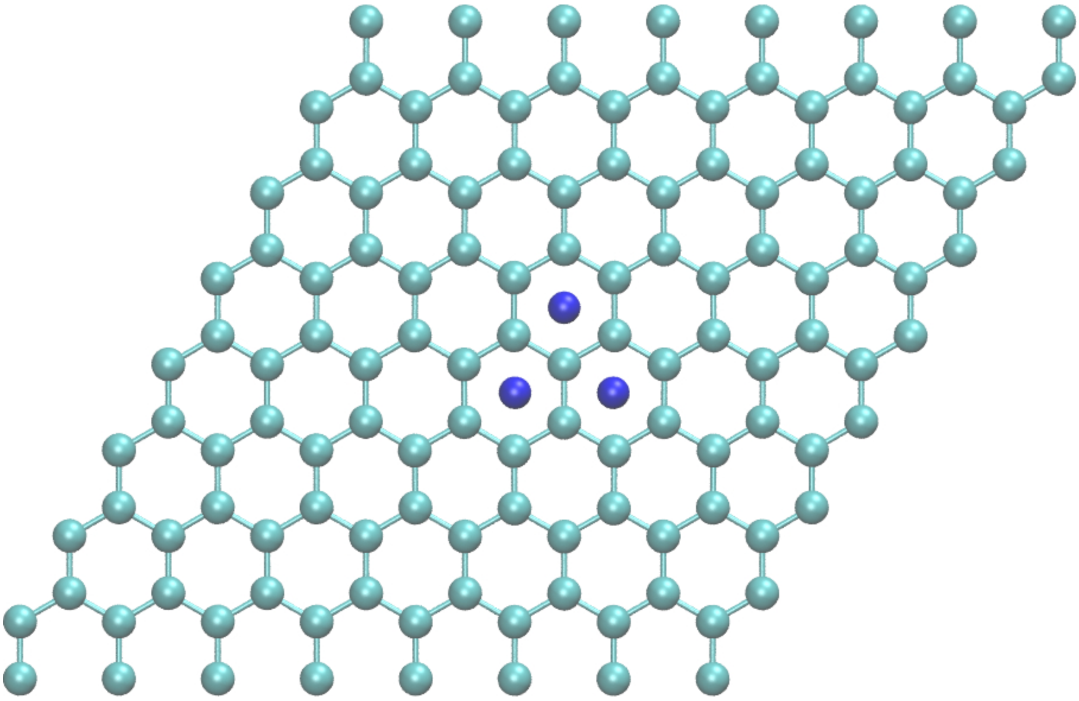

FIGURE A.5: Ni 3 top view on a hollow position on top of a graphene sheet.

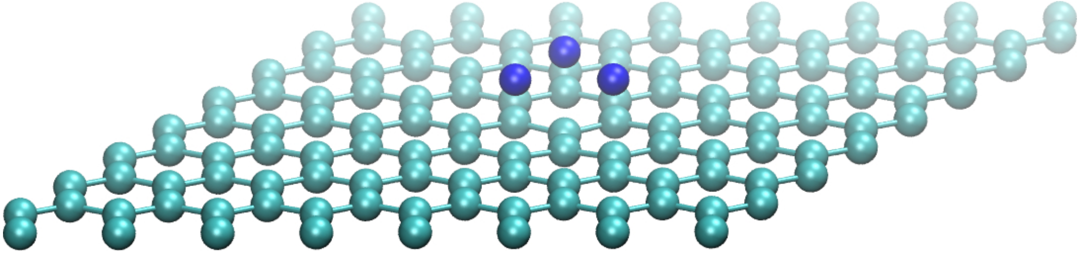

FIGURE A.6: Ni 3 lateral view on a hollow position on top of a graphene sheet.

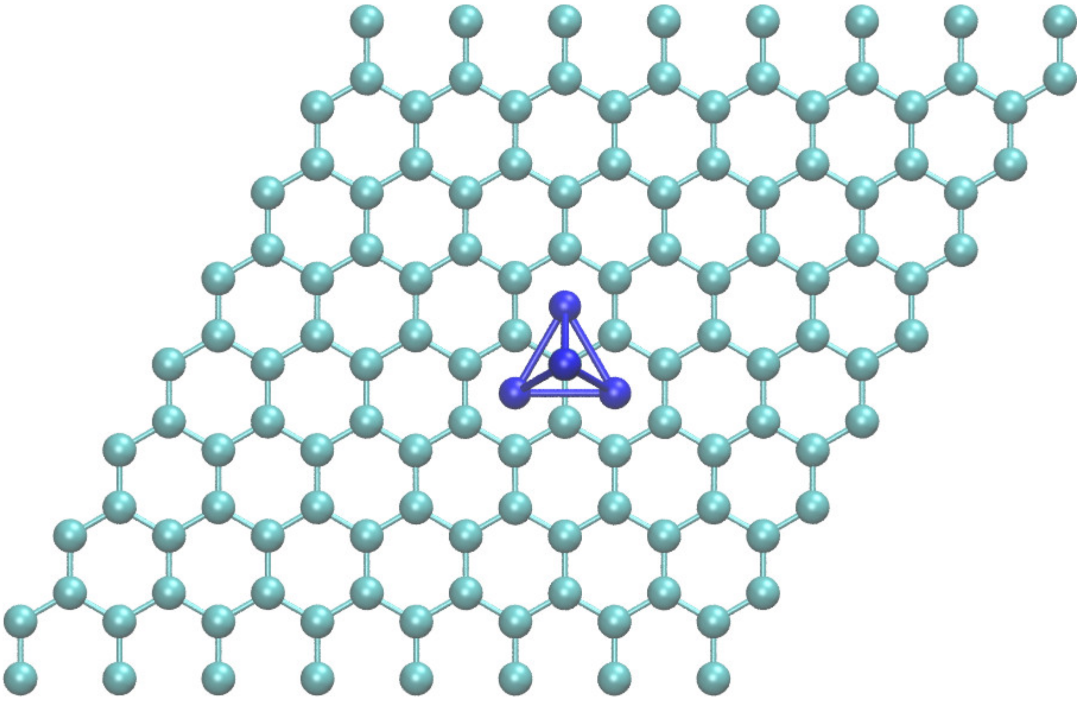

FIGURE A.7: Ni 4 top view on a hollow position forming a tetrahedron on top of a graphene sheet.

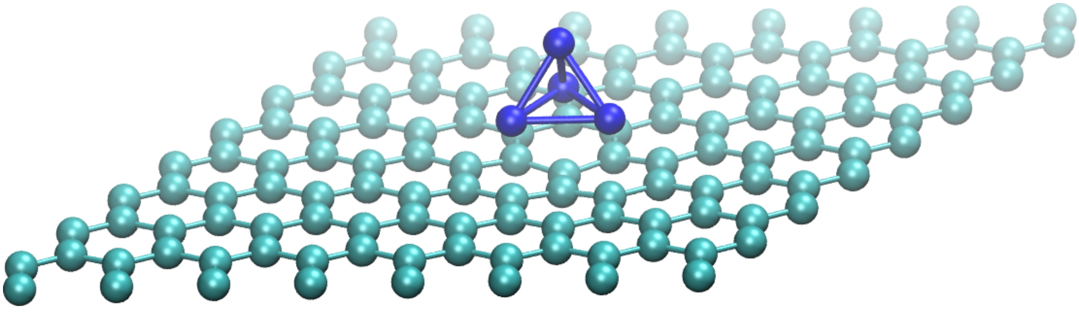

FIGURE A.8: Ni 4 lateral view on a hollow position forming a tetrahedron on top of a graphene sheet.

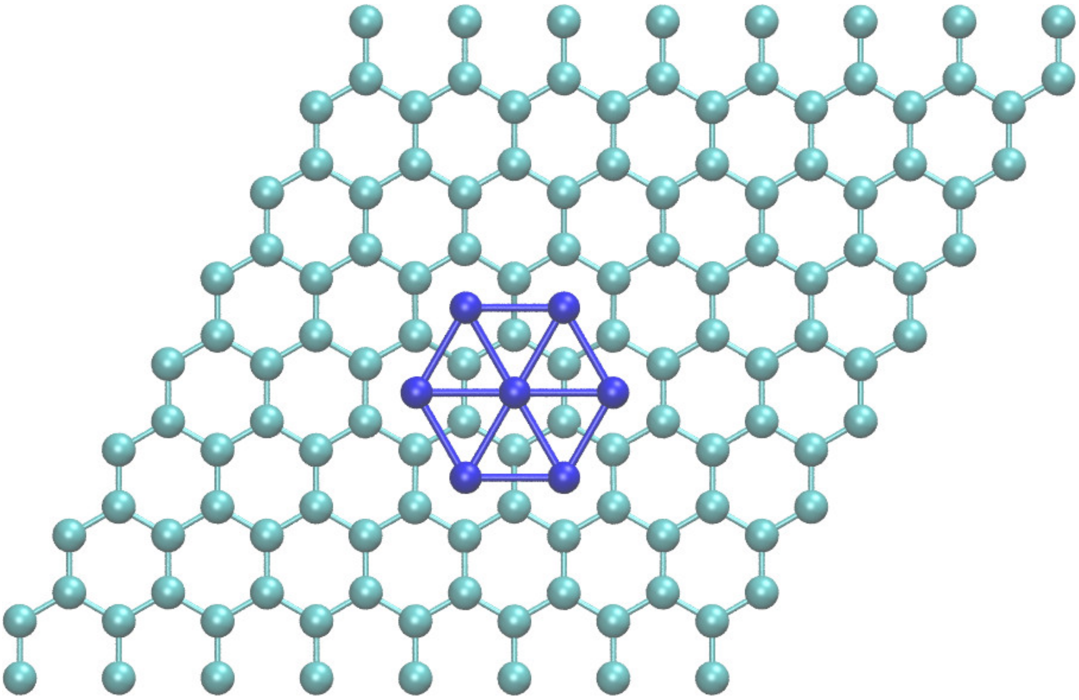

FIGURE A.9: Ni 7 top view on a hollow position forming a triangular lattice on top of a graphene sheet.

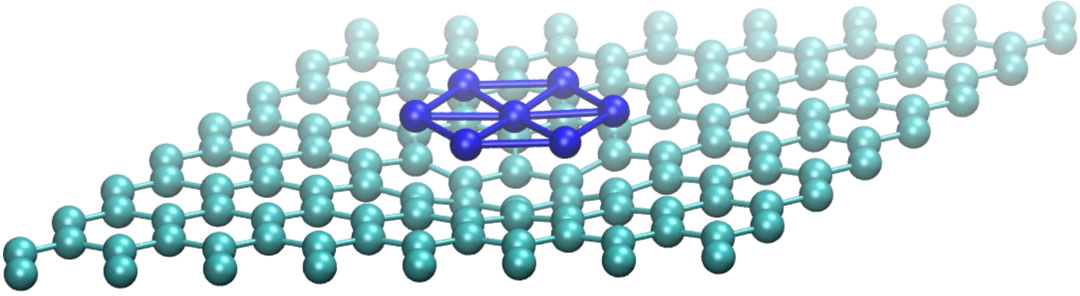

FIGURE A.10: Ni 7 lateral view on a hollow position forming a triangular lattice on top of a graphene sheet.

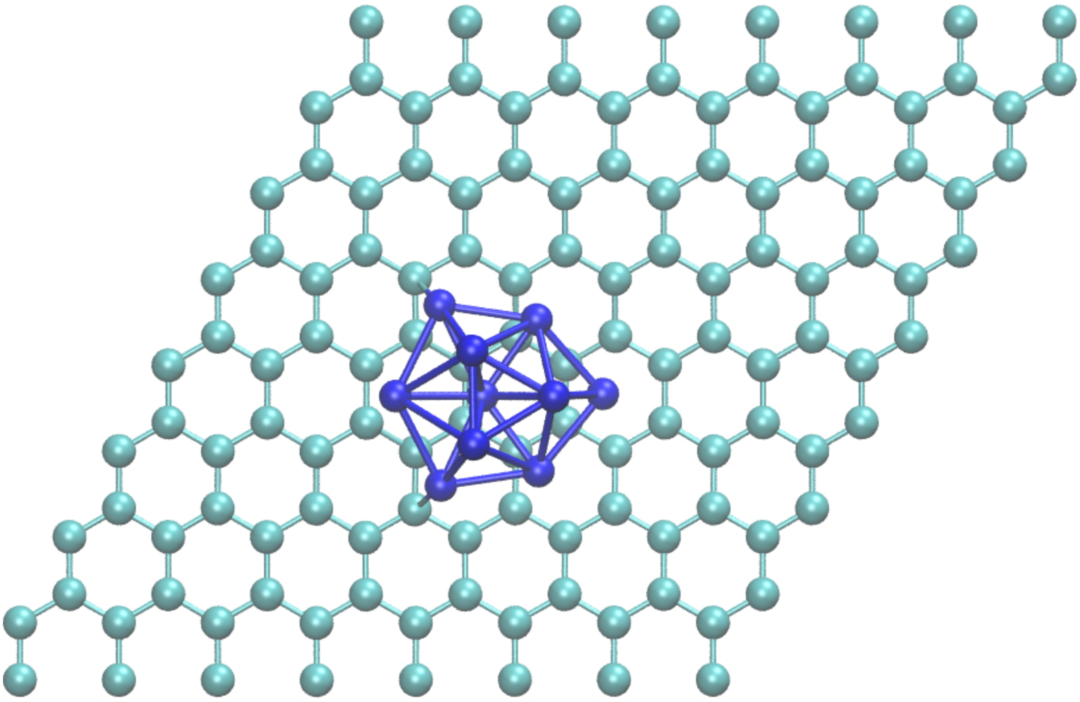

FIGURE A.11: Ni 10 top view on a hollow position forming a triangular lattice on top of a graphene sheet.

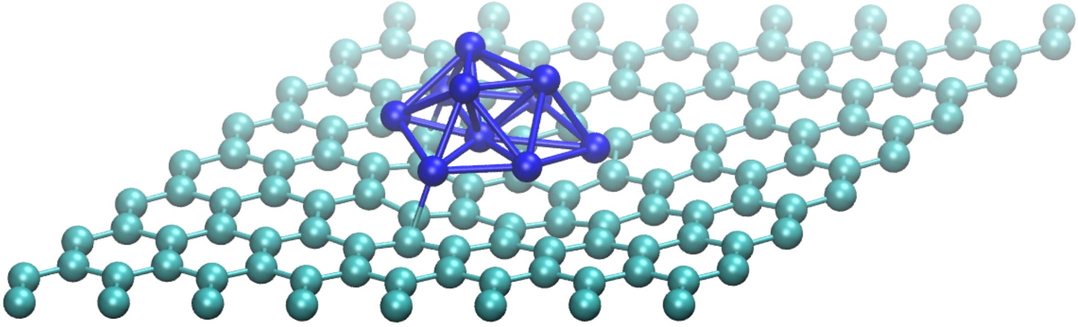

FIGURE A.12: Ni 10 lateral view on a hollow position forming a triangular lattice on top of a graphene sheet.

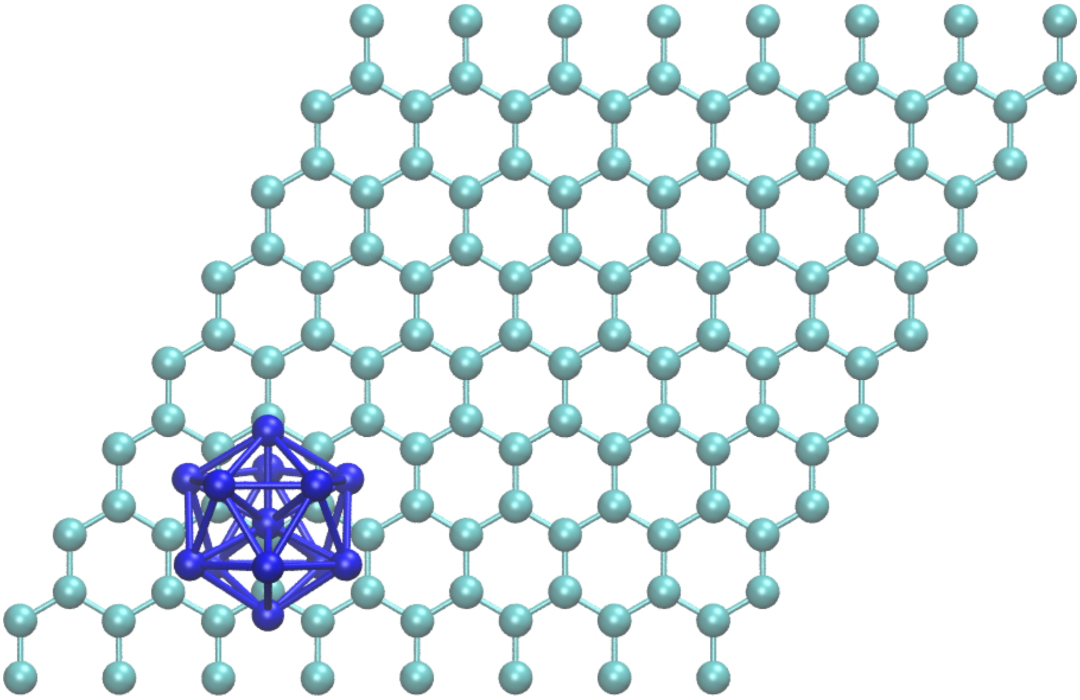

FIGURE A.13: Ni 13a top view on a hollow position forming a triangular lattice on top of a graphene sheet.

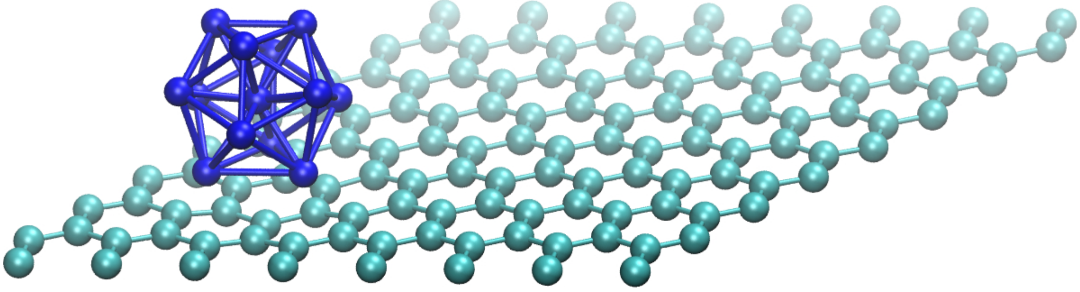

FIGURE A.14: Ni 13a lateral view on a hollow position forming a triangular lattice on top of a graphene sheet.

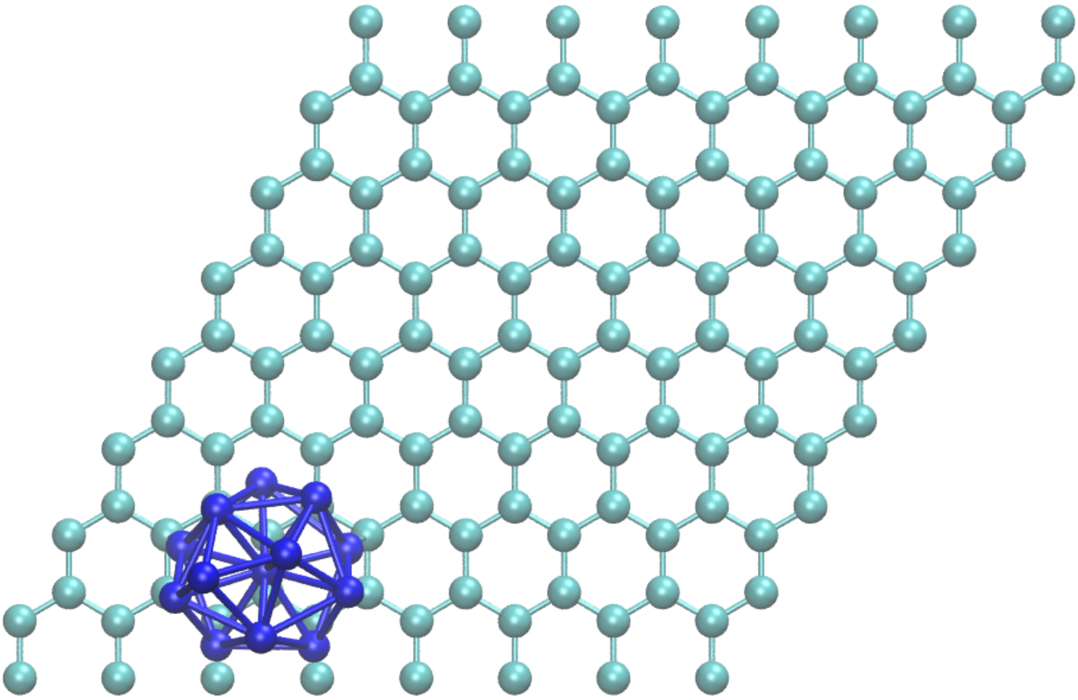

FIGURE A.15: Ni 13b top view on a hollow position forming a triangular lattice on top of a graphene sheet.

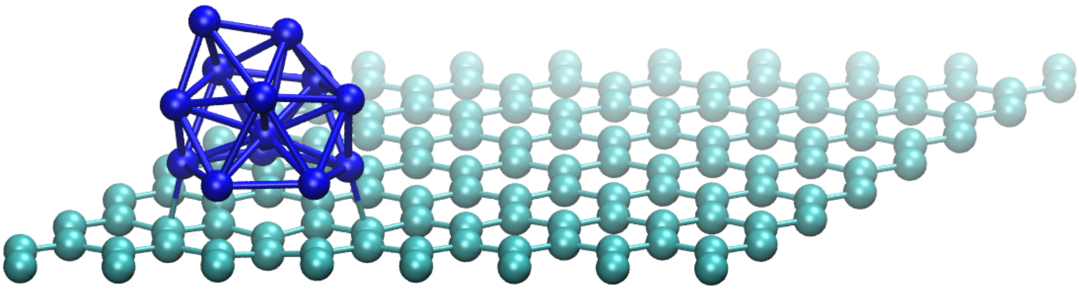

FIGURE A.16: Ni 13b lateral view on a hollow position forming a triangular lattice on top of a graphene sheet.

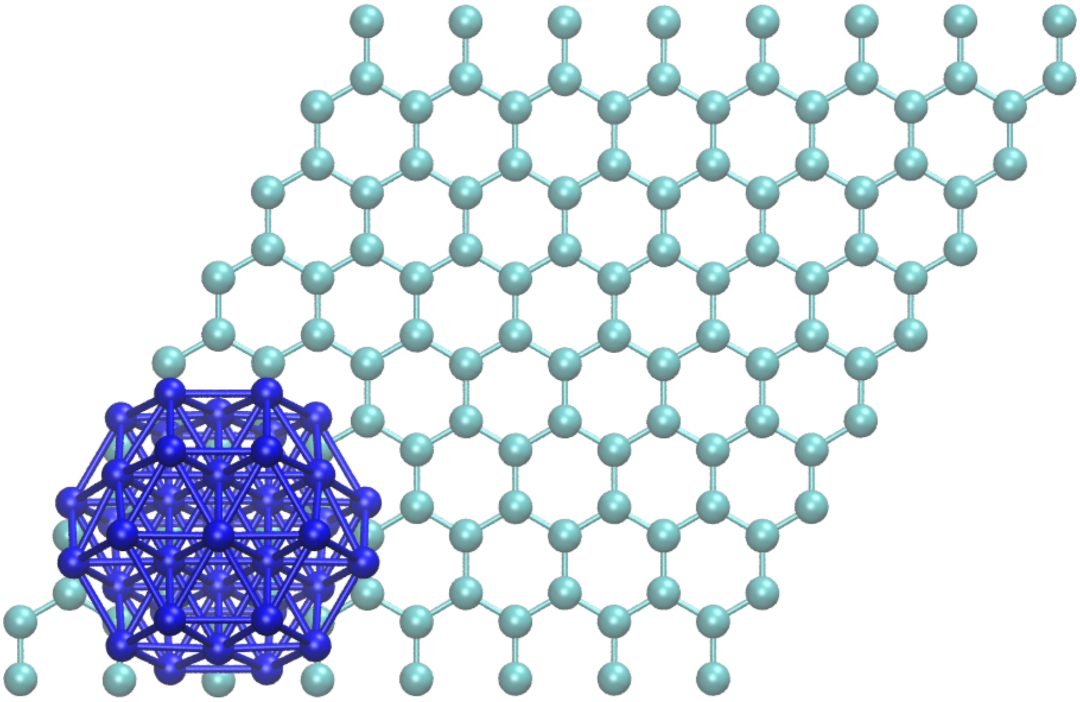

FIGURE A.17: Ni 38a top view on a hollow position forming a triangular lattice on top of a graphene sheet.

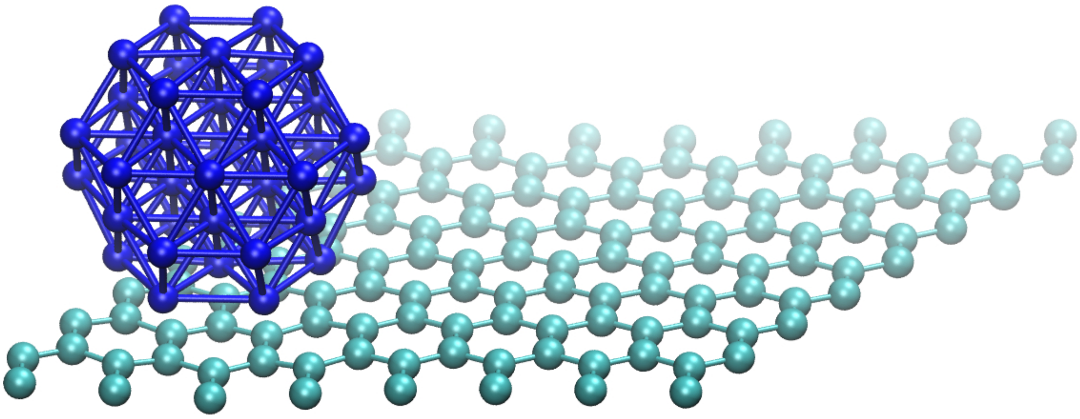

FIGURE A.18: Ni 38a lateral view on a hollow position forming a triangular lattice on top of a graphene sheet.

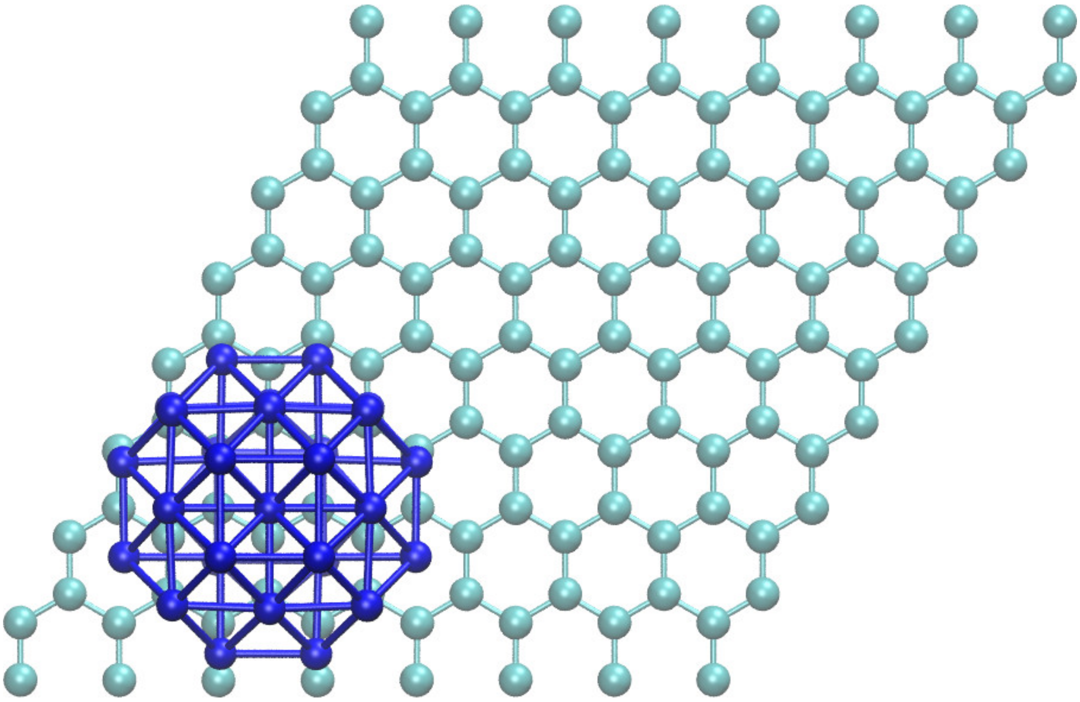

FIGURE A.19: Ni 38b top view on a hollow position forming a triangular lattice on top of a graphene sheet.

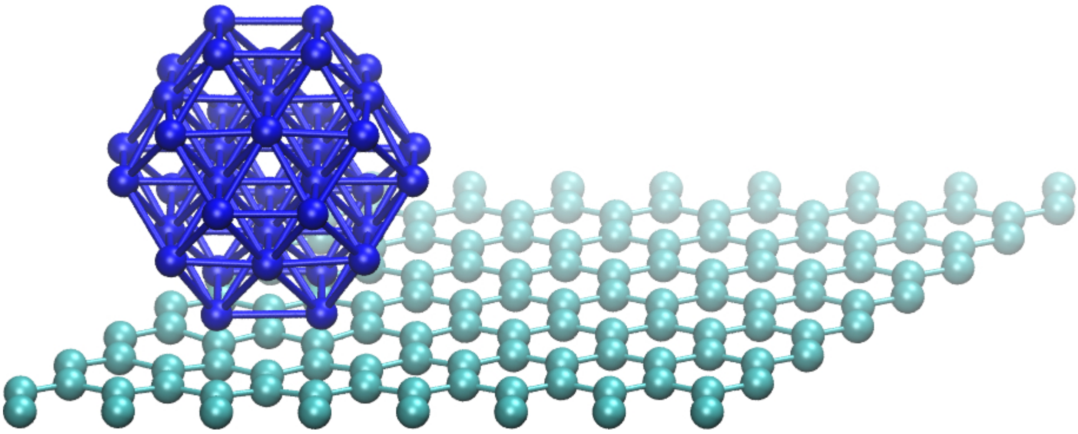

FIGURE A.20: Ni 38b lateral view on a hollow position forming a triangular lattice on top of a graphene sheet.

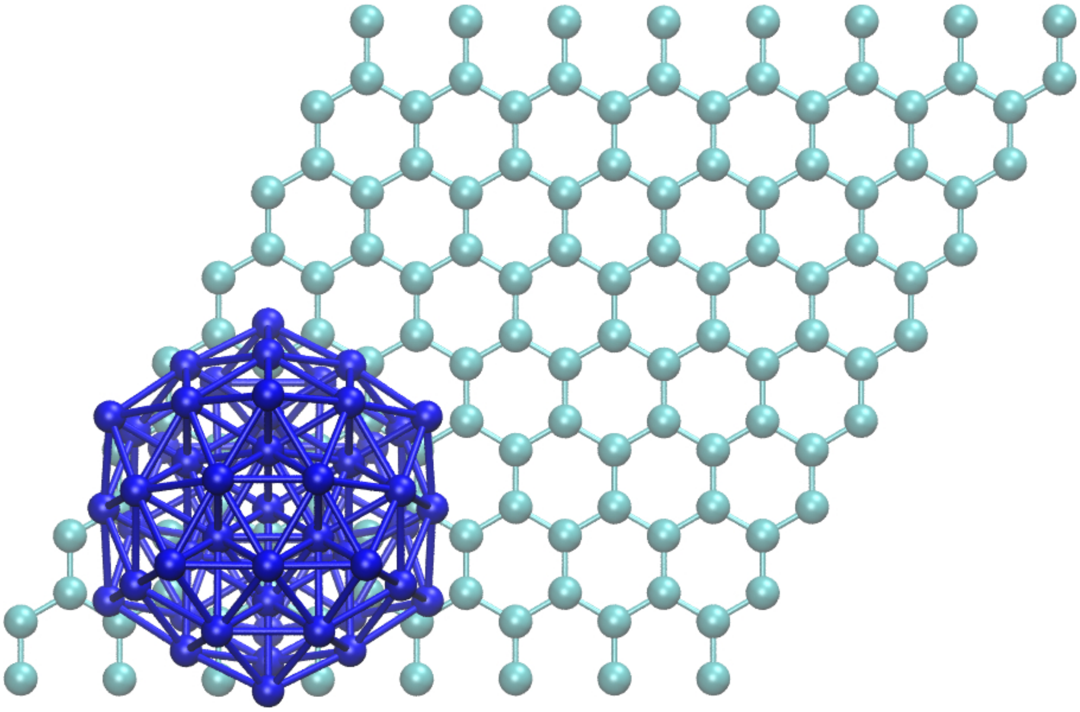

FIGURE A.21: Ni 55 top view on a hollow position forming a triangular lattice on top of a graphene sheet.

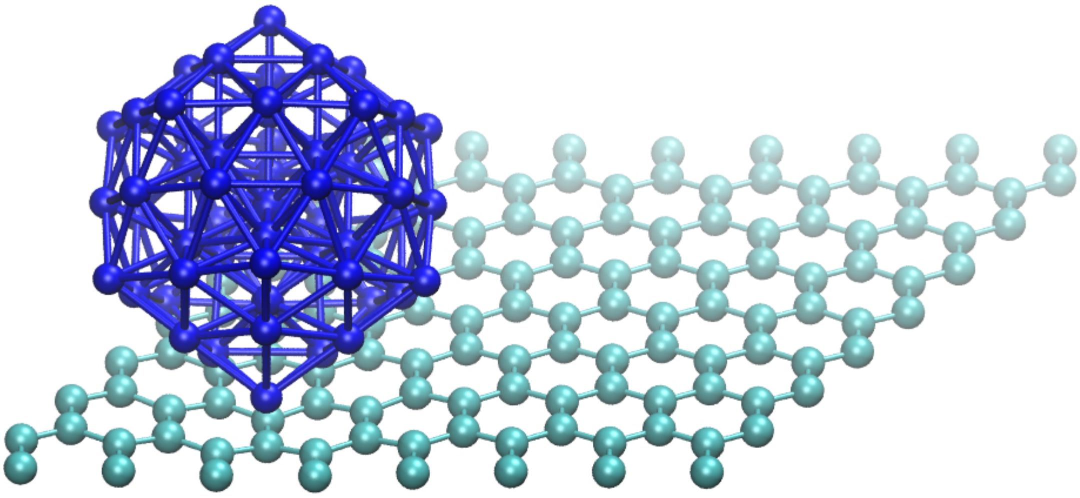

FIGURE A.22: Ni 55 lateral view on a hollow position forming a triangular lattice on top of a graphene sheet.

Appendix B

LAMMPS forcefield files

The follwing files are the forcefield files obtained in Chapter 4 and summarized in table 4.2 (pag.55) for the direct use in LAMMPS.

In the input file in LAMMPS the following lines must be included

```
pair_style  tersoff
pair_coeff  * * PdC.tersoff Pd C
```

for the case of a system including Palladium and Carbon. Equivalently for Nickel and Carbon. The file PdC.tersoff must be in the same directory as LAMMPS is being executed.

File: `PdC.tersoff`

```
# PdC.tersoff file for LAMMPS:
# format of a single entry (two lines):
#   element 1, element 2, element 3,  m, gamma, lambda3, \
    c, d, costheta0, n
#   beta, lambda2, B, R, D, lambda1, A

  C  C  C  1  2.0813000E-04  0.0000000E+00  3.3000000E+02  \
    3.5000000E+00 -1.0000000E+00  1
           1  2.6887745E+00  1.3970730E+03  1.8500000E+00  \
    6.0000000E-01  3.2803049E+00  2.6058416E+03

  C  C Pd  1  1.8063309E-02  5.6065639E+00  6.9036064E+02  \
    4.7553053E+00 -1.0000000E+00  0
           0  0  0  5.1412752E+00  3.9568795E-02  0  0

  C Pd  C  1  2.0813000E-04  0.0000000E+00  3.3000000E+02  \
```

```
    3.5000000E+00 -1.0000000E+00  0
           0  0  0  1.8500000E+00  6.0000000E-01  0  0

  C Pd Pd  1  1.8063309E-02  5.6065639E+00  6.9036064E+02  \
    4.7553053E+00 -1.0000000E+00  1
           1  5.0794563E-01  1.8333867E+00  5.1412752E+00  \
    3.9568795E-02  7.2827517E+01  1.7508654E+00

 Pd  C  C  1  1.8063309E-02  5.6065639E+00  6.9036064E+02  \
    4.7553053E+00 -1.0000000E+00  1
           1  5.0794563E-01  1.8333867E+00  5.1412752E+00  \
    3.9568795E-02  7.2827517E+01  1.7508654E+00

 Pd  C Pd  1  1.0000000E+00  2.7229160E+00  0.0000000E+00  \
    1.0000000E+00 -1.0000000E+00  0
           0  0  0  5.7500000E+00  6.0000000E-01  0  0

 Pd Pd  C  1  1.8063309E-02  5.6065639E+00  6.9036064E+02  \
    4.7553053E+00 -1.0000000E+00  0
           0  0  0  5.1412752E+00  3.9568795E-02  0  0

 Pd Pd Pd  1  1.0000000E+00  2.7229160E+00  0.0000000E+00  \
    1.0000000E+00 -1.0000000E+00  1
           1  1.3614580E+00  1.4493828E+02  5.7500000E+00  \
    6.0000000E-01  3.9537584E+00  1.8304268E+04
```

File: `NiC.tersoff`

```
# NiC.tersoff file for LAMMPS:
# format of a single entry (two lines):
#   element 1, element 2, element 3,  m, gamma, lambda3, \
    c, d, costheta0, n
#   beta, lambda2, B, R, D, lambda1, A

  C  C  C  1  2.0813000E-04  0.0000000E+00  3.3000000E+02  \
    3.5000000E+00 -1.0000000E+00  1
           1  2.6887745E+00  1.3970730E+03  1.8500000E+00  \
```

```
   6.0000000E-01  3.2803049E+00  2.6058416E+03

 C  C Ni  1  1.8002513E-02  5.6153061E+00  6.8886747E+02  \
   4.7534976E+00 -1.0000000E+00  0
          0  0  0  5.1500000E+00  2.0000000E-01  0  0

 C Ni  C  1  2.0813000E-04  0.0000000E+00  3.3000000E+02  \
   3.5000000E+00 -1.0000000E+00  0
          0  0  0  1.8500000E+00  6.0000000E-01  0  0

 C Ni Ni  1  1.8002513E-02  5.6153061E+00  6.8886747E+02  \
   4.7534976E+00 -1.0000000E+00  1
          1  5.0759784E-01  1.8329660E+00  5.1500000E+00  \
   2.0000000E-01  7.2725205E+01  1.7460343E+00

Ni  C  C  1  1.8002513E-02  5.6153061E+00  6.8886747E+02  \
   4.7534976E+00 -1.0000000E+00  1
          1  5.0759784E-01  1.8329660E+00  5.1500000E+00  \
   2.0000000E-01  7.2725205E+01  1.7460343E+00

Ni  C Ni  1  1.0000000E+00  9.5458412E-01  0.0000000E+00  \
   1.0000000E+00 -1.0000000E+00  0
          0  0  0  5.7500000E+00  6.0000000E-01  0  0

Ni Ni  C  1  1.8002513E-02  5.6153061E+00  6.8886747E+02  \
   4.7534976E+00 -1.0000000E+00  0
          0  0  0  5.1500000E+00  2.0000000E-01  0  0

Ni Ni Ni  1  1.0000000E+00  9.5458412E-01  0.0000000E+00  \
   1.0000000E+00 -1.0000000E+00  1
          1  4.7729206E-01  7.0273229E+00  5.7500000E+00  \
   6.0000000E-01  6.8237912E+00  1.8146369E+06
```

Bibliography

[1] K. Albe, K. Nordlund, and R. S. Averback. "Modeling the metal-semiconductor interaction: Analytical bond-order potential for platinum-carbon". In: *Physical Review B* 65.19 (2002), p. 195124. ISSN: 0163-1829. DOI: 10.1103/PhysRevB.65.195124.

[2] A. Allain et al. "Electrical contacts to two-dimensional semiconductors". In: *Nat. Mater.* 14 (2015), pp. 1195–1205. DOI: 10.1038/nmat4452.

[3] N. W. Ashcroft, N. D. Mermin, and S. Rodriguez. *Solid state physics*. AAPT, 1978.

[4] E. Bersch et al. "Band offsets of ultrathin high-κ oxide films with Si". In: *Phys. Rev. B* 78 (8 2008), p. 085114. DOI: 10.1103/PhysRevB.78.085114.

[5] F. Bloch. "Über die Quantenmechanik der Elektronen in Kristallgittern". In: *Zeitschrift fur Physik* 52.7-8 (1929), pp. 555–600. DOI: 10.1007/BF01339455.

[6] K.I. Bolotin et al. "Ultrahigh electron mobility in suspended graphene". In: *Solid State Communications* 146.9 (2008), pp. 351 –355. ISSN: 0038-1098. DOI: https://doi.org/10.1016/j.ssc.2008.02.024.

[7] M. Born and R. Oppenheimer. "Zur Quantentheorie der Molekeln". In: *Annalen der Physik* 389.20 (), pp. 457–484. DOI: 10.1002/andp.19273892002.

[8] M. Brandbyge et al. "Density-functional method for nonequilibrium electron transport". In: *Phys. Rev. B* 65 (16 2002), p. 165401. DOI: 10.1103/PhysRevB.65.165401.

[9] D. W. Brenner. "Empirical potential for hydrocarbons for use in simulating the chemical vapor deposition of diamond films". In: *Phys. Rev. B* 42 (15 1990), pp. 9458–9471. DOI: 10.1103/PhysRevB.42.9458.

[10] D. W. Brenner et al. "A second-generation reactive empirical bond order (REBO) potential energy expression for hydrocarbons". In: *Journal of Physics: Condensed Matter* 14.4 (2002), pp. 783–802. DOI: 10.1088/0953-8984/14/4/312.

[11] Cg Broyden. "A class of methods for solving nonlinear simultaneous equations". In: *Math. Comput.* 19.92 (1965), pp. 577–593. DOI: 10.2307/2003941.

[12] D. M. Ceperley and B. J. Alder. “Ground State of the Electron Gas by a Stochastic Method”. In: *Phys. Rev. Lett.* 45 (7 1980), pp. 566–569. DOI: 10.1103/PhysRevLett.45.566.

[13] T. Chari et al. “Resistivity of rotated graphite-graphene contacts”. In: *Nano Letters* 16.7 (2016), pp. 4477–4482. DOI: 10.1021/acs.nanolett.6b01657.

[14] F. A. Chaves et al. “Physical model of the contact resistivity of metal-graphene junctions”. In: *Journal of Applied Physics* 115.16 (2014), p. 164513.

[15] F. Cleri and V. Rosato. “Tight-binding potentials”. In: *Computer Simulation in Materials Science* 205.1 (1991), pp. 233–253. DOI: 10.1007/978-94-011-3546-7_11.

[16] F. Cleri and V. Rosato. “Tight-binding potentials for transition metals and alloys”. In: *Phys. Rev. B* 48 (1 1993), pp. 22–33. DOI: 10.1103/PhysRevB.48.22.

[17] S. Datta. *Electronic Transport in Mesoscopic Systems*. Cambridge Studies in Semiconductor Physi. Cambridge University Press, 1997. ISBN: 9780521599436.

[18] M. Dion et al. “Van der Waals Density Functional for General Geometries”. In: *Phys. Rev. Lett.* 92 (24 2004), p. 246401. DOI: 10.1103/PhysRevLett.92.246401.

[19] Y. Du et al. “Contact research strategy for emerging molybdenum disulfide and other two-dimensional field-effect transistors”. In: *APL Mater.* 2.9 (2014), p. 092510. DOI: 10.1063/1.4894198.

[20] P. Erhart and K. Albe. “Analytical potential for atomistic simulations of silicon, carbon, and silicon carbide”. In: *Physical Review B* 71.3 (2005), p. 35211. DOI: 10.1103/PhysRevB.71.035211.

[21] T. Fang et al. “Carrier statistics and quantum capacitance of graphene sheets and ribbons”. In: *Appl. Phys. Lett.* 91.9 (2007), p. 092109. DOI: 10.1063/1.2776887.

[22] R. P. Feynman. “Forces in Molecules”. In: *Phys. Rev.* 56 (4 1939), pp. 340–343. DOI: 10.1103/PhysRev.56.340.

[23] G. Fiori et al. “Electronics based on two-dimensional materials”. In: *Nature Nanotechnology* 9 (2014), p. 768. DOI: 10.1038/nmat3169.

[24] D. S. Fisher and P. A. Lee. “Relation between conductivity and transmission matrix”. In: *Phys. Rev. B* 23 (12 1981), pp. 6851–6854. DOI: 10.1103/PhysRevB.23.6851.

[25] G. D. Förster. “Atomistic modeling of metallic nanoparticles on carbonaceous substrates and epitaxial graphene on metals”. PhD thesis. Université Claude Bernard de Lyon, 2015.

[26] G. D. Förster, F. Rabilloud, and F. Calvo. "Atomistic modeling of epitaxial graphene on Ru(0001) and deposited ruthenium nanoparticles". In: *Phys. Rev. B* 92 (16 2015), p. 165425. DOI: `10.1103/PhysRevB.92.165425`.

[27] T. Frederiksen et al. "Inelastic transport theory from first principles: Methodology and application to nanoscale devices". In: *Phys. Rev. B* 75.20 (2007), p. 205413. DOI: `10.1103/PhysRevB.75.205413`.

[28] D. Frenkel et al. "Understanding molecular simulation". In: *Computers in Physics* 11.4 (1997), pp. 351–354.

[29] S. García-Gil et al. "Optimal strictly localized basis sets for noble metal surfaces". In: *Phys. Rev. B* 79 (7 2009), p. 075441. DOI: `10.1103/PhysRevB.79.075441`.

[30] A. K. Geim and I. V. Grigorieva. "Van der Waals heterostructures". In: *Nature* 499 (2013), pp. 419–425. DOI: `10.1038/nature12385`.

[31] A. K. Geim and K. S. Novoselov. "The rise of graphene". In: *Nature Materials* 6.3 (2007), pp. 183–191. DOI: `10.1038/nmat1849`.

[32] W. Gerlach and O. Stern. "Das magnetische Moment des Silberatoms". In: *Zeitschrift fur Physik* 9.1 (1922), pp. 353–355. ISSN: 1434-6001. DOI: `10.1007/BF01326984`.

[33] W. Gerlach and O. Stern. "Der experimentelle Nachweis der Richtungsquantelung im Magnetfeld". In: *Zeitschrift fur Physik* 9.1 (1922), pp. 349–352. ISSN: 1434-6001. DOI: `10.1007/BF01326983`.

[34] W. Gerlach and O. Stern. "Der experimentelle Nachweis des magnetischen Moments des Silberatoms". In: *Zeitschrift fur Physik* 8.1 (1922), pp. 110–111. ISSN: 1434-6001. DOI: `10.1007/BF01329580`.

[35] G. Green. "An Essay on the Application of mathematical Analysis to the theories of Electricity and Magnetism ." In: 39.1850 (1854), pp. 161–221. arXiv: `arXiv:0807.0088v1`.

[36] S. Gupta et al. "Contact resistivity reduction through interfacial layer doping in metal-interfacial layer-semiconductor contacts". In: *J. Appl. Phys.* 113.23 (2013), p. 234505. DOI: `10.1063/1.4811340`.

[37] Shu-Jen Han et al. "High-Frequency Graphene Voltage Amplifier". In: *Nano Letters* 11.9 (2011), pp. 3690–3693. DOI: `10.1021/nl2016637`.

[38] D.R. Hartree. "The Wave Mechanics of an Atom with a Non-Coulomb Central Field Part I Theory and Methods". In: *Mathematical Proceedings of the Cambridge Philosophical Society* 24.1 (1928), pp. 89–110. DOI: `10.1017/S0305004100011919`.

[39] H. Hellmann. *Einführung in Die Quantenchemie*. Springer-Verlag, 2015.

[40] P. Hohenberg and W. Kohn. "Inhomogeneous Electron Gas". In: *Phys. Rev.* 136 (3B 1964), B864–B871. DOI: `10.1103/PhysRev.136.B864`.

[41] W. Humphrey, A. Dalke, and K. Schulten. "VMD – Visual Molecular Dynamics". In: *Journal of Molecular Graphics* 14 (1996), pp. 33–38.

[42] Martin J. et al. "Observation of electron–hole puddles in graphene using a scanning single-electron transistor". In: *Nature Physics* 4 (144 2007). DOI: `10.1038/nphys781`.

[43] F. Jovell Megias. "Drift Difusion Simulation of a 2D channel based Field Effect Transistor". MA thesis. Universitat Autònoma de Barcelona, 2014.

[44] R. Kappera et al. "Phase-engineered low-resistance contacts for ultrathin MoS_2 transistors". In: *Nat. Mater.* 13 (2014), pp. 1128–1134. DOI: `10.1038/nmat4080`.

[45] C. Kittel, P. McEuen, and P. McEuen. *Introduction to solid state physics*. Vol. 8. Wiley New York, 1996.

[46] K. Kobayashi and J. Yamauchi. "Electronic structure and scanning-tunneling-microscopy image of molybdenum dichalcogenide surfaces". In: *Phys. Rev. B* 51 (23 1995), pp. 17085–17095. DOI: `10.1103/PhysRevB.51.17085`.

[47] W. Kohn and L. J. Sham. "Self-Consistent Equations Including Exchange and Correlation Effects". In: *Phys. Rev.* 140 (4A 1965), A1133–A1138. DOI: `10.1103/PhysRev.140.A1133`.

[48] F. H. L. Koppens et al. "Photodetectors based on graphene, other two-dimensional materials and hybrid systems". In: *Nature Nanotechnology* 9 (2014), pp. 780–793. DOI: `10.1038/nnano.2014.215`.

[49] H. W. Kroto et al. "C60: Buckminsterfullerene". In: *Nature* 318 (1985), pp. 162–163. DOI: `10.1038/318162a0`.

[50] R. Landauer. "Spatial Variation of Currents and Fields Due to Localized Scatterers in Metallic Conduction". In: *IBM Journal of Research and Development* 1.3 (1957), pp. 223–231. DOI: `10.1147/rd.13.0223`.

[51] Chul-Ho Lee et al. "Atomically thin p–n junctions with van der Waals heterointerfaces". In: *Nature Nanotechnology* 9 (2014), pp. 676–681. DOI: `10.1038/nnano.2014.150`.

[52] *Cohesion*. Vol. 43. 5. 1931, p. 461.

[53] WS. Leong, H. Gong, and J. T. L. Thong. “Low-Contact-Resistance Graphene Devices with Nickel-Etched-Graphene Contacts”. In: *ACS Nano* 8.1 (2014), pp. 994–1001. DOI: `10.1021/nn405834b`.

[54] Hai Li et al. “Preparation and Applications of Mechanically Exfoliated Single-Layer and Multilayer MoS2 and WSe2 Nanosheets”. In: *Accounts of Chemical Research* 47.4 (2014), pp. 1067–1075. DOI: `10.1021/ar4002312`.

[55] B. A. Lippmann and J. Schwinger. “Variational Principles for Scattering Processes. I”. In: *Phys. Rev.* 79 (3 1950), pp. 469–480. DOI: `10.1103/PhysRev.79.469`.

[56] W. Liu, C. Hierold, and M. Haluska. “Electrical contacts to individual SWCNTs: A review”. In: *Beilstein J. Nanotechnol.* 5 (2014), pp. 2202–2215. DOI: `10.3762/bjnano.5.229`.

[57] Yuan Liu et al. “Van der Waals heterostructures and devices”. In: *Nature Reviews Materials* 1.16042 (2016). DOI: `10.1038/natrevmats.2016.42`.

[58] Per-Olov Löwdin. “Quantum Theory of Many-Particle Systems. III. Extension of the Hartree-Fock Scheme to Include Degenerate Systems and Correlation Effects”. In: *Phys. Rev.* 97 (6 1955), pp. 1509–1520. DOI: `10.1103/PhysRev.97.1509`.

[59] R. M. Martin. *Electronic structure: basic theory and practical methods*. Cambridge university press, 2004.

[60] S. Hans Martin and T. Walter. “QM/MM Methods for Biomolecular Systems”. In: *Angewandte Chemie International Edition* 48.7 (), pp. 1198–1229. DOI: `10.1002/anie.200802019`.

[61] D. Marx and J. Hutter. “Ab initio molecular dynamics”. In: *Parallel computing* 309.309 (2009), p. 327.

[62] N. Metropolis and E. C. Nelson. “Early Computing at Los Alamos”. In: *Annals of the History of Computing* 4.4 (1982), pp. 348–357. DOI: `10.1109/MAHC.1982.10035`.

[63] J. W. Mintmire, B. I. Dunlap, and C. T. White. “Are fullerene tubules metallic?” In: *Phys. Rev. Lett.* 68 (5 1992), pp. 631–634. DOI: `10.1103/PhysRevLett.68.631`.

[64] H. J. Monkhorst and J. D. Pack. “Special points for Brillouin-zone integrations”. In: *Phys. Rev. B* 13 (12 1976), pp. 5188–5192. DOI: `10.1103/PhysRevB.13.5188`.

[65] G. E. Moore. “Cramming more components onto integrated circuits”. In: 86.1 (1965), pp. 82–85.

[66] J. Nord et al. "Modelling of compound semiconductors: analytical bond-order potential for gallium, nitrogen and gallium nitride". In: *Journal of Physics: Condensed Matter* 15.32 (2003), pp. 5649–5662. DOI: `10.1088/0953-8984/15/32/324`.

[67] K. S. Novoselov et al. "A roadmap for graphene". In: *Nature* 490 (2012), pp. 192–200. DOI: `10.1038/nature11458`.

[68] K. S. Novoselov et al. "Electric Field Effect in Atomically Thin Carbon Films". In: *Science* 306.5696 (2004), pp. 666–669. DOI: `10.1126/science.1102896`.

[69] K. S. Novoselov et al. "Two-dimensional atomic crystals". In: *Proceedings of the National Academy of Sciences* 102.30 (2005), pp. 10451–10453. DOI: `10.1073/pnas.0502848102`.

[70] K. S. Novoselov et al. "Two-dimensional gas of massless Dirac fermions in graphene". In: *Nature* 438 (2005), pp. 197–200. DOI: `10.1038/nature04233`.

[71] Pulay P. "Improved SCF convergence acceleration". In: *Journal of Computational Chemistry* 3.4 (), pp. 556–560. DOI: `10.1002/jcc.540030413`.

[72] Wendel S. P. and J. J. Palacios. "A theoretical study of the electrical contact between metallic and semiconducting phases in monolayer MoS 2". In: *2D Mater.* 4.1 (2017), p. 015014. DOI: `10.1088/2053-1583/4/1/015014`.

[73] T. Palacios, A. Hsu, and H. Wang. "Applications of graphene devices in RF communications". In: *IEEE Communications Magazine* 48.6 (2010), pp. 122–128. ISSN: 0163-6804. DOI: `10.1109/MCOM.2010.5473873`.

[74] N. Papior et al. "Improvements on non-equilibrium and transport Green function techniques: The next-generation TRANSIESTA". In: *Computer Physics Communications* 212 (2017), pp. 8–24. DOI: `10.1016/j.cpc.2016.09.022`.

[75] JU. Park et al. "Synthesis of monolithic graphene–graphite integrated electronics". In: *Nature Materials* 11 (2011). DOI: `10.1038/nmat3169`.

[76] M. Paulsson and M. Brandbyge. "Transmission eigenchannels from nonequilibrium Green's functions". In: *Phys. Rev. B* 76.11 (2007), p. 115117. DOI: `10.1103/PhysRevB.76.115117`.

[77] J. P. Perdew, K. Burke, and M. Ernzerhof. "Generalized Gradient Approximation Made Simple". In: *Phys. Rev. Lett.* 77 (18 1996), pp. 3865–3868. DOI: `10.1103/PhysRevLett.77.3865`.

[78] J. P. Perdew and Alex Zunger. "Self-interaction correction to density-functional approximations for many-electron systems". In: *Phys. Rev. B* 23 (10 1981), pp. 5048–5079. DOI: `10.1103/PhysRevB.23.5048`.

[79] S. Plimpton. "Fast Parallel Algorithms for Short – Range Molecular Dynamics". In: *Journal of Computational Physics* 117.June 1994 (1995), pp. 1–19. ISSN: 00219991. DOI: `10.1006/jcph.1995.1039`. URL: `http://lammps.sandia.gov`.

[80] P. Pulay. "Convergence acceleration of iterative sequences. The case of scf iteration". In: *Chemical Physics Letters* 73.2 (1980), pp. 393 –398. DOI: `https://doi.org/10.1016/0009-2614(80)80396-4`.

[81] B. Radisavljevic et al. "Single-layer MoS2 transistors". In: *Nat. Nanotechnol.* 6.3 (2011), pp. 147–150. DOI: `10.1038/nnano.2010.279`. eprint: `0402594v3`.

[82] J. Robertson. "High dielectric constant oxides". In: *The European Physical Journal - Applied Physics* 28.3 (2004), 265–291. DOI: `10.1051/epjap:2004206`.

[83] Max Roser and Hannah Ritchie. *Technological Progress*. `https://ourworldindata.org/technological-progress`. Published online at OurWorldInData.org [online resource]. 2018.

[84] H. Rydberg et al. "Van der Waals Density Functional for Layered Structures". In: *Phys. Rev. Lett.* 91 (12 2003), p. 126402. DOI: `10.1103/PhysRevLett.91.126402`.

[85] E. Schrödinger. "An Undulatory Theory of the Mechanics of Atoms and Molecules". In: *Phys. Rev.* 28 (6 1926), pp. 1049–1070. DOI: `10.1103/PhysRev.28.1049`.

[86] D. S. Schulman, A. J. Arnold, and S. Das. "Contact engineering for 2D materials and devices". In: *Chem. Soc. Rev.* 47 (9 2018), pp. 3037–3058. DOI: `10.1039/C7CS00828G`.

[87] J. M. Soler et al. "The SIESTA method for ab initio order-N materials simulation". In: *Journal of Physics: Condensed Matter* 14.11 (2002), p. 2745. DOI: `10.1088/0953-8984/14/11/302`.

[88] J. Svensson and E. E. B. Campbell. "Schottky barriers in carbon nanotube-metal contacts". In: *J. Appl. Phys.* 110.11 (2011), p. 111101. DOI: `10.1063/1.3664139`.

[89] S. M. Sze and Kwok K Ng. *Physics of semiconductor devices*. 2006.

[90] Philippe Tassin, Thomas Koschny, and Costas M. Soukoulis. "Graphene for Terahertz Applications". In: *Science* 341.6146 (2013), pp. 620–621. DOI: `10.1126/science.1242253`.

[91] J. Tersoff. “New empirical approach for the structure and energy of covalent systems”. In: *Phys. Rev. B* 37 (12 1988), pp. 6991–7000. DOI: `10.1103/PhysRevB.37.6991`.

[92] J. Tersoff. “New empirical model for the structural properties of silicon”. In: *Phys. Rev. Lett.* 56.6 (1986), pp. 632–635. ISSN: 1079-7114. DOI: `10.1103/PhysRevLett.56.632`.

[93] L. H. Thomas. “The calculation of atomic fields”. In: *Mathematical Proceedings of the Cambridge Philosophical Society* 23.5 (1927), 542–548. DOI: `10.1017/S0305004100011683`.

[94] N. Troullier and JL. Martins. “Efficient pseudopotentials for plane-wave calculations”. In: *Phys. Rev. B* 43 (3 1991), pp. 1993–2006. DOI: `10.1103/PhysRevB.43.1993`.

[95] M. Vanin et al. “Graphene on metals: A van der Waals density functional study”. In: *Phys. Rev. B* 81 (8 2010), p. 081408. DOI: `10.1103/PhysRevB.81.081408`.

[96] A. Venugopal, L. Colombo, and E. M. Vogel. “Contact resistance in few and multilayer graphene devices”. In: *Applied Physics Letters* 96.1 (2010), p. 013512. DOI: `10.1063/1.3290248`.

[97] A. Venugopal, L. Colombo, and E. M. Vogel. “Contact resistance in few and multilayer graphene devices”. In: *Appl. Phys. Lett.* 96.1 (2010), p. 013512. DOI: `10.1063/1.3290248`.

[98] D. Voiry, A. Mohite, and M. Chhowalla. “Phase engineering of transition metal dichalcogenides”. In: *Chem. Soc. Rev.* 44 (9 2015), pp. 2702–2712. DOI: `10.1039/C5CS00151J`.

[99] L. Wang et al. “One-dimensional electrical contact to a two-dimensional material”. In: *Science* 342.6158 (2013), pp. 614–617. DOI: `10.1126/science.1244358`.

[100] R. Waser and M. Aono. “Nanoionics-based resistive switching memories”. In: *Nature Materials* 6 (2007), pp. 833 –840. DOI: `10.1038/nmat2023`.

[101] A.N. Whitehead and B. Russell. *Principia Mathematica*. Principia Mathematica v. 2. University Press, 1912. URL: `https://books.google.es/books?id=sbTVAAAAMAAJ`.

[102] E. Wigner. “On the Interaction of Electrons in Metals”. In: *Phys. Rev.* 46 (11 1934), pp. 1002–1011. DOI: `10.1103/PhysRev.46.1002`.

[103] J. Wintterlin and M. L. Bocquet. “Graphene on metal surfaces”. In: *Surface Science* 603.10-12 (2009), pp. 1841–1852. DOI: `10.1016/j.susc.2008.08.037`.

[104] F. Withers et al. “Light-emitting diodes by band-structure engineering in van der Waals heterostructures”. In: *Nature Materials* 14 (2015), pp. 301–306. DOI: `10.1038/nmat4205`.

[105] Yanqing Wu et al. “State-of-the-Art Graphene High-Frequency Electronics”. In: *Nano Letters* 12.6 (2012), pp. 3062–3067. DOI: `10.1021/nl300904k`.

[106] K. L. N. Acharya X. Cartoixà and J. J. Palacios. “Contact resistance in metal/two-dimensional material junctions from first principles *in preparation*”.

[107] Won Seok Yun et al. “Thickness and strain effects on electronic structures of transition metal dichalcogenides: 2H-MX_2 semiconductors (M = Mo, W; X = S, Se, Te)”. In: *Phys. Rev. B* 85 (3 2012), p. 033305. DOI: `10.1103/PhysRevB.85.033305`.

[108] R. Zacharia, H. Ulbricht, and T. Hertel. “Interlayer cohesive energy of graphite from thermal desorption of polyaromatic hydrocarbons”. In: *Phys. Rev. B* 69 (15 2004), p. 155406. DOI: `10.1103/PhysRevB.69.155406`.

[109] J. Zhu, ZRL. Taylor, and OC. Zienkiewicz. *The Finite Element Method: Its Basis And Fundamentals*. Elsevier, 2005. ISBN: 9780080983561.